Combining omnidirectional vision with polarization vision for robot navigation

Abd El Rahman Shabayek

SPIM

Thèse de Doctorat

école doctorale **sciences pour l'ingénieur et microtechniques**

UNIVERSITÉ DE BOURGOGNE

APPORTS COMBINÉS DE LA VISION OMNIDIRECTIONNELLE ET POLARIMÉTRIQUE POUR LA NAVIGATION DE ROBOTS

Combining Omnidirectional Vision with Polarization Vision for Robot Navigation

Abd El Rahman SHABAYEK

SPIM

Thèse de Doctorat

école doctorale **sciences pour l'ingénieur et microtechniques**

UNIVERSITÉ DE BOURGOGNE

THÈSE présentée par

Abd El Rahman SHABAYEK

pour obtenir le

Grade de Docteur de
l'Université de Bourgogne

Spécialité : **Instrumentation et l'Informatique de l'Image**

APPORTS COMBINÉS DE LA VISION OMNIDIRECTIONNELLE ET POLARIMÉTRIQUE POUR LA NAVIGATION DE ROBOTS

Combining Omnidirectional Vision with Polarization Vision for Robot Navigation

Soutenue le 28 novembre 2012 devant le Jury :

Laurent BIGUE	Rapporteur	Professeur à l'Université de Haute Alsace
David FOFI	Directeur de thèse	Professeur à l'Université de Bourgogne
Youcef MEZOUAR	Rapporteur	Professeur à l'Université Blaise Pascal
Olivier MOREL	Co-directeur de thèse	Maître de conférence à l'Université de Bourgogne
Pascal VASSEUR	Président du jury	Professeur à l'Université de Rouen

Contents

Cover **2**

Jury **3**

Table of Contents **5**

List of Figures **11**

List of Tables **12**

List of Algorithms **13**

Acknowledgment **14**

Summary **15**

Résumé **17**

1 Introduction **19**
1.1 Polarization 19
1.2 Bio-Inspired Polarization Techniques 20
1.3 Skylight polarization 20
1.4 Problem statement 21
1.5 Contributions 22
1.6 Organization 23

2 Vision Based UAV Attitude Estimation **24**
2.1 Introduction 24
2.1.1 Vision sensors for attitude estimation 25
2.1.2 The main techniques for attitude estimation 26
2.2 Horizon Detection 27
2.2.1 Sky/Ground Segmentation 28
2.2.2 Polarization based segmentation 29
2.2.3 Using perspective sensors 31
2.2.4 Using omnidirectional sensors 31
2.2.5 Central catadioptric projection of the horizon 32
2.2.6 Horizon estimation and attitude computation 32
2.3 Vanishing Points 33
2.3.1 Perspective 34

2.3.2 Gaussian sphere . . . 34
2.3.3 Vertical vanishing points . . . 35
2.3.4 Horizontal vanishing points . . . 35
2.3.5 Catadioptric . . . 35
2.4 Stereo Vision And Optical Flow . . . 37
2.4.1 Stereo vision . . . 37
2.4.2 Optical flow . . . 38
2.4.3 Optical flow from stereo vision . . . 39
2.5 Summary and conclusion . . . 40

3 Skylight Polarization 41
3.1 Skylight polarization patterns . . . 41
3.2 Skylight polarization from a Fisheye lens . . . 43
3.3 Skylight polarization from Catadioptric sensors . . . 44
3.4 Omni-Pola-Catadioptric . . . 46
3.5 Deriving the Angle of Polarization: A new approach . . . 48
3.6 Comparison of the derived AOP and the literature . . . 49

4 Skylight Stokes Calibration 54
4.1 Ambiguity caused by a reflective surface . . . 54
4.2 Incident Stokes Calibration . . . 57
4.2.1 Muller calculus . . . 57
4.2.2 Calibration process . . . 58
4.3 Computing the angle and degree of polarization using Stokes parameters . . . 61
4.4 Calibration results . . . 62

5 Applications 66
5.1 Robot Orientation and Navigation . . . 67
5.1.1 Sensors using Photodiodes . . . 67
5.1.2 CCD, Fisheye and CMOS Sensors . . . 71
5.1.3 Water and mud detection for off-road navigation . . . 73
5.2 Solar angles estimation . . . 74
5.2.1 Azimuthal angle estimation . . . 74
5.2.2 Zenital angle estimation . . . 76
5.2.3 Adding noise . . . 78
5.3 AV attitude estimation . . . 81
5.3.1 USV/GV attitude estimation . . . 81
5.3.2 AV attitude estimation from α pattern . . . 85
5.3.3 Adding noise . . . 91

6 Conclusion and Perspectives 96

Bibliography 97

A Visual Behavior Based Bio-Inspired Polarization Techniques 117
A.1 Polarization based visual behavior in the animal kingdom . . . 118
A.1.1 Orientation and Navigation . . . 118
A.1.2 Water and Transparent Object Detection . . . 118
A.1.3 Camouflage Breaking . . . 119

A.1.4 Communication 119
A.2 Polarization-Inspired machine vision applications 119
A.3 Visualizing Polarization Information 120
A.4 Robot Orientation and Navigation 120
A.5 Underwater Polarization Vision 120
A.6 Communication 122
A.7 Camouflage Breaking 123
A.8 Miscellaneous 124
A.9 Summary 124

B Polarization patterns simulation examples 127
B.1 Omni-Pola-Catadioptric sensors 127
B.1.1 Uniform 128
B.1.2 Spherical 130
B.1.3 Parabolic 133
B.1.4 Hyperbolic 137
B.2 Noisy skylight polarization patterns 139
B.3 Solar angles estimation 140
B.4 AV attitude estimation 143

List of Figures

1.1 Polarization in the animal kingdom. From left to right and top to bottom: Bee, desert ant (Cataglyphis), nocturnal bird (owl), and salmon fish 21

2.1 An illustrative sketch of the attitude (roll, pitch, and yaw angles) 25
2.2 Perspective and omnidirectional (Fisheye and Catadioptric) cameras 26
2.3 Horizon in a) a perspective image, b) a non-central catadioptric image 28
2.4 Sky/Ground segmentation and horizon extraction based on polarization from non-central catadioptric images 30
2.5 The relation between the horizon projection and the roll and pitch angles. (Adapted from [51]). 32
2.6 Gaussian Sphere adapted from [168] 34
2.7 Illustration of the relation between a vertical vanishing point and the roll and pitch angles. 36
2.8 Stereo Vision and Optical Flow 37

3.1 FD-1665 3CCD [1] 47
3.2 AOP geometrical sketch. 48
3.3 Comparing our results against [160, 129]. The α patterns simulations in first, third, and fourth raw represent the captured α patterns in the second raw on 26-August-1999 (at 6, 12, 19 UTC+1 from left to right respectively) in the Tunisian Chott el Djerid (Latitude:33.867, Longitude:8.367) as reported in [160]. East is on the down rather than up in the figure (left rather than right of the compass) because we are looking up through the celestial dome rather than down onto a map. 50
3.4 Comparing our results against [129]. The α patterns simulations in first and third rows represent the captured pattern (as reported in [129]) in the second raw in June & July 2008 one hour before sunset at the university of Tokyo (Latitude:35.667, Longitude:139.667), Japan. Two different colormaps are used to simulate ([129])'s and our formula to emphasis the difference. East is on the down rather than up in the figure (left rather than right of the compass) because we are looking up through the celestial dome rather than down onto a map. 51
3.5 A comparison between our results and ([27], [21], [129]). 52

4.1 The difference between the incident and reflected Angle of Polarization pattern (α pattern) using a metallic (Aluminum) spherical mirror with refractive index $\hat{n} = 1.44 + 5.23i$. Simulation parameters are as shown in table (4.1). 54
4.2 The difference between the incident and reflected Angle of Polarization pattern (α pattern) using a non-metallic spherical mirror with refractive index $\hat{n} = 1.44$. Simulation parameters are as shown in table (4.1). 55
4.3 The reflected polarization angle $-90 \leqslant \alpha \leqslant 90$ over the full range of incident angles. The polarization angle α is not significantly affected by reflection from the metallic mirror for incidence angles less than approximately 50°. Aluminum surface with refractive index $\hat{n} = 1.44 + 5.23i$ 56
4.4 The reflected polarization angle $-90 \leqslant \alpha \leqslant 90$ over the full range of incident angles. The polarization angle α is significantly affected by reflection from the non-metallic mirror for incidence angles more than approximately 25°. Non-metallic surface with refractive index $\hat{n} = 1.44$ 57
4.5 Pola-Catadioptric design. 58
4.6 Simulation of incident, reflected and calibrated angle of polarization α for a metallic spherical mirror. 63
4.7 Simulation of incident, reflected and calibrated degree of polarization p for a metallic spherical mirror. 63
4.8 A snapshot of our simulation program. 64
4.9 Metallic spherical mirror simulation. 64

5.1 Diagrammatic description of POL OP unit. (Adapted from (Lambrinos et al., 2000, Chu et al., 2007)) 69
5.2 Azimuth estimation. 76
5.3 Solar angles estimation from a noisy α pattern. 79
5.4 γ estimation using algorithms (5.10, 5.11). 85
5.5 Estimating angles of rotation assuming the knowledge of the rotation axis. 88
5.6 Estimating three angles of rotation where no knowledge is assumed. The simulation parameters are the same like figures (5.5a, 5.5b) where the original α pattern is rotated by 10°around x, 20°around y, and 30°around z respectively. The estimated solutions are shown in the second, third and fourth row. Note that the rotation order is not assumed to be known. The start point is (0°,0°,0°), the lower bound is (−45°,−45°,−45°), and the upper bound is (45°,45°,45°). The earth is represented in dark green. . 89
5.7 Estimating three angles of rotation where no knowledge is assumed. The simulation parameters are the same like figures (5.5a, 5.5b) where the original α pattern is rotated by −5°around y, 40°around z, and 7°around x respectively. The estimated solutions are shown in the second, third and fourth row. Note that the rotation order is not assumed to be known. The start point is (0°,0°,0°), the lower bound is (−45°,−45°,−45°), and the upper bound is (45°,45°,45°). The earth is represented in dark green. . 90

5.8 Estimating angles of rotation assuming no knowledge of the rotation axises or rotation order. 91
5.9 γ estimation using algorithm (5.11) after adding noise. The table at the top shows the ground truth rotation, the estimated rotation, and the estimation error. Images from left to right are: the noisy rotated α pattern, the difference between the noisy and the theoretically rotated α pattern, the noisy rotated p pattern, and the difference between the noisy and the theoretically rotated p pattern. The simulation parameters are shown in table (5.6). Simulated pattern in Le Creusot on 24/07/2012 at 12:39:5. . . . 93
5.10 Two angles of rotation estimation assuming the knowledge of the rotation axises using algorithm (5.13) after adding noise. The table at the top shows the ground truth rotation, the estimated rotation, and the estimation error. Images from left to right are: the noisy rotated α pattern, the difference between the noisy and the theoretically rotated α pattern, the noisy rotated p pattern, and the difference between the noisy and the theoretically rotated p pattern. The earth is represented in dark green. The simulation parameters are shown in table (5.6). Simulated pattern in Le Creusot on 26/07/2012 at 11:12:15. 94
5.11 Estimating three angles of rotation using algorithm (5.13) after adding noise where no knowledge is assumed about the rotation order however better lower (2°,12°,22°) and upper (8°,18°,28°) bounds are assumed to be provided. The robot is rotated by (5°, 15°, 25°) around x, y, and z respectively. The table at the top shows the ground truth rotation, the estimated rotation, and the estimation error. Images from left to right are: the noisy rotated α pattern, the difference between the noisy and the theoretically rotated α pattern, the noisy rotated p pattern, and the difference between the noisy and the theoretically rotated p pattern. The earth is represented in dark green. The simulation parameters are shown in table (5.6). Simulated pattern in Le Creusot on 24/07/2012 at 12:39:5. 95

A.1 Polarization in the animal kingdom. From left to right and top to bottom: Bee, desert ant (Cataglyphis), nocturnal bird (owl), and salmon fish 118

B.1 Program snapshot to simulate polarization patterns on different types of mirrors 127
B.2 Uniform mirror 128
B.3 Polarization patterns (incident/reflected/calibrated) as they appear on a uniform mirror 129
B.4 Solar angles estimation from calibrated polarization patterns after being reflected on a uniform mirror 129
B.5 One rotation angle estimation from calibrated polarization patterns after being reflected on a uniform mirror 130
B.6 Spherical mirror 131
B.7 Polarization patterns (incident/reflected/calibrated) as they appear on a spherical mirror 131

B.8 Solar angles estimation from calibrated polarization patterns after being reflected on a spherical mirror 132
B.9 Two rotation angles estimation from calibrated polarization patterns after being reflected on a spherical mirror 133
B.10 Parabolic mirror where $radius = height$ 134
B.11 Polarization patterns (incident/reflected/calibrated) as they appear on a parabolic mirror 134
B.12 Solar angles estimation from calibrated polarization patterns after being reflected on a parabolic mirror 135
B.13 Three rotation angles estimation from calibrated polarization patterns after being reflected on a parabolic mirror 136
B.14 Hyperbolic mirror where $radius = 2{*}height$ and $eccentricity = 1.3$137
B.15 Polarization patterns (incident/reflected/calibrated) as they appear on a hyperbolic mirror 138
B.16 Solar angles estimation from calibrated polarization patterns after being reflected on a hyperbolic mirror 138
B.17 Rotation angles estimation from calibrated polarization patterns after being reflected on a hyperbolic mirror 139
B.18 Noisy incident angle α and degree p of polarization patterns. Speckle noise with variance 0.85 and mean 0. 140
B.19 Noisy incident angle α and degree p of polarization patterns. Gaussian noise with variance 15 and mean 3. 140
B.20 Solar azimuthal and zenital angles estimation. 141
B.21 Solar angles estimation from a noisy α pattern at 01:38. Simulation parameters are shown on the left handside and estimation results on the right handside. 142
B.22 Solar angles estimation from a noisy α pattern at 05:20. Simulation parameters are shown on the left handside and estimation results on the right handside. 142
B.23 Solar angles estimation from a noisy α pattern at 11:50. Simulation parameters are shown on the left handside and estimation results on the right handside. 143
B.24 Estimating two angles of rotation assuming the knowledge of the rotation axis. The robot is rotated around x by 10°then around z by 20°. The simulation parameters and the original α pattern (before rotation) are shown on the top. The estimation results and the rotated α pattern are shown on the bottom. Note that the rotation order is not assumed to be known. The earth is represented in dark green. 144
B.25 Estimating two angles of rotation assuming the knowledge of the rotation axis. The robot is rotated around y by 10°then around z by 20°. The simulation parameters and the original α pattern (before rotation) are shown on the top. The estimation results and the rotated α pattern are shown on the bottom. Only the first solution is accepted as the second did not converge to a value close to zero. Note that the rotation order is not assumed to be known. The earth is represented in dark green. 145

B.26 Estimating three angles of rotation where no knowledge is assumed about the rotation order however better lower (2°,12°,22°) and upper (8°,18°,28°) bounds are assumed to be provided. The robot is rotated by (5°, 15°, 25°) around x, y, and z respectively . The earth is represented in dark green. 146
B.27 Estimating one angle of rotation assuming no knowledge of the rotation axis. The robot is rotated around z-axis by 10°. The simulation parameters are shown on the top. The the rotated α pattern, estimation results, and the rotated pattern based on the first estimation are shown on the bottom from left to right respectively. The earth is represented in dark green. 147
B.28 Estimating two angles of rotation assuming no knowledge of the rotation axises. The robot is rotated around x by 10°then around z by 20°. The simulation parameters are shown on the top. The the rotated α pattern, estimation results, and the rotated pattern based on the first estimation are shown on the bottom from left to right respectively. The earth is represented in dark green. . . 148
B.29 γ estimation using algorithm (5.11) after adding Gaussian noise with zero mean and $variance = 10$. The upper part shows the program with the simulation parameters and the lower part shows the rotated noisy α pattern and the estimation results on the axis of rotation (z-axis). 149
B.30 γ estimation using algorithm (5.11) after adding Gaussian noise with $mean = 3$ and $variance = 10$. The upper part shows the program with the simulation parameters and the lower part shows the rotated noisy α pattern and the estimation results on the axis of rotation (z-axis). 150
B.31 γ estimation using algorithm (5.11) after adding speckle noise with zero mean and $variance = 0.04$. The upper part shows the program with the simulation parameters and the lower part shows the rotated noisy α pattern and the estimation results on the axis of rotation (z-axis). 151
B.32 General rotation estimation using algorithm (5.13) after adding Gaussian noise with zero mean and $variance = 10$. The upper part shows the program with the simulation parameters and applying the original rotation. The lower part shows the rotated noisy α pattern, the estimation results, and the first rotation estimation (roll ϕ, pitch β, and yaw γ) after being applied to the original incident α pattern. 152
B.33 General rotation estimation using algorithm (5.13) after adding Gaussian noise with $mean = 3$ and $variance = 10$. The upper part shows the program with the simulation parameters and applying the original rotation. The lower part shows the rotated noisy α pattern, the estimation results, and the first rotation estimation (roll ϕ, pitch β, and yaw γ) after being applied to the original incident α pattern. 153

B.34 General rotation estimation using algorithm (5.13) after adding speckle noise with zero mean and *variance* = 0.04. The upper part shows the program with the simulation parameters and applying the original rotation. The lower part shows the rotated noisy α pattern, the estimation results, and the first rotation estimation (roll ϕ, pitch β, and yaw γ) after being applied to the original incident α pattern. 154

List of Tables

2.1 The estimated attitude angles (Roll, Pitch, and Yaw). 39

4.1 Simulation parameters of figures (4.1, 4.2) 55
4.2 Simulation parameters of figures (4.6, 4.7) 62

5.1 Simulation parameters and solar angles computation figure (B.20) 75
5.2 Azimuth estimation after adding speckle noise with $v < 0.3$ . . . 80
5.3 Azimuth estimation after adding noise. 82
5.4 Zenith estimation after adding speckle noise with $v < 0.3$ 83
5.5 Zenith estimation after adding speckle and Gaussian noise . . . 84
5.6 Simulation parameters 87

A.1 Examples of the usage of polarization in several computer vision and robotics applications 125

List of Algorithms

5.1 Polarized light sensors (POL-sensors) 67
5.2 Scanning models (Lambrinos et al. 1997 [115]) 68
5.3 Simultaneous models (Lambrinos et al. 2000 [117]) 69
5.4 Bionic navigation sensor design (Chu et al. [32, 31, 33, 30, 254]) 70
5.5 Mimicking polarization vision in the head of a dragonfly called Hemianax Papuensis (Chahl & Mizutani, 2010 [26]) 71
5.7 Solar zenital angle estimation. 76
5.6 Solar azimuthal angle estimation. 77
5.8 Solar zenital angle estimation. 78
5.9 Estimating the GV orientation from the solar azimuthal angle. . 81
5.10 Estimating the GV orientation from the α pattern. 81
5.11 Estimating the GV orientation from the α pattern. 85
5.12 Estimating the AV orientation from the α pattern. 86
5.13 Estimating the AV orientation from the α pattern. 86

Acknowledgment

الحمد لله رب العالمين، اللهم لك الحمد كما ينبغي لجلال وجهك وعظيم سلطانك

I would like to deeply thank my supervisors Prof. David Fofi and Dr. Olivier Morel for their great support and guidance during this work. I appreciate the help given by Dr. Cedric Demonceaux in some parts of our work. I warmly thank them for their time and effort. Thanks to all my colleagues in Le2i/IUT/uB who supported me and shared ideas, they paved my way to be a better researcher and get a better career.

Thanks to all my friends in Le Creusot for being so friendly and helpful during this wonderful period of my life. It was such a great experience and joy for me being here with you.

I owe the most to my parents and family who have provided me everything I need to be here right now. I believe they made me a better person. They have always supported me emotionally and financially.

My great thanks and appreciation to my wife and kids (Malak, Moaz, and Hager), I owe them a lot. They have been alone for long time while I was working in the lab; they had full patience. They had fully emotionally supported me during the whole period.

Summary

Polarization is the phenomenon that describes the oscillations orientations of the light waves which are restricted in direction. Polarized light has multiple uses in the animal kingdom ranging from foraging, defense and communication to orientation and navigation. Chapter (1) briefly covers some important aspects of polarization and explains our research problem.

We are aiming to use a polarimetric-catadioptric sensor since there are many applications which can benefit from such combination in computer vision and robotics specially robot orientation (attitude estimation) and navigation applications. Chapter (2) mainly covers the state of art of visual based attitude estimation.

As the unpolarized sunlight enters the Earth's atmosphere, it is Rayleigh-scattered by air, and it becomes partially linearly polarized. This skylight polarization provides a significant clue to understanding the environment. Its state conveys the information for obtaining the sun orientation. Robot navigation, sensor planning, and many other applications may benefit from using this navigation clue. Chapter (3) covers the state of art in capturing the skylight polarization patterns using omnidirectional sensors (e.g fisheye and catadioptric sensors). It also explains the skylight polarization characteristics and gives a new theoretical derivation of the skylight angle of polarization pattern.

Our aim is to obtain an omnidirectional 360° view combined with polarization characteristics. Hence, this work is based on catadioptric sensors which are composed of reflective surfaces and lenses. Usually the reflective surface is metallic and hence the incident skylight polarization state, which is mostly partially linearly polarized, is changed to be elliptically polarized after reflection. Given the measured reflected polarization state, we want to obtain the incident polarization state. Chapter (4) proposes a method to measure the light polarization parameters using a catadioptric sensor. The possibility to measure the incident Stokes is proved given three Stokes out of the four reflected Stokes.

Once the incident polarization patterns are available, the solar angles can be directly estimated using these patterns. Chapter (5) discusses polarization based robot orientation and navigation and proposes new algorithms to estimate these solar angles where, to the best of our knowledge, the sun zenith angle is firstly estimated in this work given these incident polarization patterns. We also propose to estimate any vehicle orientation given these polarization patterns.

Finally the work is concluded and possible future research directions are discussed in chapter (6). More examples of skylight polarization patterns, their calibration, and the proposed applications are given in appendix (B).

Our work may pave the way to move from the conventional polarization vision world to the omnidirectional one. It enables bio-inspired robot orientation

and navigation applications and possible outdoor localization based on the skylight polarization patterns where given the solar angles at a certain date and instant of time may infer the current vehicle geographical location.

Résumé

La polarisation est le phénomène qui décrit les orientations des oscillations des ondes lumineuses qui sont limitées en direction. La lumière polarisée est largement utilisée dans le règne animal, à partir de la recherche de nourriture, la défense et la communication et la navigation. Le chapitre (1) aborde brièvement certains aspects importants de la polarisation et explique notre problématique de recherche.

Nous visons à utiliser un capteur polarimétrique-catadioptrique car il existe de nombreuses applications qui peuvent bénéficier d'une telle combinaison en vision par ordinateur et en robotique, en particulier pour l'estimation d'attitude et les applications de navigation. Le chapitre (2) couvre essentiellement l'état de l'art de l'estimation d'attitude basée sur la vision.

Quand la lumière non-polarisée du soleil pénètre dans l'atmosphère, l'air entraine une diffusion de Rayleigh, et la lumière devient partiellement linéairement polarisée. Le chapitre (3) présente les motifs de polarisation de la lumière naturelle et couvre l'état de l'art des méthodes d'acquisition des motifs de polarisation de la lumière naturelle utilisant des capteurs omnidirectionnels (par exemple fisheye et capteurs catadioptriques). Nous expliquons également les caractéristiques de polarisation de la lumière naturelle et donnons une nouvelle dérivation théorique de son angle de polarisation.

Notre objectif est d'obtenir une vue omnidirectionnelle à 360° associée aux caractéristiques de polarisation. Pour ce faire, ce travail est basé sur des capteurs catadioptriques qui sont composées de surfaces réfléchissantes et de lentilles. Généralement, la surface réfléchissante est métallique et donc l'état de polarisation de la lumière incidente, qui est le plus souvent partiellement linéairement polarisée, est modifiée pour être polarisée elliptiquement après réflexion. A partir de la mesure de l'état de polarisation de la lumière réfléchie, nous voulons obtenir l'état de polarisation incident. Le chapitre (4) propose une nouvelle méthode pour mesurer les paramètres de polarisation de la lumière en utilisant un capteur catadioptrique. La possibilité de mesurer le vecteur de Stokes du rayon incident est démontré à partir de trois composants du vecteur de Stokes du rayon réfléchi sur les quatre existants.

Lorsque les motifs de polarisation incidents sont disponibles, les angles zénithal et azimutal du soleil peuvent être directement estimés à l'aide de ces modèles. Le chapitre (5) traite de l'orientation et de la navigation de robot basées sur la polarisation et différents algorithmes sont proposés pour estimer ces angles dans ce chapitre. A notre connaissance, l'angle zénithal du soleil est pour la première fois estimé dans ce travail à partir des schémas de polarisation incidents. Nous proposons également d'estimer l'orientation d'un véhicule à partir de ces motifs de polarisation.

Enfin, le travail est conclu et les possibles perspectives de recherche sont discutées dans le chapitre (6). D'autres exemples de schémas de polarisation de la lumière naturelle, leur calibrage et des applications sont proposées en annexe (B).

Notre travail pourrait ouvrir un accès au monde de la vision polarimétrique omnidirectionnelle en plus des approches conventionnelles. Cela inclut l'orientation bio-inspirée des robots, des applications de navigation, ou bien la localisation en plein air pour laquelle les motifs de polarisation de la lumière naturelle associés à l'orientation du soleil à une heure précise peuvent aboutir à la localisation géographique d'un véhicule.

Chapter 1

Introduction

Solar radiation entering the atmosphere of the Earth becomes partially linearly polarized due to scattering interactions with atmospheric constituents (e.g various gases, aerosol particles, water droplets and ice crystals). The formed skylight polarization pattern mainly depends on a) the solar position, b) the distribution of atmospheric components, and c) the reflection characteristics of the underlying surface.

Skylight polarization has been the subject of numerous theoretical and experimental investigations since its discovery by Arago in 1809 (e.g., [28], [152], [191], [97], [38]).The characteristics of skylight polarization can be used to indicate atmospheric turbidity ([17]), detect clouds across the sky ([99]), and detect the horizon line for attitude estimation ([192]) . On the other hand, celestial polarization also bears a great biological importance, since numerous species are capable of perceiving polarization, as an independent property of light beyond intensity and color, and using it as a cue for their orientation (e.g., [66, 67], [237], [104]). It was also hypothesized that Vikings could make use of skylight polarization when navigating across the sea ([164, 165]).

In the past, point-source polarimeters were used for ground-based measurements of celestial polarization to obtain degree and angle of linear polarization for different wavelengths at a small spot in the sky. Recently, the observation of skylight polarization over the whole celestial hemisphere become available by the development of full-sky (i.e., 180° field of view) imaging polarimetry which ensures a fast and accurate data collection ([155], [229], [73, 74], [160]).

1.1 Polarization

Polarization is the phenomenon that describes the oscillations orientation of the light (or other radiation) waves which are restricted in direction. Light's vector orientation can be weekly detected by some humans with their naked eyes, but humans need the help of polarizing optics to visualize most invisible polarization effects ([78], [1]).

Polarization of light was first discovered by Bartolinus (1625-1698), he found that when a light ray is refracted by a calcite crystal, two rays are produced. One follows the ordinary laws of refraction and the other follows a different law [38]. Huygens (1629-1695) made several observations like Bartolinus noting the two

different rays with different properties. He noticed if either ray passed through a second crystal, the emergent intensity strongly depended on the second crystal orientation. This observation proved the existence of an asymmetry around the direction of propagation of certain light rays which is due to polarization [38].

1.2 Bio-Inspired Polarization Techniques

For long time, it was thought that sensing of polarization in animals is invariably related to their behavior like navigation and orientation. Polarized light has been shown to have multiple uses in the animal kingdom, ranging from foraging, defense, and communication to orientation and navigation ([238, 170]). The light polarization pattern in the atmosphere or underwater has been found to be highly regular depending on the position of the sun in the sky, which suggests that the polarization patterns constitute a reliable source of orientational information for many animals. Recently, it was found that polarization can be part of a high-level visual perception, permitting a wide area of vision applications. Polarization vision can be used for most tasks of color vision like: object recognition, contrast enhancement, camouflage breaking, and signal detection and discrimination.

Sky polarization patterns are used by many insects for navigation. Honeybees use celestial polarization to move between the hive and foraging locations ([167, 238, 42]). Cataglyphis ants ([42]) and nocturnal ([48]) use the sun and moon, respectively, celestial polarization for similar tasks. Salmon fishes may have a similar ability ([88]), which allows them to orient in underwater light fields ([156]). Light reflection from water surfaces results in horizontally polarized light which is utilized by water beetles and other insects for orientation. ([188, 189, 190]). Some of these animals are shown in figure (1.1).

1.3 Skylight polarization

Skylight polarization provides a significant clue to understand the environment. The skylight polarization state conveys the information for obtaining the sun orientation. As the unpolarized sunlight enters the Earth's atmosphere, it is Rayleigh-scattered by air, and it becomes partially linearly polarized. If the atmosphere is clear (cloudless), this scattering phenomenon results in the well-known spatial distribution of the radiance (intensity), color, the degree of polarization p , and the angle of polarization α ([94]). Robot navigation, sensor planning, and many other applications may benefit from using this navigation clue. Chapter (3) discusses in detail the skylight polarization patterns and how they are captured. We also provide a new derivation of the skylight angle of polarization α and a comparison with the state of the art methods. Our interest is in omnidirectional polarization vision and hence it is dedicated to the usage of omnidirectional sensors to measure skylight polarization patterns. Omnidirectional skylight polarization measurements obtained by fisheye lenses, catadioptric sensors (combing mirrors with cameras), and our proposed omni-pola-catadioptric sensor formed by a mirror and a polarizational camera are also covered.

Figure 1.1: Polarization in the animal kingdom. From left to right and top to bottom: Bee, desert ant (Cataglyphis), nocturnal bird (owl), and salmon fish

1.4 Problem statement

We are aiming to use a polarizational-catadioptric sensor which has a field of view up to 360° since there are many applications which can benefit from such combination in computer vision and robotics. Polarization vision can be part of high-level visual perception permitting wide area of vision applications as it can be used for most tasks of color vision like: object recognition, contrast enhancement, camouflage breaking, and signal detection and discrimination. Omni-pola vision may enrich the robotic visual capabilities in different fields like:

- industrial inspection applications, e.g (metallic cyclinderical internal surface defect inspection can be greatly enhanced using a pola-catadioptric sensor).
- mineral exploration, e.g (inspect the soil characteristics while/after drilling).
- underwater pipe inspection, underwater oil reg inspection.
- transparent objects tracking and camouflage breaking for military purposes.
- mobile robot orientation and navigation, e.g (**outdoor** orientation and navigation decisions can be taken based on the skylight polarization pattern like bees, **indoor** orientation and navigation decisions can be taken based on the polarizational features of the surrounding environment like detecting a glass door which is transparent for conventional visual sensors).

In this work the focus is on the last point, where we investigate outdoor robot orientation and navigation using bio-inspired techniques based on polarization vision.

Skylight polarization patterns (chapter 3) constitute a reliable source of orientational information for many animals, hence we proposed an omni-polarizational sensor to capture the full polarimetric pattern (chapter 4) and developed algorithms (chapter 5) to obtain the solar angles and the vehicle attitude based on these patterns.

State of the art in visual based Unmanned Aerial Vehicle (UAV) attitude estimation is given in chapter (2) in which we target vision only techniques to draw the main research lines considered to solve this problem using visual sensors only. UAV was mainly aimed to as it can be considered the most general case for autonomous robots attitude estimation.

Our novel proposed omni-polarizational (pola-catadioptric) sensor consists of a metallic mirror and a lens. This metallic mirror changes the polarization state of the incident beam a little but to gain sufficient accuracy we proposed a method to calibrate the incident polarization state (4).

1.5 Contributions

In this work, our aim is to combine omnidirectional and polarizational sensors to obtain omnidirectional polarization vision for robot navigation. In the way to accomplish this target, the literature was surfed to produce three surveys, a novel pola-catadioptric sensor and several algorithms for solar angles computation and Autonomous Vehicle attitude estimation algorithms. Here is a list of contributions:

- A complete dedicated survey to one of the most important bio-inspired visual features in nowadays applications [see appendix (A) ([197])].
- A complete survey on vision based UAV attitude estimation techniques [see chapter (2) ([192])].
- A comprehensive survey about measuring skylight polarization patterns using omnidirectional sensors was given in [see chapter (3)].
- An analytic form of the skylight angle of polarization was derived [see section (3.5)].
- A novel pola-catadioptric sensor was proposed [see section (3.4) ([193, 197])].
- Only three out of the four reflected Stokes are proved to be sufficient to estimate the three incident Stokes [see section (4)] and calibrating the polarization state of incident light after being reflected from any surface [see section (4)].
- Solar angles estimation from skylight polarization patterns where, to the best of our knowledge, the sun zenith angle is firstly estimated here given these patterns [see section (5.2)] and autonomous vehicle attitude estimation from skylight polarization patterns [see section (5.3)].

- MATLAB® toolbox to simulate skylight polarization patterns, interact with different types of mirrors, and calibrate the incident polarization state from the reflected polarization patterns . User can travel in time and space to simulate these patterns anywhere in the earth at any instant of time. All solar information are provided. The user is capable of estimating the solar angles given these polarization patterns. He can also rotate the mirror (the robot which the mirror is attached to its center of gravity) and estimate the rotation angles from the polarization patterns. The user is free to add any amount of noise and play around with several parameters concerning time, space, and mirrors [snapshots of the different tasks are provided in chapters (, 5)].

1.6 Organization

Chapter (2) covers vision based UAV attitude estimation techniques passing through horizon detection, vanishing points, stereo vision and optical flow based techniques.

Chapter (3) explains the skylight polarization patterns and covers the state of the art in capturing the skylight polarization patterns using fisheye, catadioptric, our proposed omni-pola-catadioptric sensors, the angle of polarization derivation, and a comparison between our new formula and what exists in literature.

Chapter (4) covers the skylight Stokes calibration process where the ambiguity caused by reflective surface is highlighted and the proposed calibration of the incident skylight polarization by computing its stokes parameters is explained.

Chapter (5) will give a detailed survey about polarization based robot orientation and navigation. The chapter will cover applications based on the calibrated incident polarization patterns where the solar angles and robot attitude (roll, pitch, and yaw angles) are estimated.

Finally the work will be concluded and possible future research directions will be discussed in chapter (6).

Chapter 2

Vision Based UAV Attitude Estimation

Unmanned aerial vehicles (UAVs) are increasingly replacing manned systems in situations that are dangerous, remote, or difficult for manned aircraft to access. Its control tasks are empowered by computer vision technology. Visual sensors are robustly used for stabilization as primary or at least secondary sensors. Hence, UAV stabilization by attitude estimation from visual sensors is a very active research area. Vision based techniques are proving their effectiveness and robustness in handling this problem. In this work a comprehensive review of UAV vision based attitude estimation approaches ([192]) is covered, starting from horizon based methods and passing by vanishing points, optical flow, and stereoscopic based techniques.

2.1 Introduction

In order to determine the pose of the vehicle accurately and rapidly, the regular approach is to use inertial sensors with other sensors and applying sensor fusion. Some sensors used for this purpose are the Global positioning sensor (GPS), inertial navigation sensor (INS), as well as other sensors such as altitude sensors (ALS) and speedometers. These sensors have some limitations. GPS sensor for example, is not available at some locations or readings are subject to error. INS has the disadvantage of accumulation of errors. To overcome these limitations, vision-based navigation approaches have been developed. These approaches can be used where GPS or INS systems are not available or can be used with other sensors to obtain better estimations. UAV attitude estimation has been deeply studied in terms of data fusion of multiple low cost sensors in a Kalman filter (KF) framework to have the vehicle full state of position and orientation. But in pure vision based methods, if a horizontal world reference is visible (e.g horizon) the camera attitude can be obtained.

In order to control a flying vehicle at least six parameters (pose of the vehicle) should be known; Euler angles representing the orientation of the vehicle and a vector of coordinates, representing the position of the vehicle. Pose estimation basically depends on viewing a world unchanging physical reference (e.g landmarks on the ground) for accurate estimation. Our main concern in this

work is to review the work that focuses on attitude (roll, pitch, and yaw angles shown in figure (2.1)) estimation rather than pose estimation.

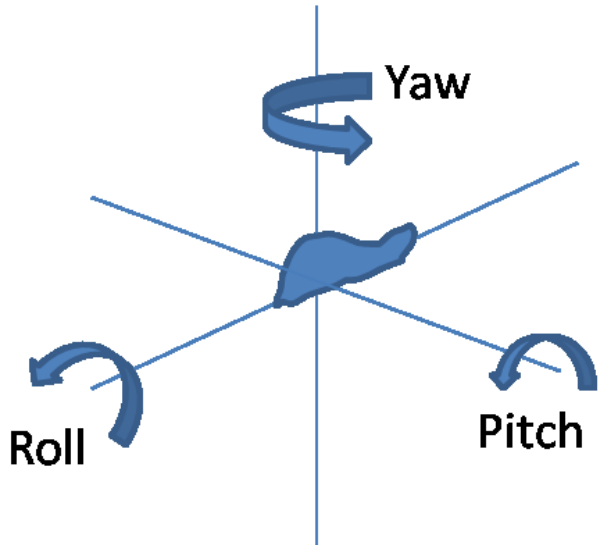

Figure 2.1: An illustrative sketch of the attitude (roll, pitch, and yaw angles)

In a typical flight, the demand for yaw angle will be largely constant and hence disturbances tend to have a relatively small effect on yaw. Further, small steady state errors are normally acceptable since (unlike roll and pitch) any errors will have no further effect on the UAV motion. Therefor, for the sake of UAV stabilization, the most important angles to be estimated are the pitch and roll angles as most of the work in literature propose. In this work, the focus is on attitude estimation from perspective and omnidirectional cameras.

Sections (2.2, 2.3, 2.4), will review the general techniques for attitude estimation from visual sensors (perspective and omnidirectional only) in detail. In section (2.2), horizon detection algorithms will be briefly explained and reviewed. Vanishing points based techniques are reviewed in section (2.3). The classical and hybrid approaches using stereo-vision and optical flow are reviewed in section (2.4). Finally we conclude in section (2.5).

2.1.1 Vision sensors for attitude estimation

Vision based methods were first introduced by [61] . They proposed to equip a Micro Air Vehicle (MAV) with a perspective camera to have a vision-guided flight stability and autonomy system. Omnidirectional sensors for attitude estimation were first introduced by [51]. The omnidirectional sensors (Fisheye and Catadioptric cameras shown in figure (2.2)) were used in different scenarios. Catadioptric sensors are commercially available for reasonable prices. A catadioptric sensor has two main parts, the mirror and the lens. The lens could be telecentric or perspective. The sensor is in general assembled as shown in figure (2.2c).

Omnidirectional sensors were used alone or in stereo configurations. Omnidirectional vision presents several advantages: a) a complete surrounding of the UAV can be captured and the horizon is totally visible, b) possible occlusions will have lower impact on the estimation of the final results, c) whatever the attitude of the UAV, the horizon is always present in the image, even partially, and the angles can always be computed, d) it is also possible to compute the roll and pitch angles without any prior hypothesis, contrary to the applications using a perspective camera. Yet, catadioptric vision also presents some drawbacks. For example, a) a catadioptric image contains significant deformations due to the geometry of the mirror and to the sampling of the camera, b) catadioptric cameras should be redesigned to a lower scale to be attached to a micro air vehicle (MAV).

(a) Perspective (b) Fisheye

(c) Catadioptric

Figure 2.2: Perspective and omnidirectional (Fisheye and Catadioptric) cameras

2.1.2 The main techniques for attitude estimation

In literature, the first group of methods tries to detect a horizontal reference frame in the world to estimate the up direction and hence the attitude of the vehicle. The horizon, if visible, is the best natural horizontal reference to be used [61]. However, in urban environments the horizon might not be visible. Hence, the second group tries to find the vanishing points from parallel vertical and horizontal lines which are basic features of man made structure (e.g [53]). The third group was biologically inspired from insects, it employs the UAV

motion (optical flow) for the sake of required estimation [12]. Stereo vision based techniques came to the play to open the door for more accurate estimation specially if combined with optical flow (e.g [133]). All these techniques will be discussed in the following sections.

Most of the employed techniques in literature use the Kalman filter (KF) or one of its variations in order to obtain an accurate and reliable estimation specially if more than one sensor is used and their measurements are fused. For a general parameter estimation issue, the extended Kalman filter (EKF) technique is widely adopted. Due to the processing of EKF in a linear manner, it may lead to sub-optimal estimation and even filter divergence. Nevertheless, state estimation using EKF assumes that both state recursion and covariance propagation are Gaussian. Unscented Kalman filter (UKF) resolves the nonlinear parameter estimation and machine learning problems. It can outperform the EKF especially for those highly nonlinear system dynamics/measurement processes. None of the Jacobean or derivatives of any functions are taken under the UKF processing [105]. For example in [57], using an EFK, the candidate horizon lines are propagated and tracked through successive image frames, with statistically unlikely horizon candidates eliminated. In [107], they followed the EKF framework to combine inertial and visual sensor for real time attitude estimation. They have designed a KF for image line measurements.

2.2 Horizon Detection

The visual sensor is not only a self-contained and passive like an INS but also interactive with its environment. An absolute attitude can be provided by detecting a reliable world reference frame. Attitude computation by vision is based on the detection of the horizon, which appears as a line in perspective images or a curve in omnidirectional images as shown in figure (2.3), and on the estimation of the angle between the horizon and a horizontal reference.

Due to the difficulty in obtaining ground-truth for aircraft attitude, most of the work in literature do not provide a quantitative measure of error in their estimates of roll and pitch. In [220], they provided a complexity and performance comparison between their method and other methods in literature. They have included a comparison table of execution times for various published studies on visual attitude estimation.

In the following subsections, we will cover in detail the different segmentation approaches for horizon detection in section (2.2.1) where both the perspective and omnidirectional scenarios will be reviewed. Section (2.2.3) will briefly discuss horizon estimation and attitude computation in the perspective case. Section (2.2.4) will briefly discuss the same in the omnidirectional case specially in the catadioptric scenario which is frequently used.

(a) Perspective (b) Non-central catadioptric

Figure 2.3: Horizon in a) a perspective image, b) a non-central catadioptric image

2.2.1 Sky/Ground Segmentation

As the segmentation of sky and ground is a crucial step toward extracting the horizon line/curve, which is used for attitude estimation, these segmentation methods will be discussed here.

Using perspective vision, algorithms employing Gaussian assumptions for sky/ground segmentation fails in scenarios where the underlying Gaussian assumption for the sky and ground appearances is not appropriate [61]. These assumptions might be enhanced by a statistical image modeling framework by building prior models of the sky and ground then trained. Since the appearances of the sky and ground vary enormously, no single feature is sufficient for accurate modeling; as such, these algorithms rely both on color and texture as critical features. They may use hue and intensity for color representation, and the complex wavelet transform for texture representation. Then they may use Hidden Markov Tree models as underlying statistical models over the feature space [222]. In [57], the algorithm is based on detecting lines in an image which may correspond to the horizon, followed by testing the optical flow against the measurements expected by the motion filter.

Using omnidirectional vision, some algorithms use markovian formulation of sky/ground segmentation based on color information [51], or the sky/ground partitioning is done in the spherical image thanks to the optimization of the Mahalanobis distance between these regions. The search for points in either regions takes place in the RGB space [52]. In order to isolate the sky from the ground [132, 131], an approach based on the method employed by [36] weights the RGB components of each pixel using the function $f\,(RGB) = 3B^2/(R + G + B)$.

In [220], they propose an algorithm which can be incorporated into any vision system (e.g. narrow angle, wide angle or panoramic), irrespective of the way in which the environment is imaged (e.g. through lenses or mirrors). The proposed horizon detection method consists of four stages: a) enhancing sky/ground contrast, b) determining optimum threshold for sky and ground segmentation, c) converting horizon points to vectors in the view sphere, and d) fitting 3D plane to horizon vectors to estimate the attitude.

In [215] they proposed segmentation using temperature from thermopile sensors in the thermal infrared band. However, in this work, the focus will be on attitude estimation from perspective and omnidirectional sensors only.

The previous segmentation solutions are either complex and/or time consuming. A method based on polarization for segmentation in section (2.2.2) is proposed. We believe it will have significant enhancements in both complexity and time due to its simplicity . We propose a novel non-central catadioptric sensor where the mirror is a free-form shape and the camera is polarimetric (e.g FD-1665P Polarization Camera [1]) to be used for attitude estimation.

2.2.2 Polarization based segmentation

Instead of using color information or edge detection algorithms for segmentation which may require different complex models and offline processing as shown in 2.2 , we propose to use polarization information which exists in the surrounding nature. Polarization information are directly computed from three intensity images taken at three different angles of a linear polarization filter (see section 4.3) or at one shot using a polarizational camera [1].

Using polarization for segmentation is not new. It was used for rough surface segmentation [219], material classification [241], water hazards detection for autonomous off-road navigation [248] , and similar applications. However, to the best of our knowledge, it is the first time to propose using polarization for sky/ground segmentation for UAV attitude estimation.

Figure (2.4) shows the segmentation results using the formulas in section (4.3) for non-central catadioptric images with the horizon detected by simply detecting the transition area. This technique is very simple and can be optimized by kind of binary search in the image having very rapid and robust results for the detected horizon in the image. Only few regions of the image are needed to be inspected for their degree or angle of polarization to decide for the search direction. Unlike conventional segmentation methods, thanks to polarization, we do not face the illumination problem caused by the sun being in the image.

After extracting the horizon, the UAV attitude can be estimated by the state of the art methods as explained in this chapter.

(a) 0°

(b) 45°

(c) 90°

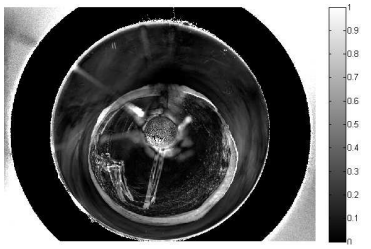

(d) Segmentation based on the degree of polarization

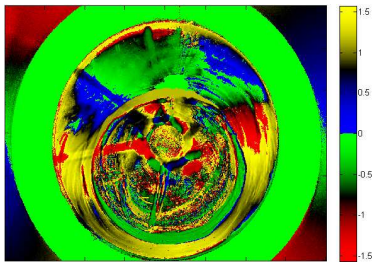

(e) Segmentation based on the angle of polarization

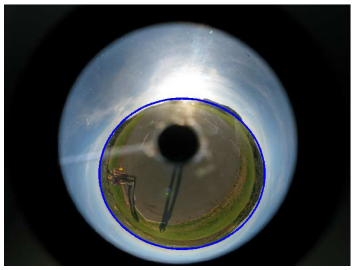

(f) Extracted horizon curve

Figure 2.4: Sky/Ground segmentation and horizon extraction based on polarization from non-central catadioptric images

Section (4.3) shows how to compute the degree and angle of polarization. For the sake of completeness we mention here a different method by [241] to compute the angle and degree of polarization which can be used also for segmentation.

The angle (phase) of polarization is computed as follows:

$$\begin{aligned} \alpha \quad &= \quad 0.5 * tan^{-1}(\frac{I_0 + I_{90} - 2I_{45}}{I_{90} - I_0}) + 90 \\ if \quad I_{90} &< \quad I_0 \\ \quad if \quad &I_{45} < I_0 \\ \quad \alpha \quad &= \alpha + 90 \\ \quad else \quad &\alpha = \alpha - 90 \end{aligned} \tag{2.1}$$

and the degree of polarization is:

$$p = \frac{I_{90} - I_0}{(I_{90} + I_0) * cos(2\alpha)} \tag{2.2}$$

where I_0, I_{45}, and $I_{90}$are intensity images taken at 0°, 45°, and 90° of the rotating polarizer respectively (or at one shot from a polarizational camera).

In future work, we may provide detailed algorithms with complexity and run time comparison with other methods found in literature.

2.2.3 Using perspective sensors

The horizon is projected as a line in the perspective image. Intuitively, it is required to extract that line. Most methods first segment the image into sky/ground areas, then take the separating points as the horizon line. The attitude is dependent on the gradient of that horizon line on the image plane. In literature, the general approach is to find the normal to the plane of the horizon in order to estimate the roll and pitch angles. The normal vector has direct mathematical relation with the attitude as expressed in different methods. The work done by [10, 223] are examples of successful autonomous control of a MAV based on attitude estimation from the horizon detected.

In literature, horizon detection problem has been addressed by segmentation and edge detection. In [61, 62] they proposed to equip a MAV with a perspective camera to have a vision-guided flight stability and autonomy system. They detected the horizon by extracting the straight line that separates the sky from the ground using the context difference of the two regions. In [222] they treated the horizon detection problem as a subset of image segmentation and object recognition, and used a percentage of the sky seen as an error signal to a flight stability controller on a MAV. The resulting system was stable enough to be safely flown by an untrained operator in real time. In contrast, [10] uses a direct edge-detection technique, followed by automatic threshold and a Hough-like algorithm to generate a "projection statistic"' for the horizon. It claims a 99% success rate over several hours of video. Importantly, it deals only with detection, not estimation of attitude. In [57] they propose an algorithm slightly similar to [10] in that it uses an edge detection technique followed by a Hough transform. However, they propose different image pre-filtering. In [34, **?**, 35, 36] they use the centroids of sky and ground to extract the horizon and derive the different angles. They try to simplify their work by using a circular mask to reduce image asymmetry and to simplify the calculations.

2.2.4 Using omnidirectional sensors

The use of a single perspective camera generates several drawbacks. Firstly, a partial view of the environment and important occlusions in the horizon can have a serious influence on the final result. Secondly, the horizon is visible only in a particular interval of roll and pitch values. If the UAV gets out of this interval, the final image is exclusively made of sky or earth and the horizon cannot be detected. Thirdly, it is only possible to compute the roll angle while the pitch is only approximated thanks to a hypothesis on the altitude of the UAV. All that pushed the need toward employing omnidirectional sensors to capture the horizon in almost all scenarios. The horizon appears as a curve

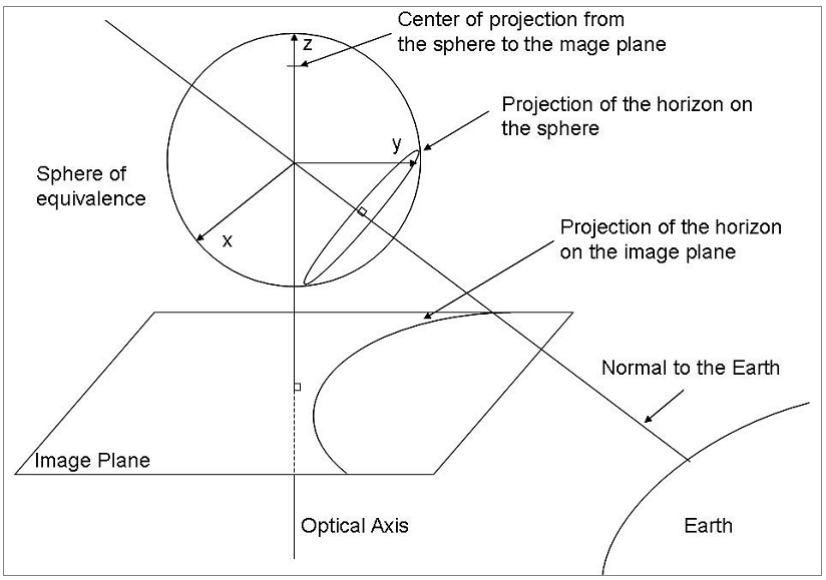

Figure 2.5: The relation between the horizon projection and the roll and pitch angles. (Adapted from [51]).

in the omnidirectional image. It is common to use both fisheye and central catadioptric sensors. As both are treated by the equivalence sphere theory proposed by [9]. The particular geometric characteristics of the catadioptric sensor will be briefly explained in the next section. Once the horizon is detected, these characteristics are used to compute the attitude of the UAV.

2.2.5 Central catadioptric projection of the horizon

As demonstrated in [9], a 3D sphere projects on the equivalence sphere in a small circle, and then on the catadioptric image plane in an ellipse (see figure (2.5)). Consequently, the attitude computation is based on searching for an ellipse in the omnidirectional image or a small circle on the equivalent sphere which corresponds to the horizon. The geometrical properties of the equivalent sphere allow to deduce the roll and pitch angles. Indeed, the normal of the projected horizon on the sphere, which is also confounded with the line passing through the center of the sphere of equivalence and through the center of the earth represents in fact the attitude of the UAV depending on the position of the optical axis. Then, the computation of the coordinates of the optical axis is sufficient in order to deduce the roll and pitch angles.

2.2.6 Horizon estimation and attitude computation

In order to estimate the horizon, first the catadioptric image should be segmented to obtain the sky/ground and hence the points belonging to the horizon. Next, the horizon points should be back projected on the equivalence sphere.

Finally, the best plane passes through the horizon on that sphere should be estimated to deduce its normal which gives the roll and pitch angles (e.g [51, 52]).

In [51], they proposed to use an omnidirectional visual sensor in order to compute the attitude of a UAV. They have extended the work of [61, 62] to detect the curved horizon line. They show an adaptation of the Markov Random Fields (MRFs) to treat the deformations in the catadioptric images in order to detect the horizon and hence the catadiotric geometric characteristics are used to compute the UAV attitude. This method gives interesting results but do not use sufficiently the geometric characteristics of catadioptric vision. Moreover, the segmentation step is time consuming and do not permit a real time implementation. In [52], they present higher accuracy and computation time. They use the geometric characteristics of the central catadioptric sensor for a formulation of the process as an optimization problem which is solved on the sphere of equivalence in order to compute directly the attitude angles. In [15], a hybrid method that is using the horizon and the homography is proposed. In [132, 131], they propose a similar approach to [51] for attitude estimation and a stereo-based system for height and motion estimation.

2.3 Vanishing Points

In [52, 51], the horizon was determined with Random Markow Fields or RGB based Mahalanobis distance. This approach requires the conditions where the horizon is visible. In addition, it can not be used to estimate the yaw angle. In urban environments, the world reference can be the parallel lines which are a basic property of man-made structures. In this situations, vanishing points at the intersection of parallel vertical and horizontal lines can be used for attitude estimation (e.g low altitude in urban environments [53]).

In [6], a batch process was developed to recover the history of camera orientations from non-linear optimization (bundle adjustment) of the vanishing points. In [107], their approach is based on vanishing points detection using raw line measurements directly to refine the attitude. They do not require any line tracking. But they fuse these line measurements with IMU gyro angle and compare each line segment with the current best attitude estimate.

Vanishing points were more exploited with the omnidirectional sensors. In [53], they use lines that are available in urban areas which avoids the limitations of horizon determination but it is still not possible to estimate the yaw angle, also it requires to determine the sky. Therefore, their approach is not suitable in dense city environments as well as closed areas. A more recent work proposes the use of vanishing points and infinite homography to estimate the helicopter attitude[16]. This approach can be used in urban environments, however this method has never been applied to a real UAV. In [214], they used the approach described in [16] to estimate helicopter attitude and improved it using a KF.

The research area in using vanishing points for attitude estimation is very active. It provides the intuitive solution for the attitude estimation problem specially in urban environments. Due to its importance, the following subsections will explain them in more details using perspective and omnidirectional sensors. For a comprehensive evaluation of several approaches for vanishing points detection, the reader is referred to [205, 55].

2.3.1 Perspective

The perspective projection of parallel lines intersects at a single point on an image called the vanishing point. In [11], given the camera calibration matrix, the geometric relationship between the vanishing points, the horizon, and camera orientation has been well established in a Gaussian sphere using 2D projective geometry . All vanishing points can be considered in a Gaussian sphere representation even those at infinity. For more details on representing vanishing points on a Gaussian sphere from a calibrated camera (see figure (2.6)), the reader is referred to [11, 168, 107].

2.3.2 Gaussian sphere

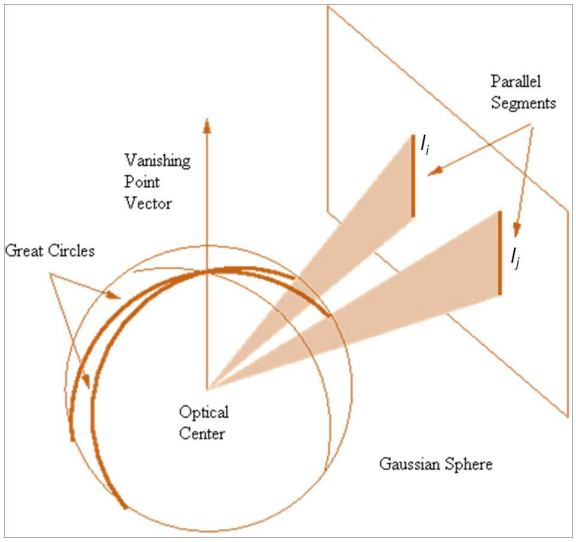

Figure 2.6: Gaussian Sphere adapted from [168]

The Gaussian sphere is a unit sphere which shares the same optical center of the pinhole camera. In the 2D projective space, an image line is represented as a normal vector of a great circle in homogeneous coordinates. The intersection of two parallel edges is a vanishing point which can be computed by the duality between the points and lines in a projective plane $i.e\, v_{ij} = l_i \times l_j$ where v_{ij} is a vanishing point and l_i, and l_j are parallel lines. The vanishing point is the direction to the corresponding 3D point at infinity.

In a calibrated camera, the vanishing points formed by vertical edges and those formed by horizontal edges are geometrically constrained to:

$$v^T_{vertical}.v^i_{horizontal} = 0,\ i = 1, ..., n. \tag{2.3}$$

Vanishing points that lie on the same plane define a vanishing line in an image. Then the horizon is equal to the vanishing line that links any two horizontal vanishing points. The horizon is dual to the vertical vanishing point.

This can be geometrically explained as having the horizon as the projection of the world ground plane, and the normal to the ground plane is projected on the vertical vanishing point i.e:

$$horizon = v^i_{horizontal} \times v^j_{horizontal} \tag{2.4}$$

.

The UAV attitude can be determined when either the vertical vanishing point or at least two horizontal vanishing points are recovered from the image given that a) the great circle in the Gaussian sphere has the same orientation as the world ground plane, and b) the relative camera pose with respect to an UAV is known. In general, it is assumed that the camera is attached to the UAV where the camera's principle axis is aligned along the UAV centerline.

2.3.3 Vertical vanishing points

In urban environments, vertical edges meet at a single vanishing point in the same direction as the gravity in the world coordinates. The vertical vanishing point is the perspective projection of the world z-axis with the camera pose matrix. Let $v_{vertical} = (v_x, v_y)^T$, be the vertical vanishing point , then once it is found, the attitude can be immediately computed by (see figure (2.7)):

$$roll = \phi = atan2(v_x, v_y),\ pitch = \theta = atan\frac{1}{\sqrt{v_x^2 + v_y^2}}\,. \tag{2.5}$$

The horizon line on the image is a line defined by the vertical vanishing point where:

$$sin_\phi cos_\theta x + cos_\phi cos_\theta y + sin_\theta = 0\,. \tag{2.6}$$

2.3.4 Horizontal vanishing points

In urban environments, horizontal edges which are orthogonal to the gravity direction meet at vanishing points in the world ground plane. One of the horizontal vanishing points is the perspective projection of the world x-axis with the camera pose matrix. Then a horizontal vanishing point is:

$$v_{horizontal} = [\frac{cos_\phi sin_\psi - sin_\phi sin_\theta cos_\psi}{cos_\theta cos_\psi},\ \frac{-sin_\phi sin_\psi - cos_\phi sin_\theta cos_\psi}{cos_\theta cos_\psi}]^T \tag{2.7}$$

where ψ is the *yaw* angle. All the horizontal vanishing points are along the horizon and their locations are determined by the different yaw angles.

2.3.5 Catadioptric

As previously mentioned, Projection of 3D world points to the image plane can be done in three steps. Firstly the point is projected to the equivalent sphere, then to the plane at infinity and finally to the image plane. Besides, projection of 3D lines generates great circles on the equivalent sphere (see figure (2.5)). By back projecting every candidate edge on the sphere and checking each edge

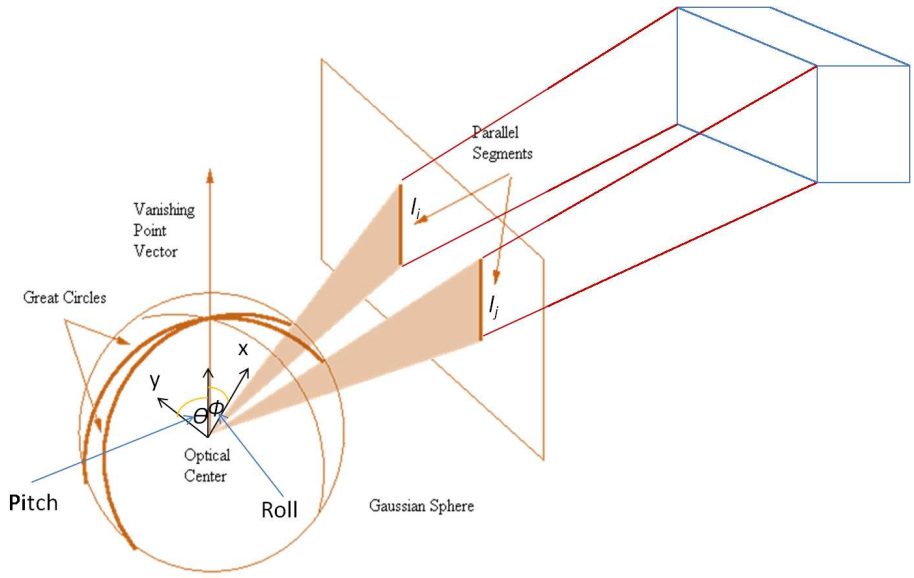

Figure 2.7: Illustration of the relation between a vertical vanishing point and the roll and pitch angles.

if it verifies the great circle constraint, one can decide which edges belong to real 3D lines. In order to do this, the edges divided according to their gradient orientations and selected by their lengths are back projected to the sphere. Then plane normal of the great circle is computed by cross product of first and last edgel directions. In addition, parallel lines have the same vanishing direction on the equivalent sphere. Therefore, dominant parallel lines can be extracted by counting lines which satisfy some similarity threshold based on their vanishing direction. By excluding found parallel lines and repeating the same algorithm, these dominant vanishing directions can be found. Based on an orthogonality threshold, if $|u_1 \times u_2| \leq OrthogonalityThreshold$, the cross product $u_3 = u_1 \times u_2$ is computed to determine the third vanishing direction, where u_is are orthogonal parallel lines. If the inequality is not satisfied, this means that the detection of orthogonal parallel lines failed; therefore attitude estimation at that frame should be skipped. In that case, it is thought that the UAV does not change its orientation.

2.4 Stereo Vision And Optical Flow

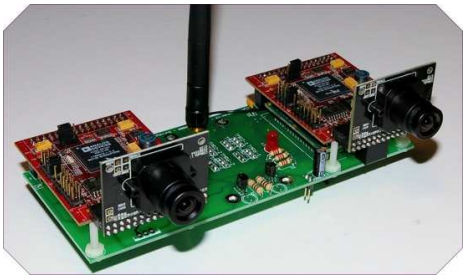

(a) Stereo vision System

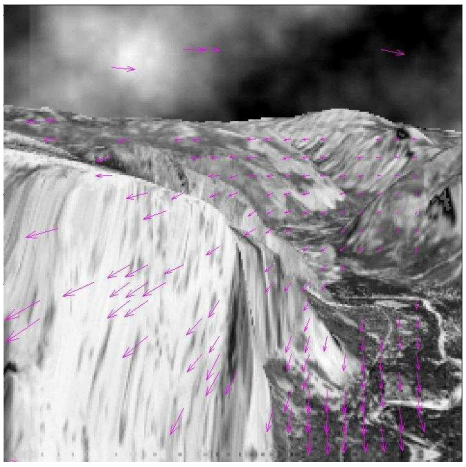

(b) Phase-based estimation of the optical flow field adapted from [3]

Figure 2.8: Stereo Vision and Optical Flow

2.4.1 Stereo vision

Computer stereo vision is a part of computer vision where two cameras capture the same scene but they are separated by a distance as shown in figure (2.8a). A computer compares the images while shifting the two images together over top of each other to find the parts that match. The shifted amount is called the disparity.

In [231], the authors used a dual CCD stereo vision system in order to improve the computation of the attitude by determining the complete pose of the UAV taking advantages of UKF. However, this system relies on the capture of ground targets/landmarks in both images which limits the environment in which the UAV can move. In [63], they presented a mixed stereoscopic vision system made of fish-eye and perspective cameras for altitude estimation. Since there exists a homography between the two captured views, where the sensor is calibrated and the attitude is estimated by the fish-eye camera using the

techniques in [51, 53] , the algorithm searches for the altitude which verifies this homography. It allows real time implementation. In [132, 131] , the conventional stereo system was used for altitude computation. But for attitude computation, they also used a similar approach to [51].

2.4.2 Optical flow

Optical flow is the approximation of the motion field which can be computed from time-varying image sequences (see figure (2.8b)). It provides many important visual cues [72]. It is possible to estimate the flight altitude from the observed optical flow in the downward direction. Faster optic flow indicates a low flight altitude. Obstacles can be detected in the forward direction by detecting expansion, or divergence, in the forward visual field.

Optical flow estimation methods are based on a) differential Techniques (dense motion field) where spatial and temporal variations of the image brightness at all pixels are considered, b) phase methods where response of filters to energy signals are used, c) matching techniques (sparse motion field) where the disparity of special image points (features) between frames is estimated.

In [207, 208], they derived a form of the KF that uses the relationship between vision-based measurements and the motion of the camera. The resulting Implicit Extended Kalman filter (IEKF) can be used to recover the camera motion states. In [82], they reused [207, 208] work in terms of an aircraft state-estimation problem by incorporating aircraft dynamics into the IEKF framework. The resulting formulation partially estimated the aircraft states but exhibited relatively slow convergence. Improvements have been demonstrated by [234, 235] who also used an aircraft model. Unfortunately, accurate MAV models are often not available within an aggressive flight regime where the aerodynamics are difficult to characterize.

Several techniques have utilized the kinematic relationship between camera motion and the resulting optical flow to directly solve for unknown motion parameters using constrained optimization. In [69, 110, 112], these techniques depend on at least partial knowledge of the translational velocity for use in the optimization. This knowledge often depends on GPS measurements. In [113], they addressed the problem of estimating aircraft states during a GPS-denied mission segment. An iterative optimization approach is adopted to determine the angular rates and the wind-axis angles. No knowledge of vehicle velocity is required. The coupled aircraft-camera kinematics are used to solve for aircraft states in similar fashion to previous efforts; however, velocity dependencies are removed through decoupling the optical flow resulting from angular and translational motion, respectively. Angular rate estimates are obtained initially and used to setup a simple linear least-squares problem for the aerodynamic angles. Performance of the least-squares problem is further improved through the application of a weighting scheme derived from parallax measurements.

But Optical flow is inherently noisy, and obtaining dense and accurate optical flow images is computationally expensive. Additionally, systems that rely on optical flow for extracting range information need to discount the components of optical flow that are induced by rotations of the aircraft, and use only those components that are generated by the translational motion of the vehicle. This either requires an often noisy, numerical estimate of the roll, pitch, and yaw rates of the aircraft, or additional apparatus for their explicit measurement, such as a

Papers	Roll	Pitch	Yaw
Horizon detection			
[61, 62, 34, ?, 35, 36, 52, 51, 57, 220]	x	x	
[15, 132, 131]	x	x	x
Vanishing points			
[53, 107]	x	x	
[16, 214]	x	x	x
Stereo vision and optical flow			
[112, 113, 57, 133, 135, 134, 89, 63]	x	x	
[132, 131]	x	x	x

Table 2.1: The estimated attitude angles (Roll, Pitch, and Yaw).

three-axis gyroscope. Furthermore, the range perceived from a downward facing camera or optical flow sensor is only dependent upon altitude, velocity, and the aircraft's attitude [135].

Stereo vision provides an attractive approach to solve some of the problems of providing guidance for autonomous aircraft operating in low-altitude or cluttered environments [133, 135]. In [57], the optical flow of the image for each candidate horizon line is calculated, and using these measurements from the perspective camera, they are able to estimate the body rates of the aircraft. In [209], they estimate the heading of a small fixed pitch four rotor helicopter. Heading estimates are computed using the optical flow technique of phase correlation on images captured using a down facing camera. The camera is fitted with an omnidirectional lens and the images are transformed into the log-polar domain before the main computational step.

2.4.3 Optical flow from stereo vision

In [133, 135, 134], they proposed a stereo vision system from two non-central catadioptric cameras. The profile of the mirror is designed to ensure that equally spaced points on the ground, on a line parallel to the camera's optical axis, are imaged to points that are equally spaced in the camera's image plane. However, they have not used physical mirrors, but instead used high resolution video cameras equipped with wide-angle fish-eye lenses and simulated the imaging properties of the mirrors by means of software lookup tables. Given the measured disparity surface from the optical flow, the attitude (roll and pitch) and altitude can be estimated by iteratively fitting the modeled surface to the measurements. They propose to enhance their method by estimating attitude and altitude with respect to an assumed ground plane by reprojecting the disparity points into 3D coordinates. In [89], he presentes a technique for estimating the aerodynamic attitude in the presence of dynamic obstacles. This technique relies on optical flow and stereo vision to remove dynamic objects from the static background. The resulting flow field is used for attitude computation from the calculated flow centroids.

2.5 Summary and conclusion

Any UAV may fly in low, middle, or high altitudes. We believe that the Omnidirectional sensors should be always used because either the horizon will be always visible (middle and high altitudes) or the vanishing points directions in low altitudes. If the horizon is visible, then attitude should be estimated based on it. We proposed a simpler method for segmentation and horizon detection based on polarization which can be used. In urban environments, techniques based on vanishing points should be used. If obstacle avoidance and altitude estimation are required with attitude estimation, then optical flow approaches from stereoscopic sensors are recommended.

In the work presented in sections (2.2.4, 2.3), the catadioptric sensors used were assumed to be central sensors having a single view point. But in practice, non-central catadioptric sensors are more practical due to higher resolution and simplicity in design. Even the claimed central sensors, might be slightly non-central due to possible misalignment of the lens. All of that pushed the need toward developing methods for attitude estimation from non-central catadioptric sensors.

In summary, a comprehensive review on attitude estimation approaches from visual sensors has been covered. Table (2.1) shows the papers and the estimated angles in the reviewed work. The main general approaches has been shortly discussed. Horizon detection which is the main key for attitude estimation in middle and high altitudes, has been discussed in the light of current ongoing work using different visual sensors. The sky/ground segmentation methods, for horizon detection, found in literature have been reviewed and a novel approach based on polarization applied to UAV attitude estimation has been proposed. In low altitudes the horizon is mostly invisible, hence the line segments found in man-made structures are exploited to obtain vanishing points for attitude computations. Stereoscopic and optical flow based techniques have been also covered. Optical flow computation from stereoscopic systems is proposed in very recent works. To the best of our knowledge, the main work done for UAV attitude estimation from vision sensors (perspective and omnidirectional only) has been covered here.

Chapter 3

Skylight Polarization

3.1 Skylight polarization patterns

As the unpolarized sunlight enters the Earth's atmosphere, it is Rayleigh-scattered by air, and it becomes partially linearly polarized. If the atmosphere is clear (cloudless), this scattering phenomenon results in the well-known spatial distribution of the radiance I, color c, the degree of polarization p , and the angle of polarization α ([94]).

The early measurements were performed by point-source polarimetry ([37], [23], [38]) limited the amount of information on skylight polarization which could be collected due to the few number of observed celestial points. As a result of this technical limitation and the difficulty of theoretical and computational study of the polarization of non-clear skies, the polarimetry of cloudy, smoky, foggy, and overcast skies has been neglected.

The distribution of polarization in the overcast sky was practically unknown ([38], [114], [104]). Although ([37]) measured, at five different solar elevations, the degree of polarization p of skylight under conditions of a heavy stratus overcast along the solar and antisolar meridians, these data were gathered by point-source polarimetry only from a few celestial points and he did not publish data on α from the overcast sky. Using a point-source polarimeter, ([23]) also measured the polarization of light from the overcast sky when the sun was invisible and obtained extremely low p values and α diverging considerably from the theoretical predictions.

A breakthrough of the mentioned technical limitation happened by the development of full-sky imaging polarimeters. Skylight polarization has been extensively studied by this mechanism for clear or partly cloudy skies, where the the development of celestial polarization Rayleigh-scattering is dominant, by ([73, 74], [160], [100], [211], [229], [155], [74]). It became possible to measure the polarization patterns of partly cloudy ([160],[211]), foggy ([90]), smoky ([93]) skies, and overcast skies ([94]).

Hegedüs et al. ([90]) found that the α patterns of foggy and cloudy skies were very similar, while the average p was considerably reduced compared to that of clear skies. They concluded that in principle if p was high enough under foggy and cloudy conditions, Vikings could have navigated by means of skylight polarization. They also ([94]) investigated the polarization patterns

of totally overcast skies. They showed that although p of overcast skies was rather low, their α patterns were quite similar to those of clear skies. They ([93]) studied the effects of forest fire smoke on skylight polarization and their possible consequences on the orientation of polarization-sensitive animals. They established that sky polarization is anomalous in several aspects due to the forest fire smoke. They suggested that the disorientation of certain insects observed by other researchers under smoky skies during the forest fire season could be partly caused by the drastic decrease of p of skylight. They ([91]) found that the α pattern of sunlit tree canopies was qualitatively the same as that of the sky, even in those patches of the celestial hemisphere where dense foliage could be seen. They concluded that this can be important for those polarization-sensitive animals which live in forests and use celestial polarization as compass information. They ([95]) also investigated the polarization characteristics of "water-skies" developing above Arctic open waters (polynyas) and that how these polynyas can be detected visually from a distance. They showed that there are statistically significant differences in the αpattern between the water-sky and the other parts of the sky (ice-sky) surrounding it, which may help biological and man-made sensors to detect far-laying open waters when they are not directly visible.

Hegedüs et al. ([94]) show that the α pattern is a very robust pattern being qualitatively always the same under all possible sky conditions. This is of great importance for the polarization-sensitive animals orientation based on sky polarization under the sun absence conditions. The celestial distribution of the $\boldsymbol{\alpha}$ pattern is formed as isolines. The isolines were always eight shaped with a center at the zenith and an axis of mirror symmetry coinciding with the solar–antisolar meridian in such a way that the smaller loop of the eight figure was always in the solar half of the sky.

At low solar elevations (when the elevation angle of the sun from the horizon is not larger than about 25°), there are always two unpolarized (neutral) points in the clear sky: the Babinet point above the sun and the Arago point above the anti-sun. Both neutral points are placed along the solar and antisolar meridians at a position where the negative polarization of skylight switches to positive polarization. The Babinet and Arago neutral points are placed at the intersections of the neutral lines (Neutral lines separate regions conventionally referred to as having positive and negative polarization) and the solar– antisolar meridian. Since the mirror symmetry axis of the α pattern is always the solar-antisolar meridian, the azimuth direction of the sun can be assessed from this polarization pattern ([91]) (Note that only the solar azimuth, i.e. the direction of the solar meridian can be determined, rather than the solar position, possessing two components: the azimuth and the elevation).

The results presented in ([160], [211], and [93, 94, 90]) clearly show that the $\boldsymbol{\alpha}$ pattern is very robust being qualitatively always the same under all possible sky conditions. The only qualitative difference among clear, partly cloudy, foggy, smoky, and totally overcast skies is in p : the higher the optical thickness of the non-clear (partly cloudy, smoky, foggy, or overcast) atmosphere, the lower the p value.

3.2 Skylight polarization from a Fisheye lens

To measure the skylight polarized radiance distribution, [229] developed a sequential full-sky imaging polarimeter. It is based on a 178° field-of-view fisheye camera lens, a CCD sensor controlled by a computer interface card and a remotely controlled filter changer. The polarimeter Mueller matrix can be changed by placing linearly polarizing filters in one of the filter wheels. Three polarizational images with different orientations of the polarizers transmission axes are taken to obtain one complete measurement in a period of 1.52 min. From these three images the first three components of the Stokes vector as well as the linear polarization degree p and angle α of the incident light are computed. During the measurements the direct solar radiation is blocked by a sun blocker to avoid camera lens flaring and overexposure of the CCD. This polarimeter needs a main power supply and connection with a computer and hence is not portable, furthermore its CCD has to be thermoelectrically cooled.

A 180° field-of-view sequential rotating analyzer imaging photopolarimeter was designed by [74], with which numerous measurements have been performed (e.g. [73, 74, 75], [159, 161], [20], [14], [13]) due to the portability of the instrument and because it is easy to manage. An angle of view of 180° is ensured by a fisheye lens including a built-in rotating filter wheel mounted with three neutral density linearly polarizing filters with three different orientations (0°, 45°, and 90° measured from the radius of the wheel) of their transmission axis. Three photographs are taken for the three different alignments of the transmission axis of the polarizers on the built-in filter wheel. In order to eliminate distorting internal reflections of direct sunlight from the refracting surfaces of the fisheye lens, a sun blocker was used. The overall time needed for one complete measurement is about $6-8$ sec under normal illumination conditions. Then the patterns of the intensity I, degree p and angle α of linear polarization are calculated the same as in video polarimetry case ([103]).

The major problem of the previously described polarimeters is their slowness due to sequentially recording the three polarizational images of the full sky . Depending on the time of exposure, one cycle of three exposures and, in between, exchanging the polarizer may take several seconds or minutes. Thus, these instruments cannot be used if the cycle duration is comparable with the time, during which the optical characteristics of the sky change considerably. Such situations occur in the following cases: a) The sky is cloudy and the clouds move fast. b) Moving aerial objects (e.g. birds or airplanes). c) Immediately after sunset or prior to sunrise when the radiance of skylight changes rapidly and moreover the time of exposure increases considerably due to the relatively low radiance of skylight. d) The platform of the polarimeter, being on the board of a moving ship ([98]).

In order to eliminate the slowness problem, ([99]) designed a 3-lens 3-camera full-sky imaging polarimeter, which takes the three polarizational images (at 0°, 60° and120°) simultaneously rather than sequentially. Thus, celestial polarization patterns can be captured even if rapid temporal changes occur in the sky. The polarimeter consists of three cameras where each of them equipped with a 180° fisheye lens. Each fisheye lens consists of two lens groups with a circular filter mount in between. Into the mounts neutral density linearly polarizing filters are inserted. The simultaneous triggering of all three cameras is mechanically ensured by synchronous pressing the remote exposure cords but-

tons. A sun blocker was used to block the direct sunlight. The evaluation of the three polarizational images taken with this 3- lens 3-camera full-sky imaging polarimeter is the same as in the case of the 1-lens 1-camera full-sky imaging polarimeter of [74].

The scientific results presented in the ([93, 94, 95, 90, 91]) were obtained by the same experimental technique of 1-camera 1-lens as in ([74]). A 180° field of view was ensured by a fisheye lens with a built-in rotating disc mounted with three broad-band neutral density linearly polarizing filters with three different polarization axes (at 0°, 45°, and 90°). Three images were taken at the three different directions and the patterns of the radiance (or intensity) I, linear polarization degree p and angle α (or E-vector alignment) of skylight were determined.

As we saw, many theoretical and experimental studies ([160], [74], [93, 94, 95, 90, 91]) have been done using one or more fish-eye lenses. ([129]) show results of p and α patterns obtained by a camera with a fish-eye lens which affirms the experimental studies of ([160], [74], [94]). In addition, unlike the previous studies, they tilt the fish-eye lens camera and analyze the α patterns. The technique used in ([129]) was similar to the technique described in ([160], [74], [100], [94]) . However in ([129]), using a commercial Digital Single-Lens Reflex (DSLR) camera, it was imperative to setup the polarizing filter in front of the fish-eye lens. Hence, their imaging polarimeter allowed only a viewing angle of 130°which is the first drawback as it limited the field of view. Three images were taken for three different polarizer transmission axis alignments and it was rotated manually which is the second drawback.

The contribution of ([129]) is to analyze the p and α patterns when the camera is tilted from the horizon. All the studies of skylight polarization patterns ([160], [74], [94]) were performed using a camera setup in the horizontal plane (i.e., the optical axis of the fish-eye lens was vertical to the ground). This condition is considered as a serious limitation as the interest should be not only in the skylight patterns but also in the object appearance (reflectance) in the outdoor environment which requires a free camera movement. When an image is taken in the outdoors, only a small part of the sky is visible, and the camera is not horizontal. Hence, it is worth investigating sky polarization patterns using a camera in a general position (i.e., the optical axis of the fish-eye lens is not necessarily vertical).

3.3 Skylight polarization from Catadioptric sensors

North and Duggin [155] used a four-lens camera with negative color roll films. Four neutral density linearly polarizing filters were used to cover the four apertures of the camera. Their transmission axes were oriented at 0°, 45°, 90° and 135° with respect to a given reference direction. Hence, all sky polarizational images were taken simultaneously. The polarimeter was suspended $2.7\,m$ over a spherical security convex mirror ($46cm$ diameter, back-surface aluminium coating on an acrylic matrix) by four thin rods. This height was required to mitigate the parallax effects created by the finite separation of the four lenses. A $6\,m$ air-driven shutter release was used to minimize obscuration by the photographer.

Although the spherical mirror of this imaging polarimeter encompassed almost 180°field of view , the polarimeter could not capture the entire skydome, since the camera above the mirror and the tetrapod screened out certain areas of the equipment. The results on skylight polarization obtained by ([155]) have been never published.

In a different context, ([123]) proposed another design based on cone mirror and CCD camera for surveillance equipped with a linear/circular polarizer. They capture three images at 0°, 45°, and 90° . However, in (p.220) it was wrongly stated that "For reflective mirror with metallic reflection surface, however, the effects on polarization are simpler. For many highly reflective metallic surfaces the polarization of reflected light is the mirror image of the original polarization pattern." The light polarization state is changed after being reflected from metallic surfaces (e.g a linearly polarized light reflects as an elliptically polarized light) ([22], p.741). This problem is solved by calibrating the original incident light polarization state from the reflected state as will be shown in this work.

Carey and Sturzl ([25]) tried to determine whether a small lightweight omnidirectional system could resolve the polarization pattern of the clear sky with sufficient accuracy. Their imaging system consisted of a linear polarizer, UV transmitting glass filter, two different cameras, each directed towards identical constant-gain omnidirectional mirrors, and attached to a swiveling mount. A sun-blocker was attached to the used tripod. The polarizer was manually rotated to obtain four different images which are 45° apart.

Although the aluminium coating on the mirror induce a small amount of circular polarization, the fourth component of the Stokes vector was assumed to be zero ([155, 123, 25]). This simplifying assumption allowed to obtain images of the partial Stokes vector by using only linear polarizers. Since the polarimeters of ([155, 123, 25]) were not calibrated, the Stokes vector S_{sky} of the incident skylight could not have been measured. With this system only the spatial distribution of the Stokes vector S_{image} of skylight reflected from the mirror could be determined, which is the major disadvantage of their polarimeters. From the resulting partial Stokes vector S_{image} the intensity image I, linear polarization degree p and angle α were derived, which inform qualitatively about skylight. Thus, a controlled experiment remains to be executed to provide absolute polarimetric calibration, to obtain full polarimetric characterization of the optical system, and to invert S_{image} to derive S_{sky}. To the best of our knowledge, this work has not been done until now. Hence, a method is proposed in this work to perform this polarimetric calibration.

Furthermore, the equipment is voluminous and cumbersome in ([155], [229], [74]), which does not permit easy and rapid setting up, disassemble, transfer and transport. Even more recent smaller constructions ([129]) have been heavy and unsuitable for mobile applications. Conversely, polarization systems built for small robotic systems have tended to have a limited field of view and produced a highly simplified sky map ([115], [30]). Although ([25]) proposed a smaller lightweight omnidirectional system, it was quite complex and contains some manual and mechanical interference.

Our imaging system which was firstly proposed in ([193]) is much simpler as it consists of a mirror and a polarizational camera ([1]).

3.4 Omni-Pola-Catadioptric

The previous polarimeters (e.g [155], [160], [74], [100], [94], [129], [25]) utilize optical imaging systems that are external to the detectors. Design compactness and fastly generated polarization images can be improved greatly by incorporating an array of microscopic polarization filtering optics directly onto a photosensitive chip ([245]) or designing color cameras to use a non-polarizing beam-splitter that directs equal amounts of incoming light onto three separate CCD sensors for the red, green and blue spectral ranges and placing a linearly polarizing filter over every CCD where each filter has a unique direction of its transmission axis. Hence, a polarizational camera can be built that operates in white light or in a given part of the spectrum ([242], [84]). A polarizational camera is a generalization of the conventional intensity camera. If necessary, the former can function as the latter. Adding color-sensing capability to a polarizational camera makes it possible to sense the complete set of light electromagnetic parameters incident on the camera. Polarizational cameras have more general capabilities than standard intensity cameras, and can be applied for different purposes ([243]).

Polarimetric or polarization imaging is an active research area in medical, machine vision and defense applications. Polarization provides additional information to analysts and researchers because the polarimetric preserving and/or inducing properties of materials are often complementary to their spectral signatures. Polarization can be part of a high-level visual perception, permitting a wide area of vision applications. Polarization imaging can be used for most tasks of color vision like: object recognition, contrast enhancement, camouflage breaking, and signal detection and discrimination. It has been used to identify stress and defects in aircraft assemblies; "see" into the water column in many applications, such as oil spill detection; separate specular from diffuse reflectance for material analysis and identification; and many other applications ([243], [197], [1]).

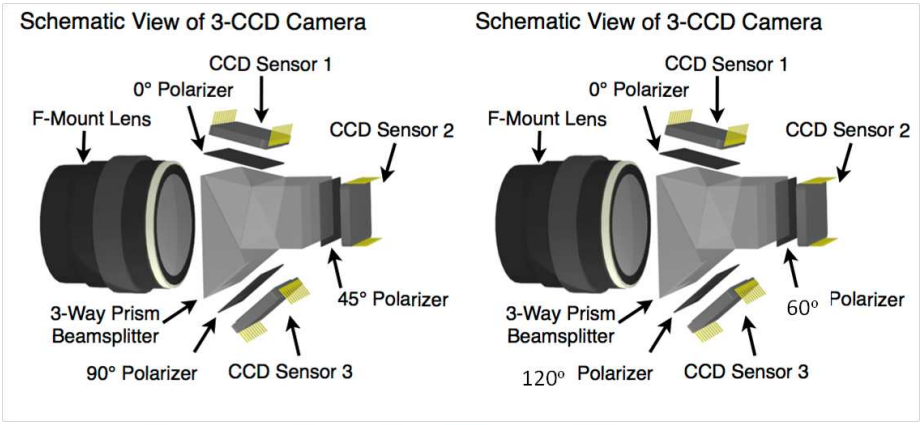

Figure 3.1: FD-1665 3CCD [1]

We propose to use a combination of polarizational camera (FD-1665 3CCD [1] figure (3.1)) and a convex shaped mirror (see sec (B.1)) to obtain the 360°polarimetric view. The prisms of the FD-1665P optical assembly are fabricated with neutral, non-polarizing beam splitter coatings. The first coating surface reflects 30 % of the light and transmits 70 %. The second coating provides a 50 % transmittance and 50 % reflectance. This combination results in splitting the incoming broadband light into three components with equal spectral and spatial content. Linear polarization trim filters with $> 99\,\%$ polarization efficiency and contrast ratio of up to 3000 : 1 are placed in front of each sensor. The filters are oriented at three equal angular spacing (0°, 60°, 120° or 0°, 45°, 90°) and cover the spectral range $380 - 1000\,nm$. The FD-1665P polarization camera is configured with monochrome sensors for each channel. Different configurations of the FD-1665P polarization camera are also possible ([1]). Such a polarizational total sky imager, based on the camera configuration, can monitor continuously the radiance, spectral and polarizational properties of the full sky.

3.5 Deriving the Angle of Polarization: A new approach

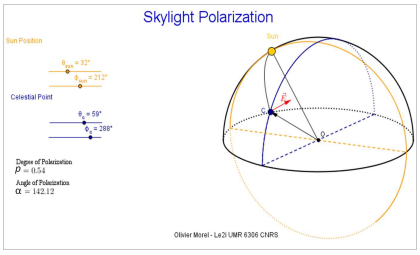

(a) The clear sky provides polarized light according to the Rayleigh scattering model. The degree and angle of polarization (p and α angles respectively) measured at a celestial point C are related to the Sun position, the angle of scattering and the plane of scattering defined by O, C and Sun. The electric vector is represented by $\vec{E}$ and is orthogonal to the plane of scattering [137].

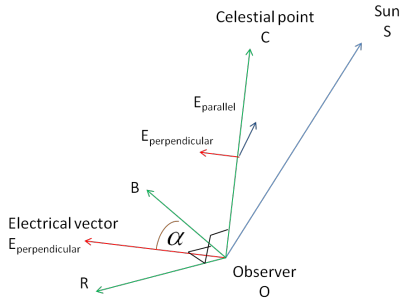

(b) Scattering plane contains C, S, and O. $E_{parallel}$ oscillates in this plane. E is perpendicular to the scattering plane, R is perpendicular to C, and B is perpendicular to C and R. α is the angle of the plane of polarization taken with respect to the vertical direction. In other words, it is defined as the angle between the $\vec{E}$ direction and $\theta - axis$ in the local polar coordinate system formed by $\theta - axis$ and $\psi - axis$.

Figure 3.2: AOP geometrical sketch.

The clear sky provides polarized light according to the Rayleigh scattering model. The degree p and angle of polarization α measured at a celestial point C are related to the Sun$S$ position, the angle of scattering and the plane of scattering defined by O, C and S. The electric vector is represented by $\vec{E}$ and is orthogonal to the plane of scattering [137]. See figure (3.2a).

Figure (3.2b) sketches the scattering plane which contains C, S, and O. $E_{parallel}$ oscillates in this plane. E is perpendicular to the incident plane, R is perpendicular to C, and B is perpendicular to C and R. α is the angle of the plane of polarization taken with respect to the vertical direction. In other words, it is defined as the angle between the $\vec{E}$ direction and $\theta - axis$ in the local polar coordinate system formed by $\theta - axis$ and $\psi - axis$.

$$S = \begin{bmatrix} cos(\psi_s)sin(\theta_s) \\ sin(\psi_s)sin(\theta_s) \\ cos(\theta_s) \end{bmatrix}, C = \begin{bmatrix} cos(\psi)sin(\theta) \\ sin(\psi)sin(\theta) \\ cos(\theta) \end{bmatrix}, R = \begin{bmatrix} -cos(\psi)cos(\theta) \\ -cos(\theta)sin(\psi) \\ sin(\theta) \end{bmatrix}, E = S \times C,$$
$$B = C \times R,$$

where S, C, and R are the Sun, Celestial, and Observer vectors respectively. Hence, the angle of polarization α is:

$$\alpha = atan(\frac{E.R}{E.B}) \tag{3.1}$$

$$= atan(\frac{sin(\psi - \psi_s) * sin(\theta_s)}{cos(\psi)cos(\psi_s)cos(\theta)sin(\theta_s) - cos(\theta_s)sin(\theta) + cos(\theta)sin(\psi)sin(\psi_s)sin(\theta_s)})$$

$$= atan(\frac{sin(\psi - \psi_s) * sin(\theta_s)}{cos(\theta)sin(\theta_s)cos(\psi - \psi_s) - cos(\theta_s)sin(\theta)}) \tag{3.2}$$

3.6 Comparison of the derived AOP and the literature

While investigating the literature, it was found that the theoretical Rayleigh formulation for the angle of polarization α was only recently derived by ([129]) as a direct trigonometric formula. It was also indirectly derived by [21] computing the phase of a complex quartic polynomial. Otherwise only the theoretical Rayleigh simulation was introduced without a clear mention of the formula ([160, 100, 101, 99, 104, 93, 94, 95, 90, 91]). [21] proposed a complex quartic polynomial, formed by the four singularity points in the sky, commonly known as neutral points (which are the Brewster and the Babinet points below and above the sun respectively, and the Arago, the fourth neutral point above and below the anti-sun respectively), to represent the polarization patterns emphasizing that the polarization global patterns are strongly constrained by the arrangement of these local singularities. Although [21] formulation shows good accuracy, it is quite complex to be directly applied. Recently ([25]) have proposed a new sensor and compared their results with the theoretical formulation given by ([129]) as a ground truth.

By visually comparing the given theoretical simulation in ([160, 129, 25]) and the actual captured α patterns, a sufficient amount of inaccuracy is noticed as shown in figures (3.3, 3.4). Hegedüs et. al ([93, 94, 95, 90, 91]) have simulated the α patterns based on ([21]) and compared them to the α captured patterns with high accuracy. The limitations of [21] formulation are the complexity of their formulation and assuming the knowledge of the neutral points positions to obtain higher accuracy. Berry et. al [21] compared their theoretical results to [27]'s results which were calculated by multiple-scattering theory. A comparison between our, [27], [21], and [129] results is shown in figure (3.5).

Due to the inaccuracy found in [129] formulation or reported results by [160] and the complexity of [21], a new derivation of the angle of polarization α is introduced to obtain higher accuracy than the reported results in ([160, 129, 25]) as shown in figures (3.3, 3.4, 3.5) which is simpler than [21] and has no previous assumptions. In the given comparisons in figures (3.3, 3.4, 3.5) between our results and ([27], [21], [129]), the reader is urged to compare the shape of the α pattern (the α global pattern) which should be as close to the captured α pattern as possible but not the color of peer areas which might be different due to different local references. Starting from figure (3.4) till the end of this work, a modified colormap of ([160]) to represent the α pattern is used to emphasis the $\pm 45°$contour which is the most significant feature in the skylight polarization pattern as will be shown in chapter (5).

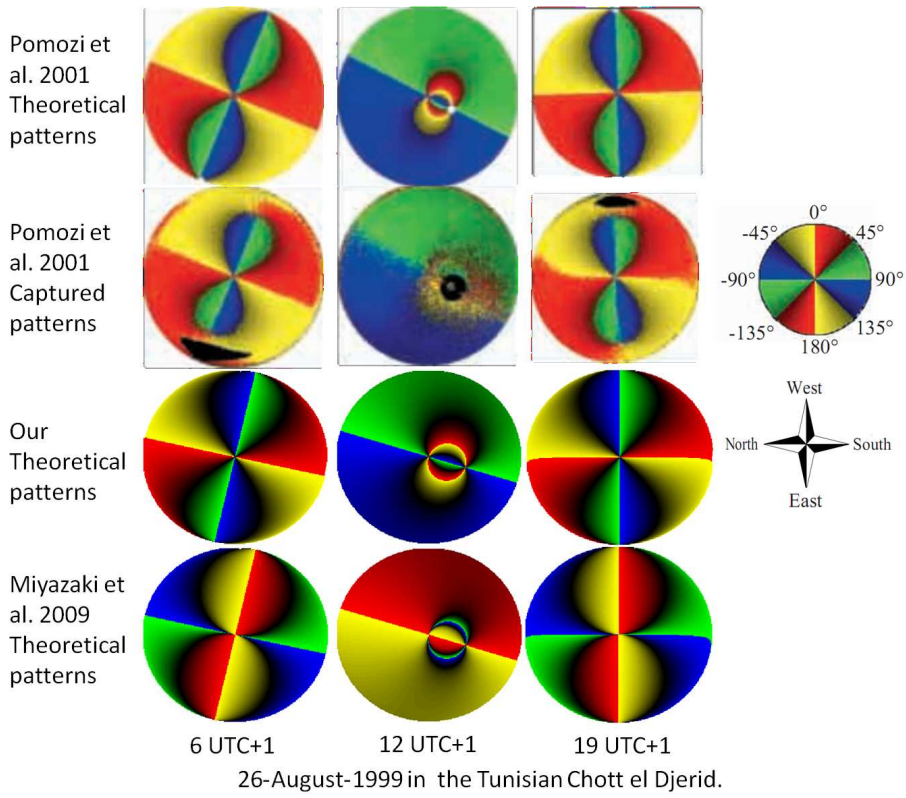

Figure 3.3: Comparing our results against [160, 129]. The α patterns simulations in first, third, and fourth raw represent the captured α patterns in the second raw on 26-August-1999 (at 6, 12, 19 UTC+1 from left to right respectively) in the Tunisian Chott el Djerid (Latitude:33.867, Longitude:8.367) as reported in [160]. East is on the down rather than up in the figure (left rather than right of the compass) because we are looking up through the celestial dome rather than down onto a map.

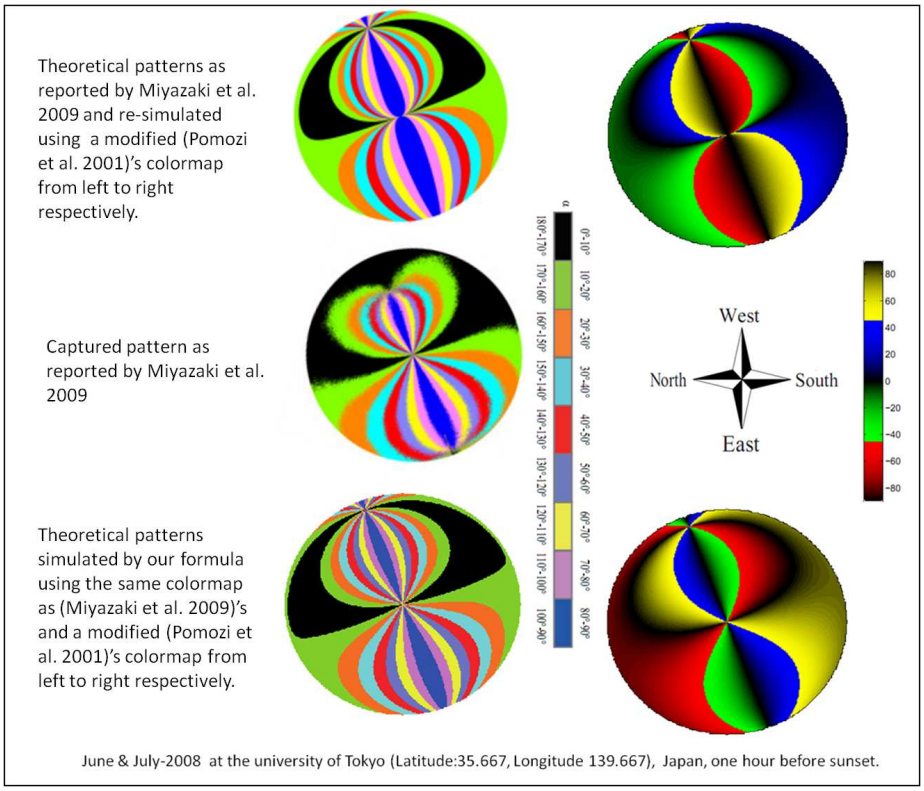

Figure 3.4: Comparing our results against [129]. The α patterns simulations in first and third rows represent the captured pattern (as reported in [129]) in the second raw in June & July 2008 one hour before sunset at the university of Tokyo (Latitude:35.667, Longitude:139.667), Japan. Two different colormaps are used to simulate ([129])'s and our formula to emphasis the difference. East is on the down rather than up in the figure (left rather than right of the compass) because we are looking up through the celestial dome rather than down onto a map.

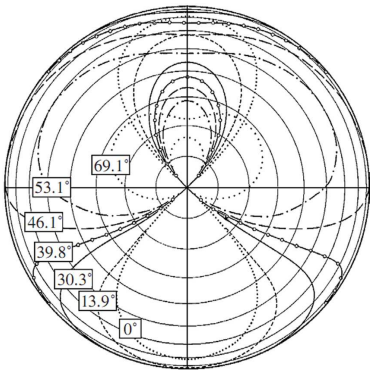

(a) Neutral lines (contours of theα pattern at $\pm 45°$ to the vertical) , calculated by multiple-scattering theory ([27]), for the indicated Sun elevations.

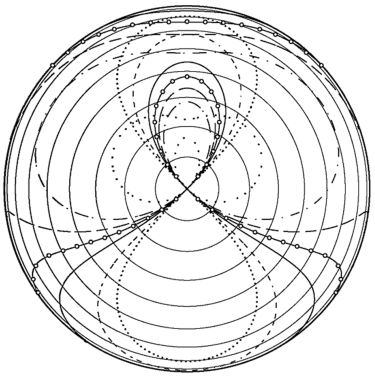

(b) Neutral lines for the same Sun elevations as in (3.5a), calculated on the balanced singularities (complex quartic polynomial) theory [21] with the same locations of the singularities (neutral points) as in (3.5a)

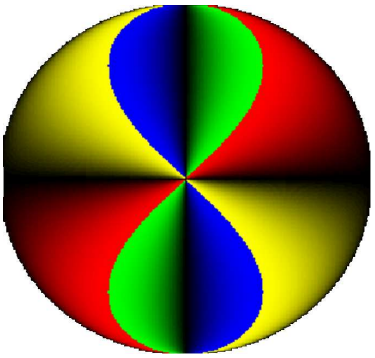

(c) Our simulation at 0°elevation angle. The contours of theα pattern at $\pm 45°$ to the vertical are around the green-blue pattern as indicated by the colorbar.

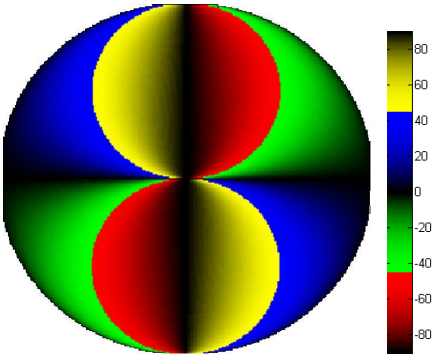

(d) [129]'s simulation at 0°elevation angle. The contours of theα pattern at $\pm 45°$ to the vertical are around the yellow-red pattern as indicated by the colorbar.

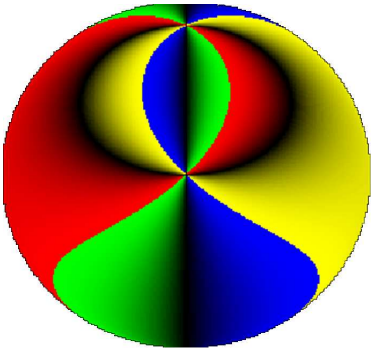

(f) Our simulation at 30.3°elevation angle. The contours of theα pattern at $\pm 45°$ to the vertical are around the green-blue pattern as indicated by the colorbar.

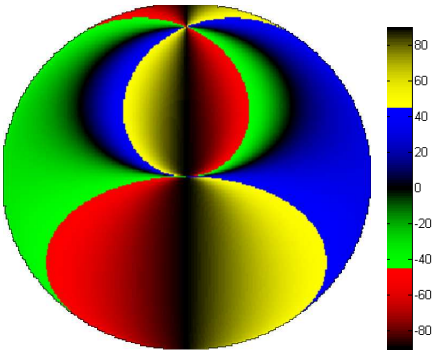

(g) [129]'s simulation at 30.3°elevation angle. The contours of theα pattern at $\pm 45°$ to the vertical are around the yellow-red pattern as indicated by the colorbar.

Figure 3.5: A comparison between our results and ([27], [21], [129]).

Chapter 4

Skylight Stokes Calibration

Any catadioptric sensor is composed of a reflective surface and a perspective/telecentric lens. Usually the reflective surface is metallic and hence the incident skylight polarization state, which is mostly partially linearly polarized, is changed to be elliptically polarized after reflection [22]. Our aim is to calibrate the polarization state of the incident light, in other words, given the measured reflected polarization state we want to obtain the incident polarization state.

4.1 Ambiguity caused by a reflective surface

Once the incident light is reflected from a metallic surface, its polarization state is changed as shown in figure (4.1).

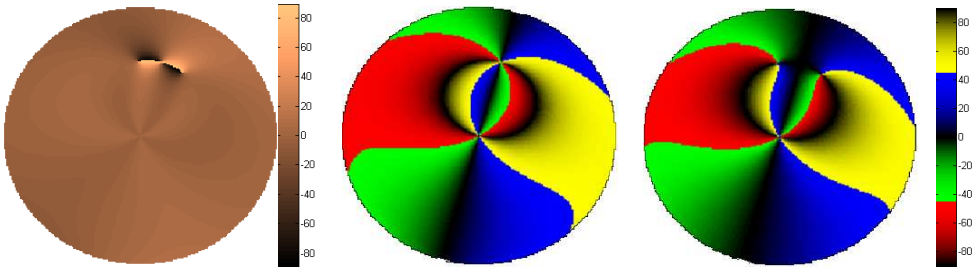

(a) Difference between incident and reflected α

(b) Incident α

(c) Reflected α

Figure 4.1: The difference between the incident and reflected Angle of Polarization pattern (α pattern) using a metallic (Aluminum) spherical mirror with refractive index $\hat{n} = 1.44 + 5.23i$. Simulation parameters are as shown in table (4.1).

Another valid assumption is that the metallic surface can be covered by a dielectric layer or the mirror can be replaced by a non-metallic mirror. In these cases the reflected light will keep the original polarization state but with different

values resulting into high ambiguity in the reflected polarization pattern as shown in figure (4.2).

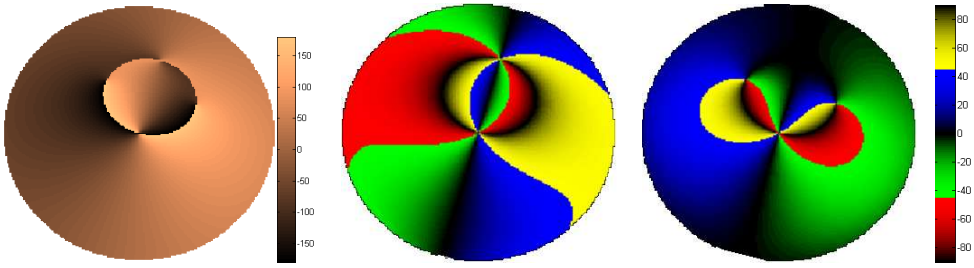

(a) Difference between incident and reflected α

(b) Incident α

(c) Reflected α

Figure 4.2: The difference between the incident and reflected Angle of Polarization pattern (α pattern) using a non-metallic spherical mirror with refractive index $\hat{n} = 1.44$. Simulation parameters are as shown in table (4.1).

Location	Le Creusot, France
Latitude +N	46.8
Longitude +E	4.4333
Date	16 May 2012
Time	16:4:20.218 GMT
Altitude	40.1037
Zenith	49.8963
Azimuth East North	164.5745
Mirror	Spherical
Refractive index fig (4.1)	$\hat{n} = 1.44 + 5.23i$
Refractive index fig (4.2)	$\hat{n} = 1.44$

Table 4.1: Simulation parameters of figures (4.1, 4.2)

It is noticed that the ambiguity in the reflected pattern from the metallic surface in figure (4.1) is less than the ambiguity in the reflected pattern from the non-metallic surface in figure (4.2). The reflected polarization pattern from a metallic surface has been studied by ([230]) and they showed that for angles of incidence less than approximately 50°, the relevant polarization parameters are not significantly affected by reflection from the mirror. We expect that under normal conditions, most of the sky-view should fall within this range, however it was not exactly the case as shown in figure (4.3), where we simulated the reflected polarization angle α from a metallic sphere at different incident angles .

On the other hand, for a non-metallic surface, the relevant polarization parameters are significantly changed for incidence angles greater than approximately 25°as shown in figure (4.4).

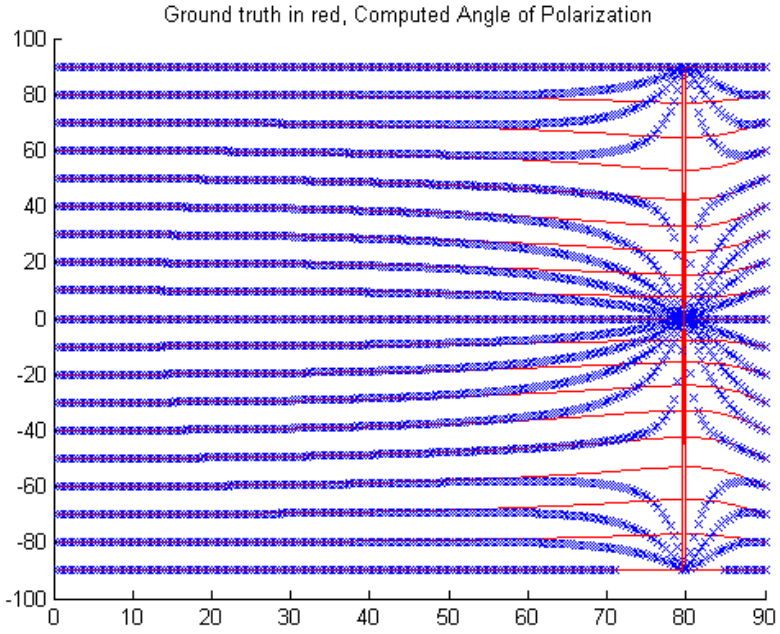

Figure 4.3: The reflected polarization angle $-90 \leqslant \alpha \leqslant 90$ over the full range of incident angles. The polarization angle α is not significantly affected by reflection from the metallic mirror for incidence angles less than approximately 50°. Aluminum surface with refractive index $\hat{n} = 1.44 + 5.23i$.

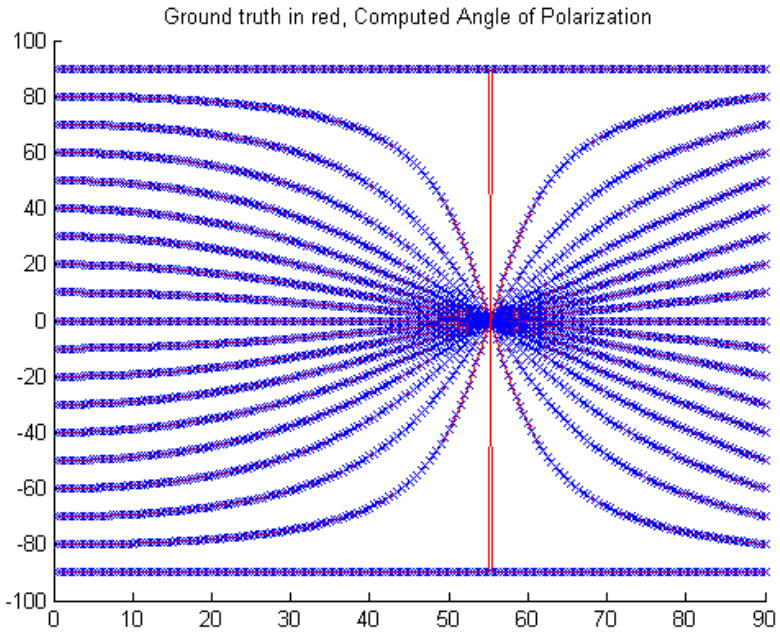

Figure 4.4: The reflected polarization angle $-90 \leqslant \alpha \leqslant 90$ over the full range of incident angles. The polarization angle α is significantly affected by reflection from the non-metallic mirror for incidence angles more than approximately 25°. Non-metallic surface with refractive index $\hat{n} = 1.44$.

Figures (4.1, 4.2, 4.3, 4.4) show clearly the source of ambiguity in both metallic and non-metallic reflective surfaces. This ambiguity pushed the need for polarimetric calibration of the incident light.

In this work, our aim is to perform polarimetric calibration in the sense of finding the incident skylight polarization pattern given the reflected ambiguous pattern from all reflective surfaces specially metallic surfaces as will be explained in this chapter. Then the calibrated polarization patterns can be used for several applications as will be discussed in chapter (5).

4.2 Incident Stokes Calibration

4.2.1 Muller calculus

The polarization state of an incident beam is characterized by its Stokes vector S_i, it interacts with the polarizing medium $M_{4\times4}$ known as the Mueller matrix for that medium, and the emerging beam is characterized by a new vector S^{out}[78]. S^{out} can be expressed as a linear combination of the four parameters of the incident beam where:

$$S^{out} = M_{4\times4}.S_i = M_{4\times4}.\begin{pmatrix} S_0 \\ S_1 \\ S_2 \\ S_3 \end{pmatrix} \tag{4.1}$$

.

The first parameter S_0 expresses the total intensity of the optical field. The remaining three parameters describe the polarization state. The parameter S_1 describes the amount of linear horizontal or vertical polarization, the parameter S_2 describes the amount of linear $+45°$ or $-45°$ polarization, and the parameter S_3 describes the amount of right or left circular polarization contained within the beam [78].

For any state of polarized light the parameters always satisfy the relation: $S_0^2 \geq S_1^2 + S_2^2 + S_3^2$. The equality sign applies when we have completely polarized light, and the inequality sign when we have partially polarized light or unpolarized light.

4.2.2 Calibration process

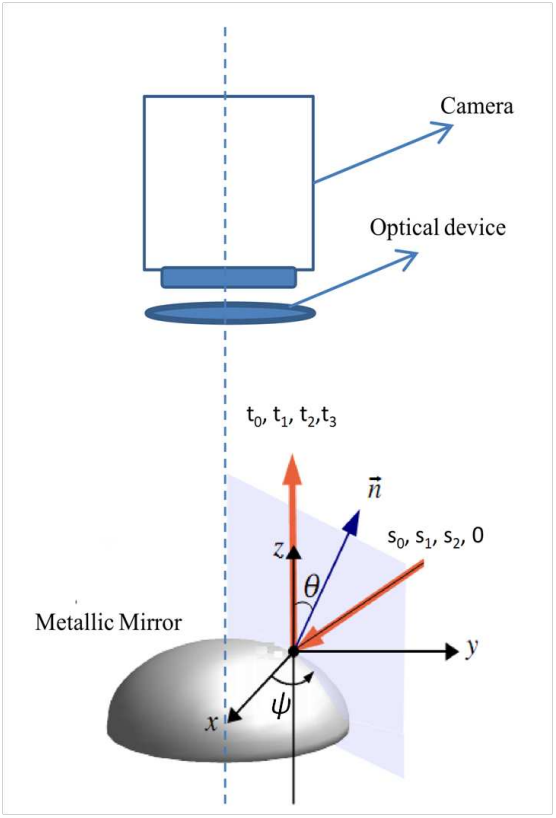

Figure 4.5: Pola-Catadioptric design.

We want to measure the three Stokes parameters (S_0, S_1, S_2) of a partially linearly polarized light using a simplified Pola-Catadioptric sensor, see figure

$$S_{out} = M_{rot}.M_{refl}.S \tag{4.8}$$

$$= \begin{pmatrix} \frac{(F_\perp - F_\parallel)S_1}{2} + \frac{(F_\perp + F_\parallel)S_0}{2} \\ -cos(\delta)\sqrt{F_\parallel F_\perp} sin(2\psi) S_2 + \frac{(F_\perp + F_\parallel)cos(2\psi)S_1}{2} + \frac{(F_\perp - F_\parallel)cos(2\psi)S_0}{2} \\ cos(\delta)\sqrt{F_\parallel F_\perp} cos(2\psi) S_2 + \frac{(F_\perp + F_\parallel)sin(2\psi)S_1}{2} + \frac{(F_\perp - F_\parallel)sin(2\psi)S_0}{2} \\ -sin(\delta)\sqrt{F_\parallel F_\perp} S_2 \end{pmatrix} \tag{4.9}$$

$$= \begin{pmatrix} t_0 \\ t_1 \\ t_2 \\ t_3 \end{pmatrix}$$

(4.5), in which a new optical element (the metallic reflector) is introduced. The Mueller matrix of the specular reflection, in the plane of incidence, is given by the product of two matrices: the Mueller matrix of a partial polarizer and the Mueller matrix of a perfect retarder [136] as shown in equations (4.2, 4.3, 4.4).

$$M_{refl} = M_{pp}(F_\perp, F_\parallel).M_{ret}(\delta, 0) \tag{4.2}$$

$$M_{pp} = \begin{pmatrix} \frac{F_\perp + F_\parallel}{2} & \frac{F_\perp - F_\parallel}{2} & 0 & 0 \\ \frac{F_\perp - F_\parallel}{2} & \frac{F_\perp + F_\parallel}{2} & 0 & 0 \\ 0 & 0 & \sqrt{F_\parallel F_\perp} & 0 \\ 0 & 0 & 0 & \sqrt{F_\parallel F_\perp} \end{pmatrix} \tag{4.3}$$

$$M_{ret} = \begin{pmatrix} 1 & 0 & 0 & 0 \\ 0 & 1 & 0 & 0 \\ 0 & 0 & cos(\delta) & sin(\delta) \\ 0 & 0 & -sin(\delta) & cos(\delta) \end{pmatrix} \tag{4.4}$$

where $F_\perp$ and $F_\parallel$ are respectively the perpendicular and parallel polarized reflected components and δ is the phase shift.

Therefore, the Mueller matrix of the specular reflection in the plane of incidence is:

$$M_{refl} = \begin{pmatrix} \frac{F_\perp + F_\parallel}{2} & \frac{F_\perp - F_\parallel}{2} & 0 & 0 \\ \frac{F_\perp - F_\parallel}{2} & \frac{F_\perp + F_\parallel}{2} & 0 & 0 \\ 0 & 0 & cos(\delta)\sqrt{F_\parallel F_\perp} & sin(\delta)\sqrt{F_\parallel F_\perp} \\ 0 & 0 & -sin(\delta)\sqrt{F_\parallel F_\perp} & cos(\delta)\sqrt{F_\parallel F_\perp} \end{pmatrix} \tag{4.5}$$

Hence, we have:

$$S_{out} = M_{refl}.S = \begin{pmatrix} \frac{F_\perp + F_\parallel}{2} S_0 + \frac{F_\perp - F_\parallel}{2} S_1 \\ \frac{F_\perp - F_\parallel}{2} S_0 + \frac{F_\perp + F_\parallel}{2} S_1 \\ cos(\delta)\sqrt{F_\parallel F_\perp} S_2 \\ -sin(\delta)\sqrt{F_\parallel F_\perp} S_2 \end{pmatrix} \tag{4.6}$$

The Stokes parameters are defined in the plane of incidence. In order to have all computed Stokes parameters in the same reference plane, a rotation by the azimuth angle ψ, see figure (4.5), should be applied using a rotation matrix M_{rot}:

$$M_{rot} = \begin{pmatrix} 1 & 0 & 0 & 0 \\ 0 & cos(2\psi) & -sin(2\psi) & 0 \\ 0 & sin(2\psi) & cos(2\psi) & 0 \\ 0 & 0 & 0 & 1 \end{pmatrix} \tag{4.7}$$

Finally, we have equation (4.8). Equations (4.6, 4.8) prove what we stated earlier about having the reflected light elliptically polarized as the last parameter in equation (4.8) is non-zero $-sin(\delta)\sqrt{F_{\parallel}F_{\perp}}S_2$. Furthermore, it implies that $F_{\perp}$, $F_{\parallel}$, δ, and, ψ must be known to estimate S_0, S_1, and S_2.

At the first glance, it might be thought that it is necessary to measure the four Stokes components of the reflected beam in order to calibrate the three Stokes components of the incident beam. However, by rechecking equation (4.8) it is proved that only three out of the four Stokes components of the reflected light should be measured to perform the incident Stokes calibration. This fact is important to reduce the number of optics required to measure the polarizational state of the reflected beam. In fact, it is possible to measure it using a polarizational camera (e.g [1]) which is capable of measuring the reflected Stokes at one shot without introducing any manual or mechanical rotations of the involved optics.

From the Fresnel formula [22]:

$$f_{\parallel} = \frac{tan(\theta - \theta_t)}{tan(\theta + \theta_t)}, \tag{4.10}$$

$$f_{\perp} = -\frac{sin(\theta - \theta_t)}{sin(\theta + \theta_t)} \tag{4.11}$$

where θ is the zenith angle, and θ_t is the transmitted angle. $F_{\perp}$, $F_{\parallel}$, and δ can be computed according to:

$$F_{\perp} = |f_{\perp}|^2, F_{\parallel} = \left|f_{\parallel}\right|^2 \tag{4.12}$$

$$\delta = arg\left(f_{\parallel} - f_{\perp}\right) \tag{4.13}$$

Assuming that the complex refractive index $\hat{n}$ of the metallic mirror is known and using the Snell-Descartes law, we can deduce that $F_{\perp}$, $F_{\parallel}$, and δ are related to the zenith angle θ:

$$\theta_t = arcsin(\frac{1}{n}sin(\theta)) \tag{4.14}$$

Finally, the estimation of the zenith angle θ and the azimuth angle ψ are sufficient to solve the problem if the refractive index is known. This estimation can be done by placing the whole setup inside a cylindrical sheet of paper to obtain unpolarized light and to apply the calibration process as described in [139]. This calibration step belongs to techniques commonly used in "Shape From Polarization" where unpolarized light becomes partially linearly polarized depending on the incident zenith angle θ and the azimuth angle ψ. By measuring the first three Stokes parameters of the reflected light, θ and ψ angles can be computed.

As mentioned, from equation (4.8), it is noted that only three out of the four equations are enough to estimate the incident Stokes parameters. Consequently, the polarization state of the incident light can be measured by combining a metallic mirror and one of the following optical setups [22]:

- a Stokes polarizational camera (camera + rotating polarizer + two retarders). This setup is able to measure t_0, t_1, t_2, t_3.

- a simplified polarizational camera (camera + rotating polarizer). This setup is able to measure t_0, t_1, t_2 .
- a simplified polarizational camera + quarter wave-plate. This setup is able to measure t_0, t_1, t_3 .

The use of a simplified polarizational camera, which is able to measure the first three Stokes parameters $t_0, t_1,$ and t_2, is more appropriate as the same setup can be employed in calibration and the polarization state measuring process. Moreover, the whole process can be done in real time by replacing the simplified polarizational camera by a commercial polarizational camera, e.g. FD-1665P Polarization Camera ([1]), which enables the measurement of the first three Stokes parameters at one shot.

Assuming the knowledge of the refractive index $\hat{n}$, the calibration process can be summarized as follows:

1. Compute the zenith angle θ and the azimuth angle ψ by means of "Shape From Polarization" techniques [139].
2. Compute $F_\perp$, $F_\parallel$, and δ as shown in equations (4.12, 4.13).
3. Measure the first three Stokes parameters of the reflected skylight by means of a simplified polarizational camera or a commercial polarization camera (e.g [1]).
4. Compute the incident Stokes parameters by algebraically manipulating equation (4.8).

4.3 Computing the angle and degree of polarization using Stokes parameters

Polarization information are directly computed from three intensity images taken at three different angles (0°, 45°, and 90°) or (0°, 60°, and 120) at one shot using a polarizational camera. The polarization patterns consist of the angle of polarization α and the degree of polarization p which are defined as:

$$\alpha = arctan(\frac{S_2}{S_1})/2 \tag{4.15}$$

,

$$p = \frac{\sqrt{S_1^2 + S_2^2}}{S_0} \tag{4.16}$$

where S_i are the Stokes components ([78]) which can be computed from:

$$I_0 = 0.5(S_0 + S_1 cos\,(2\varphi) + S_2 sin\,(2\varphi)) \tag{4.17}$$

where φ is the polarizer angle. Hence:

$$\begin{aligned} S_0 &= I_0 + I_{90}, \\ S_1 &= I_0 - I_{90}, \\ S_2 &= 2I_{45} - I_0 - I_{90} \end{aligned} \tag{4.18}$$

or

$$\begin{aligned} S_0 &= \frac{2}{3}(I_0 + I_{60} + I_{120}), \\ S_1 &= \frac{2}{3}(2I_0 - I_{60} - I_{120}), \\ S_2 &= \frac{2}{\sqrt{3}}(I_{60} - I_{120}) \end{aligned} \tag{4.19}$$

where I_0, I_{45}, and I_{90} are intensity images taken at (0°, 45°, and 90°) or I_0, I_{60}, and I_{120} are intensity images taken at (0°, 60°, and 120° as an optimum combination ([226])) at one shot using a polarizational camera (e.g FluxData FD-1665 series like FD-1665P-M ([1]) which has three monochrome CCDs with 0°, 45°, and 90° or 0°, 60°, and 120 linear polarizers. See figure (3.1)) .

4.4 Calibration results

An example of incident, reflected, and calibrated angle and degree of polarization using a metallic spherical mirror is given in figures (4.6, 4.7) according to table (4.2).

Location	Le Creusot, France
Latitude +N	46.8
Longitude +E	4.4333
Date	3\7\2012
Time	17:52:59.843 GMT
Altitude	25.4398
Zenith	64.5602
Azimuth East North	187.034
Mirror	Spherical
Refractive index fig (4.1)	$\hat{n} = 1.44 + 5.23i$

Table 4.2: Simulation parameters of figures (4.6, 4.7)

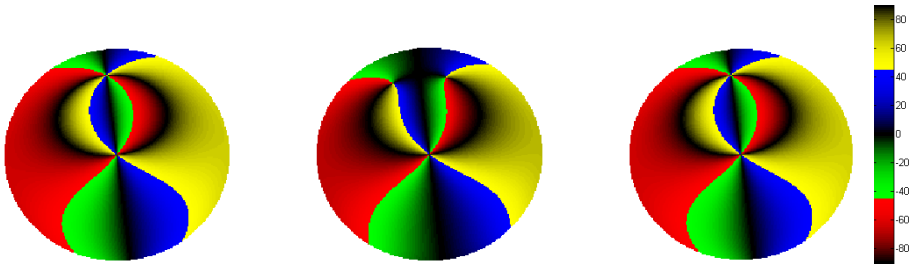

(a) Incident Angle of Polarization α.

(b) Reflected Angle of Polarization α.

(c) Calibrated Angle of Polarization α.

Figure 4.6: Simulation of incident, reflected and calibrated angle of polarization α for a metallic spherical mirror.

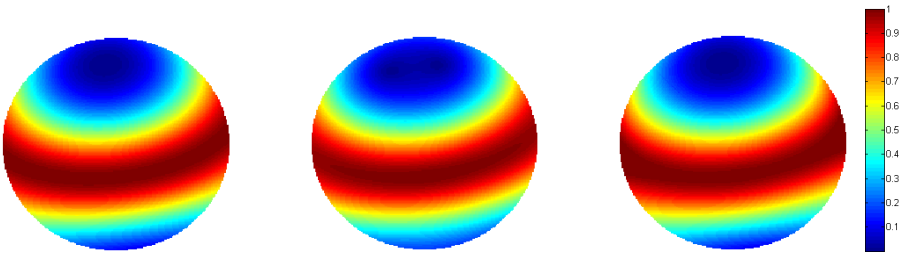

(a) Incident Degree of Polarization p.

(b) Reflected Degree of Polarization p.

(c) Calibrated Degree of Polarization p.

Figure 4.7: Simulation of incident, reflected and calibrated degree of polarization p for a metallic spherical mirror.

A snapshot of the program we developed is shown in figure (4.8) and the metallic spherical mirror simulated is shown in figure (4.9).

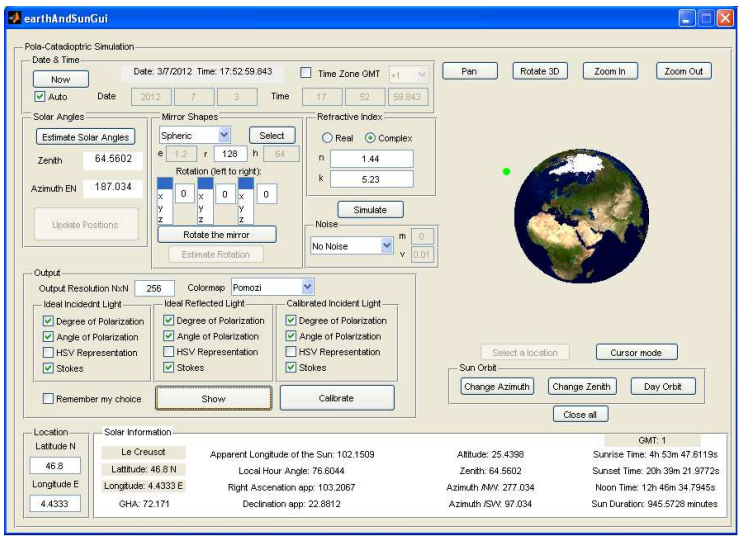

Figure 4.8: A snapshot of our simulation program.

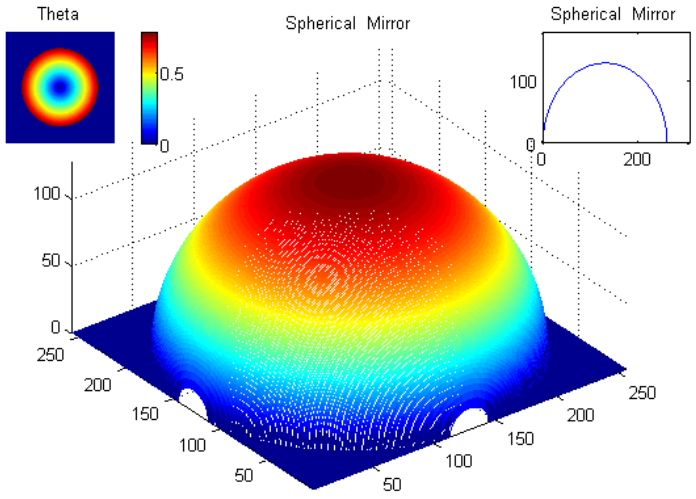

Figure 4.9: Metallic spherical mirror simulation.

In the previous simulation, the incident angle of polarization in figure (4.6-a) is computed as explained in 3.5, the reflected and calibrated angle patterns are computed as explained in 4.3 once the Stokes are obtained as explained in 4.2.2. The incident degree of polarization in figure (4.7) is computed using the Rayleigh model ([160]):

$$\begin{aligned} cos\,(\gamma) &= Sun \cdot Celestial \\ p &= \frac{sin\,(acos\,(cos\,(\gamma)))^2}{(1 + cos\,(\gamma)^2)} \end{aligned} \tag{4.20}$$

The reflected and calibrated degree of polarization patterns are computed as explained in 4.3 once the Stokes are obtained as explained in 4.2.2.

The initial incident Stokes used in simulation are computed using the following formulas:

$$\begin{aligned} S_0 &= I \\ S_1 &= I\,p\,cos\,(2\alpha) \\ S_2 &= I\,p\,sin\,(2\alpha) \end{aligned} \tag{4.21}$$

where I is the intensity which is equivalent to the first Stokes component S_0which is assumed to be uniform.

In practice, the light is reflected on the sensor's mirror and it is captured in three different intensity images which are used to compute the reflected Stokes, angle, and degree of polarization as explained in 4.3. These reflected Stokes are used to calibrate the incident Stokes and hence find the incident angle and degree of polarization patterns as explained in 4.2 and 4.3. More calibration results using different types of mirrors are shown in B.

Chapter 5

Applications

Skylight polarization patterns are used by many insects for navigation. Honeybees use celestial polarization to move between the hive and foraging locations ([167, 238, 42]). Cataglyphis ants ([42]) and nocturnal ([48]) use the sun and moon, respectively, celestial polarization for similar tasks. Salmon fishes may have a similar ability ([88]), which allows them to orient in underwater light fields ([156]). Hence, many researchers, being bio-inspired, have made theoretical and experimental investigations on skylight polarization for autonomous orientation and navigation 5.1.

The patterns of the degree of linear polarization p, and the angle of polarization α of a clear sky were simulated 3.5 and calibrated 4.2 using the proposed omni-pola-catadioptric sky-imaging polarimetry. As expected, p from the clear sky was highest at 90° from the sun and gradually decreased toward the solar and antisolar points. The α pattern had the characteristic pattern explained in sec (1.3), the isolines were always shaped like an eight with a center at the zenith and an axis of mirror symmetry coinciding with the solar-antisolar meridian in such a way that the smaller loop of the eight was always in the solar half of the sky. The solar-antisolar meridian expresses the sun orientation (sun azimuth) with excellent precision. One of this work contributions is that we found out that the eight shape expresses the sun zenith with excellent precision. Solar angles (azimuth and zenith angles) proposed computation algorithms are given in 5.2.

Here we investigate the skylight polarization as a significant global feature to be used for autonomous robots. We focus on Autonomous Vehicle (AV) orientation and attitude estimation. If the AV is capable of computing the solar angles, it will be able to decide its new orientation based on the planned target. AV attitude estimation means to find out the AV orientation. Unmanned surface vehicle (USV) or autonomous surface vehicle (ASV), which refers to any vehicle that operates on the surface of the water, or a Ground Vehicle (GV) can have a simplified model which has only one orientation angle to be estimated which is the yaw angle γ around z-axis. This simple model is considered in 5.3.1. However, if it is assumed to have many changes in the GV angles where it is required to estimate roll, pitch, and yaw angles, then it is possible to apply the method described for any AV in 2 or 5.3.2.

5.1 Robot Orientation and Navigation

Many researchers have made theoretical and experimental investigations on skylight polarization for autonomous orientation and navigation. The sky is polarized due to the scattering of sunlight by particles and air molecules in the atmosphere. The sky polarization patterns present us with the polarization information which can be used as an external compass. The location of the sun mainly determines the celestial skylight polarization pattern. It is visible and stable even in open sky patches when the sun is occluded by clouds, and it also appears beneath dark objects in air that is illuminated by the sun ([160, 211]). The benefit of using the skylight polarization pattern, rather than directly using the sun is that only patches of sky are sufficient for orientation task ([44, 247]).

Firstly, orientation techniques using photodiodes as a primary sensor to read polarization data will be covered 5.1.1. Secondly, as the camera technology became less expensive and more advanced, new techniques using CCD, CMOS, and/or fisheye lens to obtain polarization information will be covered 5.1.2. Thirdly, water and mud detection for off-road navigation will be covered 5.1.3. All methods require a rotating polarizer as a primary optic combined with the mentioned sensors as will be explained.

5.1.1 Sensors using Photodiodes

Inspired by the basic biological neuronal circuit, Lambrinos et al. ([115, 116, 117]) and Möller et al. ([130]), have developed Polarization-Opponent units (POL- OP units) as input devices that are functionally similar to the POL-neurons found in insects. Each POL-OP unit consists of a pair of polarized light sensors (POL-sensors) followed by a log-ratio amplifier. POL-sensors are explained in algorithm (5.1).

Algorithm 5.1 Polarized light sensors (POL-sensors)

POL-sensors

1. The POL-sensors consist of photodiodes with a linear polarizer and a blue transmitting filter on the top.
   (a) In each POL-OP unit the polarizing axis of one POL-sensor was adjusted 90° to the polarizing axis of the other sensor, thus mimicking the crossed-analyzer configuration in the POL-area of insect eyes.
2. The signals of each pair of POL-sensors were fed into a log ratio amplifier.
3. The three pairs of POL-sensors were mounted on a mobile robot and adjusted such that the polarizing axis of the positive channel was 0°, 60° and 120° (similar to the insect layout) with respect to the robot's body axis. The visual fields of the POL-OP units are about 60° and are centered around the zenith.

There are two models to obtain compass direction from the POL-OP responses: a) scanning models and b) simultaneous models. Scanning models (Lambrinos et al. 1997 [115]) are explained in algorithm (5.2).

Algorithm 5.2 Scanning models (Lambrinos et al. 1997 [115])

Scanning models

the agent has to:

1. find the solar meridian to use it as a reference direction 0° for its proprioceptive system.
   (a) For doing that it has to actively scan the sky by rotating around its vertical body axis.
   (b) When the output signal of one POL-OP unit (or a combination of multiple POL-OP units) reaches its maximum, the robot is known to be aligned with the solar meridian.
2. use proprioceptive information to find its heading direction based on the solar meridian.
3. obtain the compass direction by comparing the current output values of the POL-OP units with a lookup table that associates the output values of the POL-OP units with the corresponding orientation of the robot.
4. record the lookup table before each experiment by a single 360° rotation of the robot.

In contrast, the heading direction can be determined continuously and no scanning movements are necessary in a simultaneous model. (Lambrinos et al. 2000 [117]) implemented a simultaneous model which does not require a lookup table, but uses an analytical procedure to derive compass information from the values of the POL-OP units. The change in the polarization pattern during the day has to be taken into account. This can be done by either regularly updating the lookup table or by normalizing the outputs of the POL-OP units as explained in algorithm (5.3).

Algorithm 5.3 Simultaneous models (Lambrinos et al. 2000 [117])

Simultaneous model

normalizing the outputs of the POL-OP units

1. The POL-OP signals are delogarithmized by applying a sigmoid function.
2. Find the two candidate orientations (an ambiguity of π exists) from the equation derived in ([117]) $\phi = \frac{1}{2} arctan \frac{\bar{p}_1(\phi)+2\bar{p}_2(\phi)-\frac{3}{2}}{\sqrt{3}(\bar{p}_1(\phi)-\frac{1}{2})}$ where $\bar{p}_i$ is the delogarithmized sensors output and $i = 1,\ 2,\ \text{or} 3$.
3. Solve the ambiguity by employing a set of ambient-light sensors on the robot.
   (a) The values from eight ambient-light sensors, arranged in two half-circles covering a visual field of 180°, are used to obtain a rough estimate of the robot's heading with respect to the sun (ambient-light sensors with the visual field enclosing the solar meridian will have a stronger response).
4. Transform the current POL-OP readings to signals that are independent of the degree of polarization as shown in ([117]).

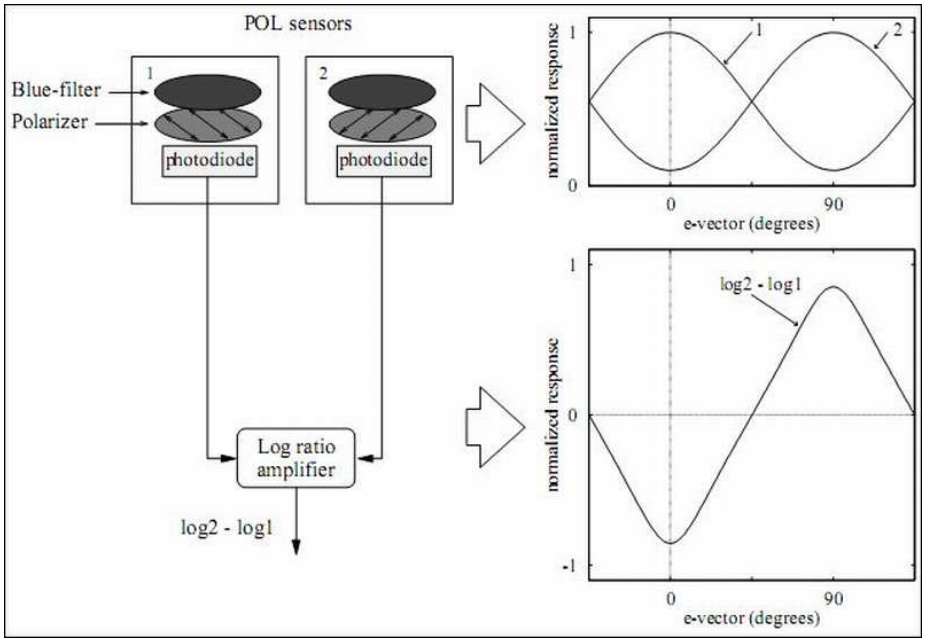

Figure 5.1: Diagrammatic description of POL OP unit. (Adapted from (Lambrinos et al., 2000, Chu et al., 2007))

Chu et al. ([32, 31, 33, 30] and Zhao et al. ([254]), have a bionic navigation sensor which is similar to Lambrinos et al. ([115, 116, 117]) and Möller et al. ([130]) with the same POL-OP unit (see figure (5.1)) and used the same mathematical formulation. Their design is explained in algorithm (5.4).

Algorithm 5.4 Bionic navigation sensor design (Chu et al. [32, 31, 33, 30, 254])

Bionic navigation sensor design

1. Three polarization direction analyzers whose polarizing axis of the positive channel is adjusted to 60° difference from one to one.
   (a) Each one consists of two POL-sensors which have the shape of regular triangular prisms (total of six sensors).
   (b) For each direction analyzer, the polarizing axis of one POL-sensor was adjusted 90° to the polarizing axis of the other sensor.
2. A POL-OP unit consists of a pair of POL-sensors and a log-ratio amplifier.
   (a) The log-ratio amplifier receives input from the two POL-sensors and delivers the difference of their logarithmized signals (exactly the same idea technique of Lambrinos et al. [115, 116, 130, 117]).
3. The three direction analyzers are mounted on a base plate.
4. Six ambient-light sensors are arranged in a ring and mounted in the metal cylinder of the six POL-sensors.
   (a) Each ambient-light sensor consists of standard photoresistors with blue filter in front.

Chu et al. simulated their design in Simulink® and analyzed the output error. Then some outdoor experiments were carried out.

All outdoor experiments performed by Lambrinos et al. ([115, 116, 130, 117]) and Chu et al. ([32, 31, 33, 30, 254]) proved to have high accuracy in obtaining directional information from polarization and the error is independent of the traveling distance.

The performance of the path integration without external reference in ([186]) is compared with the performance using a polarization compass. As proprioceptive estimate, wheel revolutions were used in both cases. The experiments were carried out using a Khepera miniature robot. They found that the e-vector (the observed regular pattern across the entire celestial hemisphere formed by the directions of polarization) compass was much better in accuracy.

Two biomimetic sensors were developed by ([26]) and made flight tests for stabilization and navigation of an aircraft using the spatial, polarizational, and spectral distributions of light in the environment. They tried to mimic the head

of a dragonfly called Hemianax Papuensis. Here we consider the polarization sensor only which is explained in algorithm (5.5).

Algorithm 5.5 Mimicking polarization vision in the head of a dragonfly called Hemianax Papuensis (Chahl & Mizutani, 2010 [26])

Polarization sensor

in the mimicked head of a dragonfly called Hemianax Papuensis

1. It used three photodiodes each with their own optics and polarization filters.
   (a) The output of the photodiode amplifiers were digitized and processed on a microcontroller.
   (b) Each photodiode had a voltage bias and gain that required calibration.
2. The direction was computed using three samples from an assembly of diode, filter, and amplifier at known angles (0°, 60° and 120°) relative to the orientation of the polarization axis of the polarization filter.

Each photodetector response to incident light in terms of voltage v is $v = b + P.F + q$, which includes the response to unpolarized light q and a bias term b which is due to the electronics. The sensor response to the polarized component of the light is given by the dot product $P.F$ where F is a column vector representing the orientation of the polarization axis of the filter and P is a row vector representing the direction and magnitude of the incident polarized light. To eliminate electronic and optical biases (b and q) the difference between the responses of the three samples v_1 to v_3 was taken. Solving for P gives: $P^T = \begin{bmatrix} v_1 - v_2 \\ v_1 - v_3 \end{bmatrix} \begin{bmatrix} F_1 - F_2 & F_1 - F_3 \end{bmatrix}^{-1}$where $F_1 - F_2$ is a column vector.

This solution assumes a calibrated system. To test their sensor, a remotely piloted aircraft was instrumented with a calibrated polarimeter and attitude reference that included a magnetic compass. The flight was run early in the morning when the sun was low. The polarization compass produced a discontinuity several times during the flight as the solution passed through 180°. There were minor differences between the two measures. They conclude that the absence of any correction for attitude probably contributed to most deviation between the magnetic and north-aligned polarization heading.

5.1.2 CCD, Fisheye and CMOS Sensors

Usher et al. ([228]) proposed to perceive sky polarization pattern using a color CCD video camera and a linear polarizing film as a filter. The blue component was used for analysis as the sunlight polarization is most apparent at UV and blue wavelengths ($350 - 450\,nm$). They smoothed all images by a 2D Gaussian

function to overcome the poor response at these short wavelengths. Two images were taken at a time, with the second image having its polarizing filter axis orthogonal to the first. Taking a set of images, they modeled the response as $f(\Phi) = K * [1 + d * cos(2\Phi)]$ where K is a scaling factor dependent on camera shutter settings and ambient conditions, d is degree of polarization, Φ is the orientation of the polarizing filter with respect to the solar meridian (line connecting the zenith and the sun), and $f(\Phi)$ is the mean intensity of an image. Their model had the same form for the photosensitive diodes of ([117]). Their initial experiments proved that it is possible to locate the solar meridian using a digital camera applying the scanning method of ([115]) and hence extracting a reference bearing from an arbitrary orientation.

The mentioned methods are simulating insect strategy taking advantage of the skylight polarization through single numerical values rather than patterns. Wu et al. ([247]) presented a method to get navigation orientations by gradient vectors of skylight polarization maps even if the sun is invisible or occluded by clouds. The maps were provided by a zenith centered imaging polarimeter with narrow field of view. The imaging polarimeter was constructed by a sensitive industrial CCD camera with short focus lens and a linearly polarizing filter. Assisted by a compass and gradienter, the imaging polarimeter was kept horizontal with the local sea level so its field of view center was adjusted to the zenith of the sky area during the experiments. Then the linear polarizer mounted in front of the objective lens was rotated. For a certain sky area, four images were taken by rotating the linear polarizer to four different relative positions (0°, 45°, 90°, and 135°) following the method in ([119]). They estimated the solar azimuth by searching the maximum attenuation gradient vector among different azimuth relative to zenith in the degree of polarization p map, or the symmetrical axis in the angle of polarization α map making use of the attenuation from zenith to horizon along the local meridian in the p maps and the symmetrical distribution of α along the local meridian. They concluded that the skylight polarization maps are able to supply stable solar azimuths information and if aided by calendar (insect circadian clock), the real body orientation could be located.

Sarkar et al.([174, 177, 175, 176]) proposed a polarization analyzing CMOS image sensor. It is able to sense polarization information in real time using a metallic wire grid micro-polarizer oriented in various directions on top of the pixel. The p and α patterns can be computed using three intensity images (0°, 45°, and 90°) using the Stokes parameters as in ([125, 70, 49]), the variations of which can be used as compass clues. The image sensor consists of an array of 128×128 pixels, occupies an area of $5 \times 4\,mm^2$ and it has been designed and fabricated in a $180\,nm$ CMOS process. They concluded to use the computed polarization information as a clue for autonomous robot navigation.

Unlike previous investigations, Miyazaki et al. ([129]) analyzed sky polarization patterns with the fisheye lens. They have tilted the measurement system based on a fisheye lens, a CCD camera, and a linear polarizer, in order to analyze transition of the 180° sky polarization patterns while tilting. The used technique is similar to the technique described in ([160, 92]). Three photographs were taken for three different alignments (0°, 45°, and 90°) of the transmission axis of the polarizer clockwise from the top view of the camera. Their main contribution was to analyze the sky polarization patterns when the camera was tilted from the horizon. They presented a method to determine the solar merid-

ian orientation from photos taken outdoors, while only a small part of the sky was available and the camera sensor was not horizontal. Therefore, the orientation of the camera could be determined from the solar meridian.

5.1.3 Water and mud detection for off-road navigation

Water and mud detection based on polarization depends on the physical principle that the light reflected from water surface is partially linearly polarized and the polarization phases of them are more similar than those from the scenes around. These hazards can be detected by comparison of polarization degree and similarity of the polarization phases. There is a comparison between different approaches of water and mud hazards detection in ([126, 166]) and a survey in ([108]).

Icy or wet roads present dangerous situations as there is an increased danger of losing control of the vehicle and the glare from wet roadway may hide path markings and other road features. A polarizing filter can considerably reduce reflections due to the fact that water tends to horizontally polarize reflected light. Huber et al. ([106]) have developed a spectro-polarizational imager. It is a portable machine vision system that operates at video frame rates. It contains only electronically controllable components, including an imaging acousto-optic tunable filter, a phase retarder, and a standard CCD-based camera. The system operates much like an ordinary CCD camera, except that the spectral and polarizational content of light to be viewed is electronically controlled using computer. During operation, the host computer sends commands to the controller to select the desired spectral and polarization parameters. They proposed glare reduction and glare detection in which their imaging system could be applied to wet or icy road conditions. Glare reduction works similarly to a polarizing filter inserted in the optical path. However, the phase retarder accomplishes this electronically and can be programmatically enabled and disabled, which is beneficial since an additional filter reduces the overall intensity of the image. For glare detection, they identify horizontally polarized reflections, thereby detecting possible dangerous road conditions. In a computer-assisted driving scenario, this additional information could be used to alert the driver of the danger, or in an autonomous vehicle, the controller could modify its driving habits accordingly.

Yamada et al. ([249]) discriminated the wet road using the ratio between horizontal and vertical polarization image intensity for each pixel. This algorithm obtained good discrimination accuracy when applied to highway environment where most water reflects the sky. A drawback of this polarization ratio based method is that it becomes imprecise when water reflects other aspects of the environment, which is common in off-road navigation.

Sarwal et al. ([178]) have made use of two approaches for small water bodies' detection. The first one requires use of an existing custom camera with three polarization filters (0°, 45°, and 90°); intrinsically mounted such that these filters and connected optics view exactly the same scene. The other approach requires use of three physically distinct cameras with the same type of polarization filters mounted on three low-cost cameras each with similar optics, running with certain geometric approximations due to the flat-earth assumption. There are pros and cons for each approach. Both approaches used the formulas from ([243]).

In order to detect water hazards for autonomous off-road navigation, especially bodies of water which roofed with tree canopy, Xie et al. ([248]) presented another polarization method based on the similarity between polarization patterns reflected from water surface than those from other scenes. Their detection algorithm is based on the comparison of p and similarity of α using the formulas from ([243]).

Polarization imaging and stereo vision was used by ([157]) to detect water hazards for robot navigation. He investigated the conventional single camera polarization imaging setup employing a mechanically rotated polarizer, polarization contrast imaging using two cameras, a three camera setup enabling the complete characterization of partially linearly polarized light, and a four camera setup employing two polarizers with identical orientations. The main challenge in their proposed system was to improve the pixel correspondence across the polarization images. They obtained good results for water detection, however further in-depth experiments are still required.

Robust mud detection is also a critical perception requirement for autonomous navigation. Mud is highly polarized and hence polarization based techniques can be used. The use of multiple sensors for mud detection including a polarization camera was proposed by ([166]). At a pixel level, partial linear polarization is measured by the transmitted radiance through a polarization filter. To determine the polarization state, three images of a scene are acquired, each with the polarization filter at a different orientation. To calculate "polarization contrast" as a simplified measurement, only two images are required where the polarization filter orientations differ by 90°. The "polarization contrast" at each pixel can be calculated by dividing the absolute value of the difference between the 0° and 90° intensity values by the sum of them. Regions that have a significantly higher degree of polarization p can be a potential cue for water or mud. In the experiments of ([166]), two polarization sensors were used: SAMBA and SALSA polarization cameras produced by Bossa Nova Technologies. The SAMBA camera provides a "polarization contrast" image and the SALSA camera provides degree of polarization p, intensity I, and angle of polarization α images.

5.2 Solar angles estimation

All solar algorithms used to obtain the skylight polarization patterns at a given time and location are based on ([127, 4]).

5.2.1 Azimuthal angle estimation

The slope of the solar-antisolar meridian is directly related to the solar azimuthal angle ψ_s. Algorithm (5.6) which is visually explained in figure (5.2) finds ψ_s from east to north by fitting a line to the solar-antisolar meridian. Figure (4.8) shows a snapshot of the program, figure (B.20) shows some examples of solar angles estimation within the day, and table (5.1) gives the simulation parameters and the computation results.

Generally the error of algorithm (5.6) was found to be within ± 0.2 (the max error was ± 0.2 with 128×128 resolution, it was ± 0.03 with 256×256 resolution).

Latitude +N	66
Longitude +E	18
Date	5\7\2012
Time Zone	GMT +1
Sunrise	0h 39m 24.182s
Noon	11h 52m 37.6889s
Sunset	23h 5m 51.1957s
Sun duration	1346.4502 minutes
Mirror	Spherical
Refractive index fig (4.1)	$\hat{n} = 1.44 + 5.23i$

(a) Main parameters

	Ground Truth	**Azimuth estimation**		**Ground Truth**	**Zenith estimation**	
Time	**Azimuth EN**	**Line fit** (5.6)	**Error**	**Zenith**	Computed by (5.7, 5.8)	**Error**
Sunrise (0:37)	**-79.7608**	-79.7653	**0.0045**	**90.8311**	90.8311	**0**
Morning (6:00)	**-8.0277**	-8.0453	**0.0176**	**68.5722**	68.5722	**0**
Noon (11:53)	**90.1251**	90.3499	**-0.2248**	**43.2796**	43.2796	**0**
Afternoon (18:00)	**191.2770**	191.3160	**-0.0390**	**70.0941**	70.0941	**0**
Sunset (23:04)	**258.7750**	258.7450	**0.0300**	**90.8421**	90.8421	**0**
		Max Error	±0.2	Max Error		**0**

(b) Solar angles computations.

Table 5.1: Simulation parameters and solar angles computation figure (B.20)

Figures (5.3a, 5.3b) show examples of Azimuthal angle estimation after adding noise. Section (B.3) shows more examples on solar angles estimation.

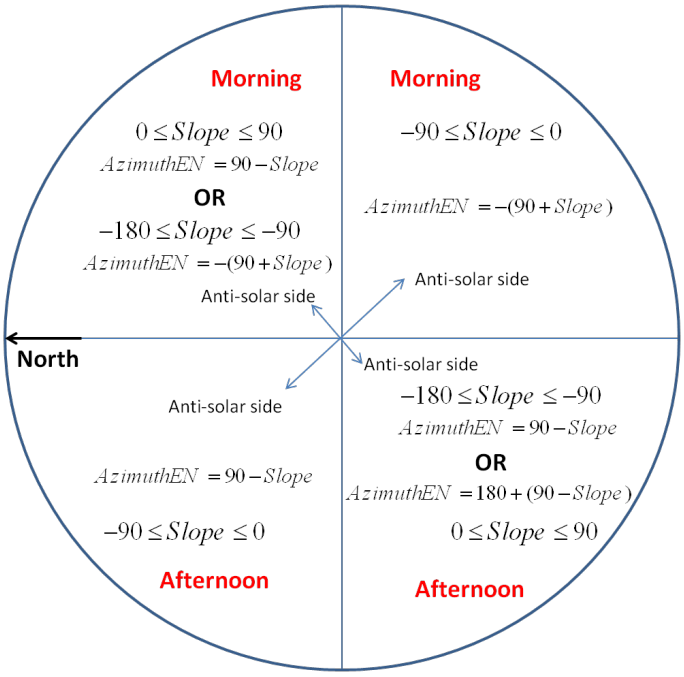

Figure 5.2: Azimuth estimation.

5.2.2 Zenital angle estimation

The contours of theα pattern at $\pm 45°$are directly related to the solar zenital angle θ_s. Algorithm (5.7) finds θ_s. Figure (B.20) shows some examples. It is assumed that the mirror shape and refractive index are known. If the minimization step in algorithm (5.7) fails (the solver fails) to find the correct zenith, then it is repeated with a new start point within the given bounds (it can be improved by a smart start point based on the time of the day), until it converges to a correct solution (the error is very close to zero). In all experiments, the start point is 0, the lower bound is 0, and the upper bound is 90 to92 (when the sun altitude is negative the zenith is more than 90).

Algorithm 5.7 Solar zenital angle estimation.

1. Find azimuth as explained in algorithm (5.6).
2. Find the contours of $\pm 45°$in the *captured* α pattern.
3. $\underset{\theta_s}{arg\,min}\,(\alpha - captured)$, where α is as defined in equation (3.1).

Algorithm 5.6 Solar azimuthal angle estimation.

1. Extract solar-antisolar meridian points where the angle of polarization α is very close to zero.
2. IF the points are highly correlated
   (a) Fit a line to these points.
3. ELSE using one of the RANdom SAmple Consensus (RANSAC) algorithm family ([2])
   (a) Remove outliers
   (b) Fit a line to the inliers
4. Find the antisolar side of the line where the corresponding degree of polarization p is higher than the solar side.
5. Find the slope of this line.
6. Compute the Azimuth from East to North as follows:
7. IF $Morning$
   (a) IF $Slope < 0°$
      i. $Azimuth = -(90° + Slope)$
   (b) ELSEIF $Slope > 0°$
      i. $Azimuth = 90° - Slope$
   (c) ELSE $Slope = 0°$
   $Azimuth = 0°$
8. ELSE $Noon \,\&\, Afternoon$
   (a) IF$Slope < 0°$
      i. IF $Slope = -180$
         A. $Azimuth = 90°$
      ii. ELSE
         A. $Azimuth = 90° - Slope$
   (b) ELSEIF $Slope > 0°$
      i. $Azimuth = 180 + (90° - Slope)$
   (c) ELSE $Slope = 0°$
      i. $Azimuth = 180°$

If the incident α pattern is very noisy then using the complete pattern for zenith estimation is more robust and reliable. Only angle of polarization α values corresponding to some degree of polarization p values greater than a given threshold (e.g $p > 0.4$) are considered when the complete pattern is used. Algorithm (5.8) explains how to compute the zenital angle from the complete α pattern.

Algorithm 5.8 Solar zenital angle estimation.

1. Find azimuth as explained in algorithm (5.6).
2. $\underset{\theta_s}{arg\,min}\,(\alpha - captured)$, where α is as defined in equation (3.1).

Without adding noise, the error for zenith estimation in algorithms (5.7, 5.8) was found to be *zero* where up to 4 solvers were required and each solver requires up to 30 iterations (10 iterations in average). If the start point or the search bounds are smartly provided based on the time of day then only *one* solver with an average of 4 iterations (up to 10 iterations) is required.

Figures (5.3a, 5.3b) show examples of zenital angle estimation after adding noise. Section (B.3) shows more examples on solar angles estimation.

5.2.3 Adding noise

Two types of noise are used to evaluate our results; Gaussian and Speckle noise as follows [79]:

- $NI = I + \sqrt{v} * randn(size(I)) + m$ adds Gaussian white noise of mean m and variance v to the image I where NI is the noisy image and $randn(size(I))$ generates normally distributed pseudorandom numbers of the same size as I.
- $NI = I + sqrt(12 * v) * I. * (rand(size(I)) - .5)$ adds Speckle noise (multiplicative noise) to the image I, where $rand(size(I)) - .5$ is uniformly distributed pseudorandom numbers with mean 0 and variance$v$.

Examples of adding noise to the skylight polarization patterns are shown in B.2.

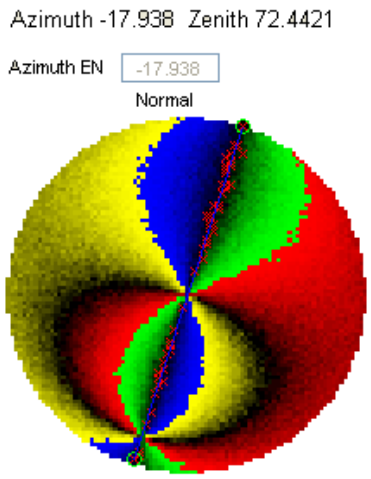

(a) Solar angles estimation from a noisy (Gaussian noise of variance 4 and mean 2) α pattern at 05:20. The correlation between the extracted points was greater than a given threshold (e.g 0.85) and hence a line was fitted to estimate the azimuthal angle. The zenital angle is estimated from the extracted $\pm 45°$contours. The ground truth values are: $azimuth = -16.8579$ and $zenith = 72.537$. Simulation parameters are shwon in table (5.1a).

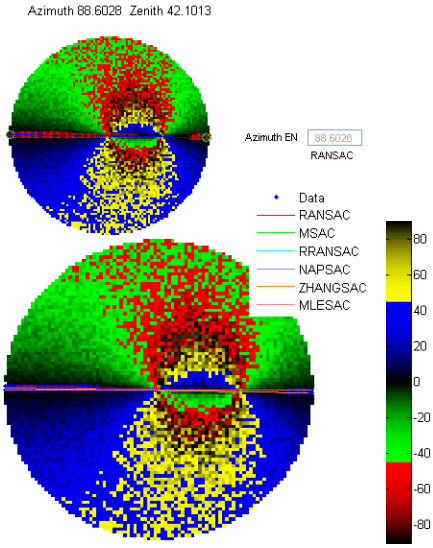

(b) Solar angles estimation from a noisy (Speckle noise of variance 0.04 and mean 0) α pattern at 11:50. Due to high noise many outliers exist and the correlation between the extracted points was less than or equal a given threshold (e.g 0.85), hence different RANSAC methods were applied and the one with the highest number of inliers was selected. A line is fitted to these points in order to estimate the azimuthal angle. The zenital angle is estimated from the extracted $\pm 45°$contours. The ground truth values are: $azimuth = 89.1161$ and $zenith = 43.2814$. Simulation parameters are shown in table (5.1a).

Figure 5.3: Solar angles estimation from a noisy α pattern.

The error in estimating the solar angles in extremely noisy conditions is shown in tables (5.2, 5.3, 5.4, 5.5). All experiments were performed on low resolution 128×128 pixels. The results show that the proposed algorithms are robust against high levels of noise.

			Azimuth estimation
			5.6
		Speckle noise with mean m and variance v	
		Ground Truth GT	**Error**
Time		**Azimuth EN**	Using all points
Morning (6:00)	**Noise Variance**	**GT -8.0277**	Speckle $m = 0$
	$v = 0.1$	-8.0634	0.0357
	$v = 0.15$	-8.0712	0.0435
	$v = 0.20$	-8.0331	0.0054
	$v = 0.25$	-8.0671	0.0394
	$v = 0.3$	-8.0638	0.0361
Afternoon (18:00)		**GT 191.2770**	
	$v = 0.1$	191.3375	-0.0605
	$v = 0.15$	191.3522	-0.0752
	$v = 0.20$	191.3121	-0.0351
	$v = 0.25$	191.3174	-0.0404
	$v = 0.3$	191.3234	-0.0464

Table 5.2: Azimuth estimation after adding speckle noise with $v < 0.3$

The azimuthal estimation error using algorithm (5.6) was between $\pm 0.03^\circ$ and $\pm 0.07^\circ$ after adding speckle noise with zero mean and variance up to 0.3. Increasing the amount of noise resulted in adding many outliers and hence using the extracted points failed to find the azimuthal angle. After removing outliers, the error was between $\pm 0.2^\circ$ and $\pm 0.4^\circ$ with the speckle noise variance between 0.35 and 1. Generally, adding speckle noise with zero mean and variance 0.04 is considered very high and the experiments are done for levels of speckle noise with variance higher than 0.04.

The azimuthal estimation error was less than $\pm 0.2^\circ$ after adding Gaussian noise with zero mean and variance up to 2. Increasing the amount of Gaussian noise the error became between $\pm 0.3^\circ$ and $\pm 0.5^\circ$ with zero mean and variance up to 5. Increasing the amount of noise the error became between $\pm 0.35^\circ$ and $\pm 0.9^\circ$ with zero mean and variance up to 18. The azimuthal estimation error was between $\pm 1^\circ$ and $\pm 2.5^\circ$ after adding Gaussian noise with $mean = 5$ and variance up to 18.

The zenital estimation error using the $\pm 45^\circ$ contours as explained in algorithm (5.7) was within $\pm 2.3^\circ$ after adding speckle noise with zero mean and variance up to 0.025. Increasing the amount of speckle noise, the error was within $\pm 3.3^\circ$ with zero mean and variance up to 0.110. Adding speckle noise with zero mean and variance more than 0.110 the algorithm fails to find an estimation within acceptable range where the error was more than 8°. Generally, adding speckle noise with zero mean and variance 0.04 is considered very high and the experiments are done for levels of speckle noise with variance higher than 0.04.

The zenital estimation error using the complete pattern as explained in algorithm (5.8) was within $\pm 2^\circ$ after adding speckle noise with zero mean and variance up to 0.02. Increasing the amount of speckle noise, the error was within $\pm 7.5^\circ$ with zero mean and variance up to 0.03. With zero mean and

variance more than 0.03 it fails to find an estimation within acceptable range where the error was more than 8°.

The zenital estimation error using the ±45° contours as explained in algorithm (5.7) was within ±0.3° after adding Gaussian noise with zero mean and variance up to 6. Increasing the amount of Gaussian noise, the error was within ±0.8° with zero mean and variance up to 18.

The zenital estimation error using the complete pattern as explained in algorithm (5.8) was within ±0.5° after adding Gaussian noise with zero mean and variance up to 6. Increasing the amount of Gaussian noise, the error was within ±2° with zero mean and variance up to 18.

Some examples of noisy α patterns and the estimated solar angles in different times of the day are shown in figures (B.21, B.22, B.23).

5.3 AV attitude estimation

The algorithms discussed here are generally based on the contours of theα pattern at ±45° or the complete α pattern. Whenever the complete α pattern is used only α values corresponding to some degree of polarization p values greater than a given threshold (e.g $p > 0.4$) are considered.

5.3.1 USV/GV attitude estimation

USV/GV is assumed to move on a flat surface and hence the vehicle can have a simplified model which has only one rotation angle to be estimated which is the yaw angle around z-axis γ. We propose three different algorithms:

Algorithm 5.9 Estimating the GV orientation from the solar azimuthal angle.

1. Given date, time and location, calculate the solar azimuth.
2. Estimate the azimuth from the *captured* α pattern as in algorithm (5.6).
3. The orientation of the vehicle is the difference between the theoretical azimuth and the computed azimuth (rotating around the z-axis is equivalent to rotating the solar anti-solar meridian line).

Algorithm 5.10 Estimating the GV orientation from the α pattern.

1. Given date, time and location, calculate the solar azimuth and zenith. The mirror shape and refractive index are assumed to be known.
2. $\underset{\gamma}{arg\,min}\,(R_z\alpha - captured)$, where α is as defined in equation (3.1), $R_z\alpha$ is the theoretically rotated α around the z-axis, and γ is the angle of rotation to be estimated around z-axis.

			Azimuth estimation		
			5.6		
		Noise with mean m and variance v			
		Ground Truth GT	**Error**		
Time		**Azimuth EN**	Using all points	Removing outliers	
Morning (6:00)	**Noise Variance**	**GT -8.0277**	Speckle $m = 0$	**GT -8.0277**	Speckle $m = 0$
	$v = 0.35$	Fails		-8.2971	0.2694
	$v = 0.7$	Fails		-8.4270	0.3993
	$v = 1$	Fails		-8.1301	0.1024
			Gaussian $m = 0$		Gaussian $m = 0$
	$v = 6$	-8.6690	0.6413	-8.427	0.3993
	$v = 18$	-9.5422	1.5145	-8.8807	0.8530
			Gaussian $m = 5$		Gaussian $m = 5$
	$v = 6$	-10.4701	2.4424	-9.7276	1.6999
	$v = 18$	-11.1778	3.1501	-10.5208	2.4931
Afternoon (18:00)		**GT 191.2770**	Speckle $m = 0$	**GT 191.2770**	Speckle $m = 0$
	$v = 0.35$	Fails		191.3099	-0.0329
	$v = 0.7$	Fails		192.0948	-0.8178
	$v = 1$	Fails		190.5392	0.7378
			Gaussian $m = 0$		Gaussian $m = 0$
	$v = 6$	191.8729	-0.5959	191.6593	-0.3823
	$v = 18$	191.7871	-0.5101	191.6894	-0.4124
			Gaussian $m = 5$		Gaussian $m = 5$
	$v = 6$	189.271	2.006	189.4623	1.8147
	$v = 18$	191.1113	0.1657	189.3350	1.9420

Table 5.3: Azimuth estimation after adding noise.

		±45			Complete		
		5.7			5.8		
		Noise with mean m and variance v					
Time		**Zenith**	Error	Solvers	**Zenith**	Error	Solvers
Morning (6:00)	**Noise Variance**	**GT 68.5722**	Speckle $m = 0$		Speckle $m = 0$		
	$v = 0.01$	68.8988	-0.3266	10	68.3957	0.1765	10
	$v = 0.015$	70.9352	-2.3630	15	67.9496	0.6226	10
	$v = 0.020$	67.1862	1.3860	15	66.6074	1.9648	15
	$v = 0.025$	66.3604	2.2118	15	71.9893	-3.4171	35
Afternoon (18:00)		**Ground Truth GT 70.0941**					
	$v = 0.01$	69.0080	1.0861	10	68.9085	1.1856	10
	$v = 0.015$	68.7991	1.295	10	66.6739	3.4202	15
	$v = 0.020$	69.5026	0.5915	15	68.7879	1.3062	15
	$v = 0.025$	68.3048	1.7893	15	62.8241	7.27	15

Table 5.4: Zenith estimation after adding speckle noise with $v < 0.3$

			±45		Complete		
			5.7		5.8		
		Noise with mean m and variance v					
Time		**Zenith**	Error	Solvers	**Zenith**	Error	Solvers
Morning (6:00)	**Noise Variance**	**GT 68.5722**	Speckle $m = 0$		Speckle $m = 0$		
Fails when	$v = 0.03$	68.5039	0.0683	15	62.8087	5.7634	15
$v > 0.11$	$v = 0.07$	67.4672	1.1050	15	Fails		
$Error > 8^\circ$	$v = 0.11$	70.0979	-1.5257	15	Fails		
			Gaussian $m = 0$		Gaussian $m = 0$		
	$v = 6$	68.3747	0.1975	5	67.2104	1.3618	3
	$v = 18$	67.8074	0.7648	5	69.6249	-1.0527	4
			Gaussian $m = 5$		Gaussian $m = 5$		
	$v = 6$	68.1555	0.4166	10	68.9444	-0.3722	10
	$v = 18$	68.2763	0.2959	10	67.9979	0.5743	10
Afternoon (18:00)		**70.0941**	Speckle $m = 0$		Speckle $m = 0$		
Fails when	$v = 0.03$	67.7626	2.3315	15	62.9011	7.193	15
$v > 0.11$	$v = 0.07$	66.7294	3.3647	25	Fails		
$Error > 8^\circ$	$v = 0.11$	69.4189	0.6752	25	Fails		
			Gaussian $m = 0$		Gaussian $m = 0$		
	$v = 6$	69.8737	0.2204	10	69.9738	0.1203	10
	$v = 18$	69.9778	0.1163	10	71.1411	-1.047	10
			Gaussian $m = 5$		Gaussian $m = 5$		
	$v = 6$	69.1769	0.9172	10	68.1117	1.9824	10
	$v = 18$	68.5510	1.5431	10	70.6462	-0.5521	10

Table 5.5: Zenith estimation after adding speckle and Gaussian noise

Algorithm 5.11 Estimating the GV orientation from the α pattern.

1. Given date, time and location, calculate the solar azimuth and zenith. The mirror shape and refractive index are assumed to be known.
2. Find the contours of $\pm 45°$in the *captured* α pattern.
3. $\underset{\gamma}{arg\,min}\,(R_z\alpha - captured)$, where α is as defined in equation (3.1), and $R_z\alpha$ is the theoretically rotated α around the z-axis and γ is the angle of rotation to be estimated around z-axis.

If the minimization step in algorithms (5.10, 5.11) fails, then it is repeated with a new starting point within reasonable range (our experiments were in the range $-45 \leq \gamma \leq 45$), until it converges to a correct solution (the error is very close to zero). Algorithm (5.11) is more robust than algorithm (5.10) as it is mush faster and does not require the Jacobin matrix in the optimization step.

Figure (5.4) shows some examples applying algorithms (5.10, 5.11) for negative and positive rotations around the z-axis and estimation results.

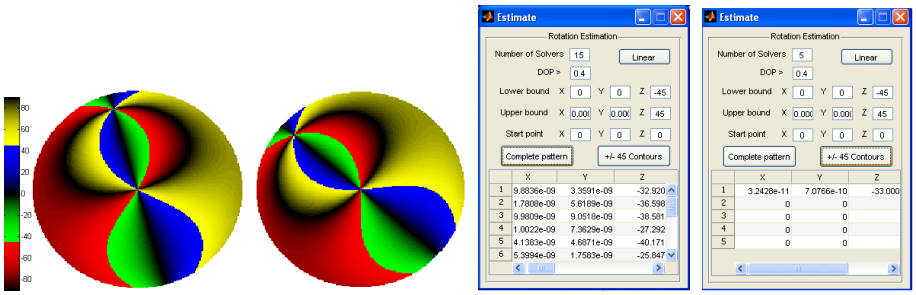

(a) Original α pattern before rotation. (b) α pattern rotated by $-33°$around the z-axis. (c) γ estimation using algorithm (5.10) (d) γ estimation using algorithm (5.11)

Figure 5.4: γ estimation using algorithms (5.10, 5.11).

5.3.2 AV attitude estimation from α pattern

Algorithm (5.12) described here can be used for any AV which is modeled with a general rotation around x, y, and z axises. We consider applying it to UAV vehicles.

Algorithm 5.12 Estimating the AV orientation from the α pattern.

1. Given date, time and location, estimate the solar azimuth and zenith. The mirror shape and refractive index are assumed to be known.
2. $\underset{\phi,\beta,\gamma}{arg\,min}\,(R\alpha - captured)$, where α is as defined in equation (3.1), and $R\alpha$ is the theoretically rotated α around x-axis (roll ϕ), y-axis (pitch β), and z-axis (yaw γ) respectively, and ϕ, β, γ are the angles of rotation to be estimated.

Algorithm 5.13 Estimating the AV orientation from the α pattern.

1. Given date, time and location, estimate the solar azimuth and zenith. The mirror shape and refractive index are assumed to be known.
2. Find the contours of $\pm 45°$in the *captured* α pattern.
3. $\underset{\phi,\beta,\gamma}{arg\,min}\,(R\alpha - captured)$, where α is as defined in equation (3.1), and $R\alpha$ is the theoretically rotated α around x-axis (roll ϕ), y-axis (pitch β), and z-axis (yaw γ) respectively, and ϕ, β, γ are the angles of rotation to be estimated.

If the minimization step in algorithms (5.12, 5.13) fails, then it is repeated with a new starting point within reasonable range (e.g $-45 \leq \phi, \beta, \gamma \leq 45$), until it converges to a correct solution (where the error is very close to zero). There are many combinations of rotation angles to obtain the same final AV attitude if the general rotation is considered where roll ϕ, pitch β, and yaw γ angles have to be computed and no knowledge is assumed. Otherwise, an exact solution is obtained if one or two different rotations occurred assuming that we know the rotation axis.

Algorithm (5.13) is more robust than algorithm (5.12) as it is mush faster and does not require the Jacobin matrix in the optimization step. Both algorithms converge to the exact solution if rotation occurs around one or two axises and the axises of rotation are assumed to be known however the order of rotation is unknown, see figures (5.5a, 5.5b). If the rotation occurs around the three-axises then the algorithms always converge to a correct solution, see figures (5.6, 5.7). Figures (5.5a, 5.5b, 5.6, 5.7) are based on algorithm (5.13).

If a better range is defined for upper and lower bounds on the amount of rotation (see figure (5.8a)) or a good starting point is provided, which is possible in practice, then the possibility to converge to the exact solution is higher using algorithm (5.13). If there is only one or two rotations but the axises of rotations are unknown and the number of axises are unknown then algorithm (5.13) can be applied to estimate an equivalent rotation (roll ϕ, pitch β, and yaw γ). Figure (5.8b) shows an example of estimating an equivalent rotation to a rotation about one unknown axis and figure (5.8c) shows an example of estimating an equivalent rotation to two rotations about two unknown axises.

In figures (5.6, 5.7, 5.8b, 5.8c) it is noted that the original rotated pattern and the estimated one are visually identical except for the earth (the dark

green area). That is because another rotation equivalent to the original one is estimated with a new pose of the camera where part of the earth appears due to a higher rotation around x or y axises. This can be avoided if an initial guess about the axis of rotation is provided or conditioned based on the real circumstances.

Latitude +N	46.8
Longitude +E	4.433
Date	(24 and 26)\7\2012
Time Zone	GMT +1
Mirror	Spherical
Refractive index	$\hat{n} = 1.44 + 5.23i$

Table 5.6: Simulation parameters

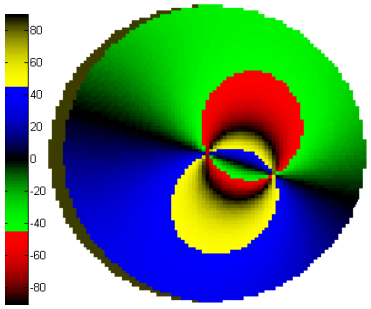

Correctly estimated solution			
x	**y**	**z**	**Order**
10	0	20	1

(a) Estimating two angles of rotation assuming the knowledge of the rotation axis. The robot is rotated around x by 10°then around z by 20°. Note that the rotation order is not assumed to be known. The earth is represented in dark green. The simulation parameters are shown in table (5.6). Simulated pattern in Le Creusot on 24/07/2012 at 12:39:5

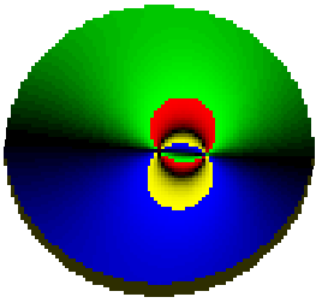

Correctly estimated solution			
x	**y**	**z**	**Order**
0	10	20	1

(b) Estimating two angles of rotation assuming the knowledge of the rotation axis. The robot is rotated around y by 10°then around z by 20°. Note that the rotation order is not assumed to be known. The earth is represented in dark green. The simulation parameters are shown in table (5.6). Simulated pattern in Le Creusot on 24/07/2012 at 12:39:5

Figure 5.5: Estimating angles of rotation assuming the knowledge of the rotation axis.

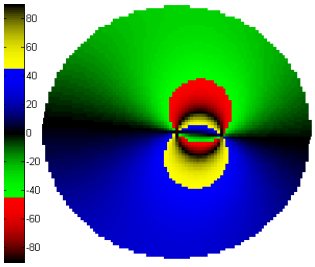

(a) Original α pattern

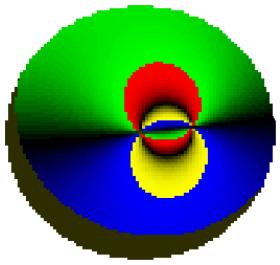

(b) α pattern rotated by 10°around x, 20°around y, and 30°around z.

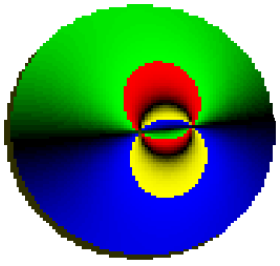

(c) First estimated rotation.

Correctly estimated solutions			
x	**y**	**z**	**Order**
4.7941	4.1273	-4.2800	1
4.9230	0.9909	-10.3987	2
6.3039	12.9598	13.5135	3
4.9917	7.1731	1.6941	4

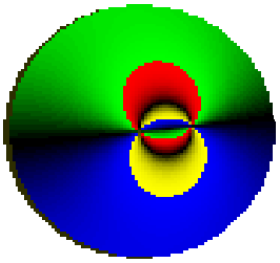

(d) Second estimated solution.

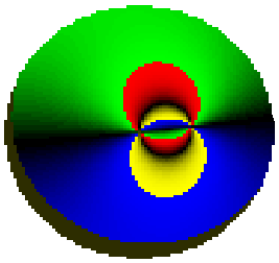

(e) Third estimated rotation.

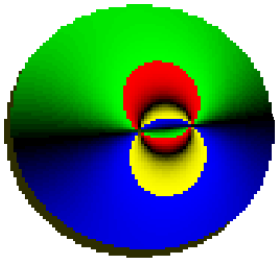

(f) Fourth estimated solution.

Figure 5.6: Estimating three angles of rotation where no knowledge is assumed. The simulation parameters are the same like figures (5.5a, 5.5b) where the original α pattern is rotated by 10°around x, 20°around y, and 30°around z respectively. The estimated solutions are shown in the second, third and fourth row. Note that the rotation order is not assumed to be known. The start point is (0°,0°,0°), the lower bound is (−45°,−45°,−45°), and the upper bound is (45°,45°,45°). The earth is represented in dark green.

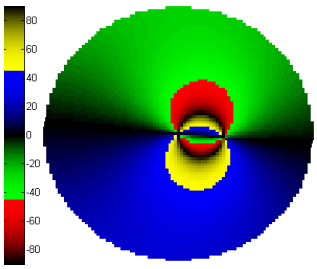

(a) Original α pattern

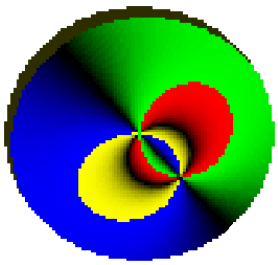

(b) α pattern rotated $-5°$around y, $40°$around z, and $7°$around x.

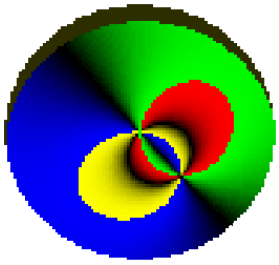

(c) First estimated rotation.

Correctly estimated solutions			
x	**y**	**z**	**Order**
1.5997	-14.1301	28.4087	1
1.4826	-14.3034	28.0335	2
-0.9179	-18.5157	19.3373	3
1.8691	-13.7397	29.2599	4

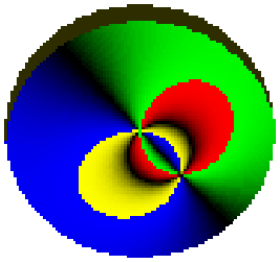

(d) Second estimated solution.

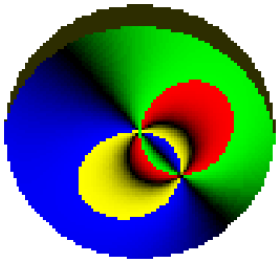

(e) Third estimated rotation.

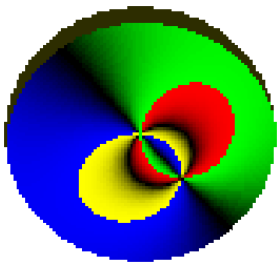

(f) Fourth estimated solution.

Figure 5.7: Estimating three angles of rotation where no knowledge is assumed. The simulation parameters are the same like figures (5.5a, 5.5b) where the original α pattern is rotated by $-5°$around y, $40°$around z, and $7°$around x respectively. The estimated solutions are shown in the second, third and fourth row. Note that the rotation order is not assumed to be known. The start point is $(0°,0°,0°)$, the lower bound is $(-45°,-45°,-45°)$, and the upper bound is $(45°,45°,45°)$. The earth is represented in dark green.

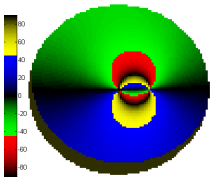

Correctly estimated solutions			
x	y	z	Order
5.1650	15.2724	25.658	1
5.0692	15.1152	25.277	2
4.5345	14.1881	23.072	3
4.7700	14.6072	24.061	4

(a) Estimating three angles of rotation where no knowledge is assumed about the rotation order however better lower (2°,12°,22°) and upper (8°,18°,28°) bounds are assumed to be provided. The robot is rotated by (5°, 15°, 25°) around x, y, and z respectively . The earth is represented in dark green.

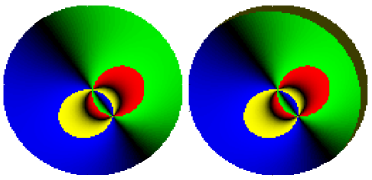

Correctly estimated equivalent solution			
x	y	z	Order
-8.0627	-7.8795	-6.3434	1

(b) Estimating one angle of rotation assuming no knowledge of the rotation axis. The robot is rotated around z-axis by 10°. The ground truth rotated α pattern is on the left and the computed rotated pattern based on the first estimation is shown on the right. The earth is represented in dark green. The simulation parameters are shown in table (5.6). Simulated pattern in Le Creusot on 26/07/2012 at 11:12:15

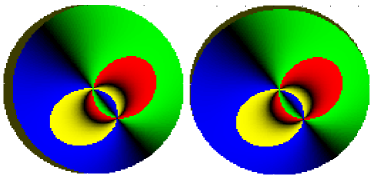

Correctly estimated equivalent solution solutions			
x	y	z	Order
1.9067	-5.3061	5.8858	1

(c) Estimating two angles of rotation assuming no knowledge of the rotation axises. The robot is rotated around x by 10°then around z by 20°. The ground truth rotated α pattern is on the left and the computed rotated pattern based on the first estimation is shown on the right. The earth is represented in dark green. The simulation parameters are shown in table (5.6). Simulated pattern in Le Creusot on 26/07/2012 at 11:12:15

Figure 5.8: Estimating angles of rotation assuming no knowledge of the rotation axises or rotation order.

5.3.3 Adding noise

Rotation estimation based on algorithms (5.11, 5.13) which depend on the $\pm 45°$ contours of the α pattern is faster and robuster than using algorithms (5.10, 5.12) which depend on the complete α pattern at points which has p higher than a given threshold. Hence a demonstration of the performance of these robust algorithms (5.11, 5.13) against high levels of noise is provided here as

they will always outperform algorithms (5.10, 5.12).

Gaussian noise with zero mean and $variance = 10$, Gaussian noise with $mean = 3$ and $variance = 10$, and speckle noise with zero mean and $variance = 0.04$ are added to each rotation estimation scenario respectively. The error found to be at maximum $\pm 2.48°$ for these high levels of noise and the average error was $\pm 0.5°$.

Figures (5.9a, 5.9b, 5.9c) show the results of adding noise on γ estimation (one angle of rotation) based on algorithm (5.11). Simulation parameters are shown in table (5.6).

Figures (5.10a, 5.10b, 5.10c) show the results of adding noise on two angles of rotation estimation based on algorithm (5.13).

As mentioned in sec (5.3.2), in practice if a better range is defined for upper and lower bounds on the rotation angles or a good starting point is provided then the possibility to converge to the exact solution is higher. Figures (5.11a, 5.11b, 5.11c) show the rotation estimation after adding Gaussian noise with zero mean and $variance = 10$, Gaussian noise with $mean = 3$ and $variance = 10$, and speckle noise with zero mean and $variance = 0.04$ to figure (5.8a) respectively.

Figures (B.32, B.33, B.34) in appendix (B) show the results of adding noise on general rotation estimation based on algorithm (5.13). The presented results in this section are shown with more simulation details in section (B.4).

Figure	Estimation	Error
Ground truth is 25°rotation around z-axis		
5.9a	24.6276°	0.3724°
5.9b	26.0435°	1.0435°
5.9c	25.9580°	0.958°

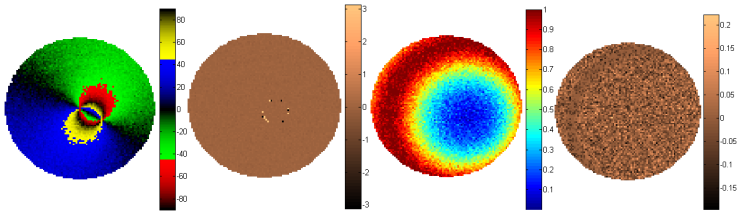

(a) γ estimation after adding Gaussian noise with zero mean and *variance* = 10. The simulation parameters are shown in table (5.6).

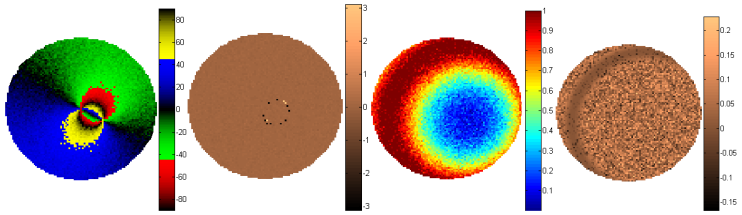

(b) γ estimation after adding Gaussian noise with *mean* = 3 and *variance* = 10. The simulation parameters are shown in table (5.6).

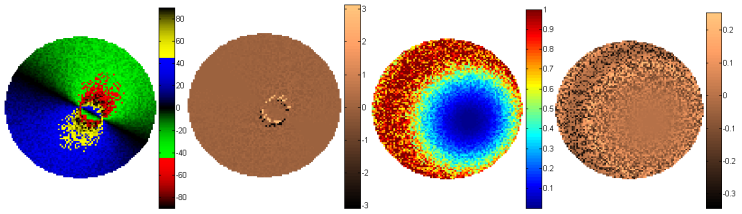

(c) γ estimation after adding speckle noise with zero mean and *variance* = 0.04.

Figure 5.9: γ estimation using algorithm (5.11) after adding noise. The table at the top shows the ground truth rotation, the estimated rotation, and the estimation error. Images from left to right are: the noisy rotated α pattern, the difference between the noisy and the theoretically rotated α pattern, the noisy rotated p pattern, and the difference between the noisy and the theoretically rotated p pattern. The simulation parameters are shown in table (5.6). Simulated pattern in Le Creusot on 24/07/2012 at 12:39:5.

Figure	Estimation	Error	Estimation	Error
Ground truth is:	10° around x-axis		20° around z-axis	
5.10a	12.0512°	2.0512°	21.0855°	1.0855°
5.10b	10.6650°	0.6650°	20.6087°	0.6087°
5.10c	11.0645°	1.0645°	21.9056°	1.9056°

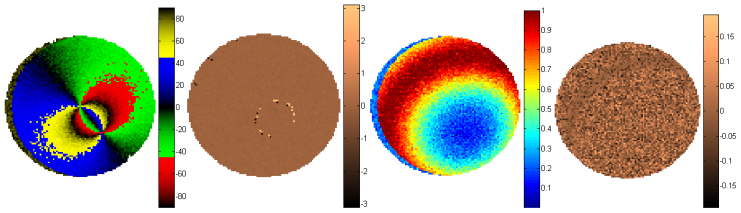

(a) Two angles of rotation estimation assuming the knowledge of the rotation axises after adding Gaussian noise with zero mean and $variance = 10$.

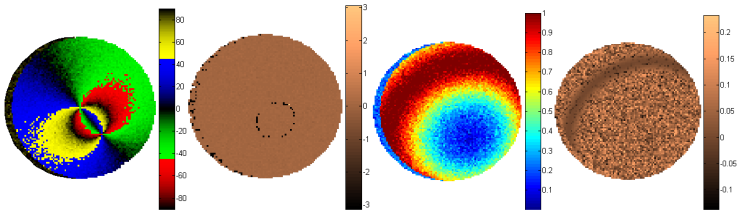

(b) Two angles of rotation estimation assuming the knowledge of the rotation axises after adding Gaussian noise with $mean = 3$ and $variance = 10$.

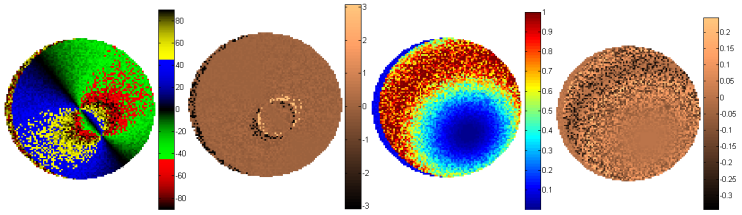

(c) Two angles of rotation estimation assuming the knowledge of the rotation axises after adding speckle noise with zero mean and $variance = 0.04$.

Figure 5.10: Two angles of rotation estimation assuming the knowledge of the rotation axises using algorithm (5.13) after adding noise. The table at the top shows the ground truth rotation, the estimated rotation, and the estimation error. Images from left to right are: the noisy rotated α pattern, the difference between the noisy and the theoretically rotated α pattern, the noisy rotated p pattern, and the difference between the noisy and the theoretically rotated p pattern. The earth is represented in dark green. The simulation parameters are shown in table (5.6). Simulated pattern in Le Creusot on 26/07/2012 at 11:12:15.

Figure	Estimation	Error	Estimation	Error	Estimation	Error
Ground truth is:	5° around x-axis		15° around y-axis		25° around z-axis	
5.11a	5.3505°	0.3505°	14.7630°	0.237°	24.8889°	0.1111°
5.11b	5.3269°	0.3269°	14.1094°	0.8906°	23.9005°	1.0995°
5.11c	5.4238°	0.4238°	14.6818°	0.3182°	27.4859°	2.4859°

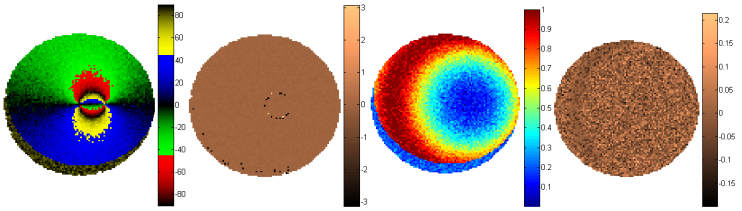

(a) Estimating three angles of rotation after adding a Gaussian noise with $mean = zero$ and $variance = 10$.

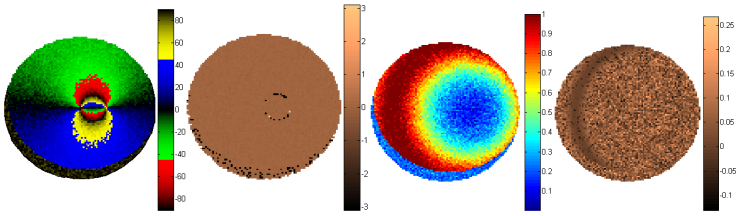

(b) Estimating three angles of rotation after adding a Gaussian noise with $mean = 3$ and $variance = 10$.

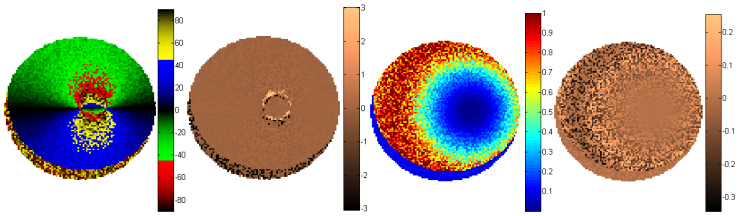

(c) Estimating three angles of rotation after adding speckle noise with $mean = zero$ and $variance = 0.04$.

Figure 5.11: Estimating three angles of rotation using algorithm (5.13) after adding noise where no knowledge is assumed about the rotation order however better lower (2°,12°,22°) and upper (8°,18°,28°) bounds are assumed to be provided. The robot is rotated by (5°, 15°, 25°) around x, y, and z respectively. The table at the top shows the ground truth rotation, the estimated rotation, and the estimation error. Images from left to right are: the noisy rotated α pattern, the difference between the noisy and the theoretically rotated α pattern, the noisy rotated p pattern, and the difference between the noisy and the theoretically rotated p pattern. The earth is represented in dark green. The simulation parameters are shown in table (5.6). Simulated pattern in Le Creusot on 24/07/2012 at 12:39:5.

Chapter 6

Conclusion and Perspectives

Animal's behavior is extremely flexible and robust facing environmental contingencies. By adopting some of these behaviors in machines, it is possible to obtain similar flexibility and robustness. Many aspects of animals lead to biological inspiration like a) behavioral strategies, b) physical design, and c) the nervous systems organization. In this work, we focused on the animals' polarization based visual behavior strategies.

Human visual awareness can be greatly expanded by augmenting different sensor models by the different capabilities of computer vision systems. Polarization vision represented in polarizational cameras becomes available to a broad range of audience, specifically outdoors and underwater applications. Unmanned robots for surveillance or exploring tasks may greatly benefit from such sensors. Thanks to polarizational cameras, it will be easier to have real time bio-inspired robotics.

Polarization information has strong cues for orientation and navigation. It can be used efficiently in communication, removing backscattering for underwater vision, breaking camouflage in complex backgrounds, and easily adapted in various machine vision applications where analyzed polarization filtered images proved to be useful.

A complete dedicated survey to one of the most important bio-inspired visual features in nowadays applications was presented in appendix (A). Many examples of skylight polarization patterns and the proposed applications were given in appendix (B). A comprehensive survey about vision based attitude estimation was given in chapter (2) and another survey about measuring skylight polarization patterns using omnidirectional sensors was given in chapter (3) along with a derivation of an accurate analytic form of the skylight angle of polarization. Our aim was measuring the polarization state of incident light using a catadioptric sensor. Hence we proved that, using the proposed pola-catadioptric design, only three out of four parameters are required to compute the incident polarization state as shown in chapter (4). The algorithms proposed to estimate solar angles and AV attitude directly serve AV orientation and navigation applications as shown in chapter (5).

For the sake of solar angles estimation, algorithms (5.6, 5.7) are highly rec-

ommended as they are fast, robust, and can be used in real time due to the small number of used points. Algorithms (5.11, 5.13) are also highly recommended for AV attitude estimation for the same reasons. It is worthy to note that all experiments were simulated on low resolution images 128×128 and against high levels of Gaussian and speckle noise.

This work emphasizes the significance of the $\pm 45°$ contour and the neutral line (in the angle of polarization α pattern) which are directly connected to the solar zenital and azimuthal angles respectively. These results suggest that animals highly depend on these features for orientation and navigation purposes. In literature, some animals need to observe any part of the sky with a sufficient degree of polarization p to be able to use polarization features. Actually, our results may recall two important questions: "Which part of the polarized skylight is sufficient for animals polarization based behavior?" , and "what if the animal is not able to observe one of these features, will it be able to take a correct decision?". These questions are left for biologists to re-answer.

We think that there are four important fields of polarization research which will evolve in the next few years: spectral-polarization vision, omni-polarization vision, a combination of both (omni-spectro-polarization vision), and night polarization vision. Independently, polarizational and spectral features do not completely represent an object of interest ([257]). The objects elemental composition defines the reflected spectral signature. The polarization characteristics depend on surface features, such as smoothness and conductance. These features can be combined to reduce false alarms, improve target identification, and enhance the scene description. Some work has already been done on this combination in ([71, 255, 257, 256, 47]). The future of polarization vision is going to be omni-directional due to its wide range of applications and the amount of information captured at one location and one shot. It takes the conventional vision applications into the omni-directional dimension. We propose to have an omni-spectro-polarizational camera (e.g combining a mirror with FD-1665 3CCD Multispectral Cameras with a linear polarizer at $0°$, $60°$, $120°$ in front of each camera). It is a combined inspiration of the birds' field of view (which can reach $360°$), the Daphnia magna spectral vision, and Cataglyphis ants polarization vision. The proposed sensor might be able to show the spectral and polarizational features from an omni-directional perspective. It can be used in almost all machine vision applications enhancing the quality of perceived images and fusing comprehensive information in a single image. It may greatly enhance the autonomous robotics world especially in open environments. To the best of our knowledge, here is the first time to propose such sensor. Also being inspired by the nocturnal, we think that in the near future it will be possible to use the skylight polarization patterns in the night for robot autonomous navigation like day light using the moon polarization patterns which are similar to sun polarization patterns ([48]).

One possible future application is a Natural Positioning System (NPS) that exploits the skylight polarization pattern to find out the latitude and longitude of the AV given date, time, and solar angles.

Bibliography

[1] Fd-1665p polarization camera, http://www.fluxdata.com/products/fd-1665-polarization-camera/.

[2] Gml ransac matlab toolbox.

[3] http://www.mathworks.com/matlabcentral/fileexchange/2422-phase-based-optical-flow.

[4] Noaa national oceanic and atomospheric administration, http://www.srrb.noaa.gov/highlights/sunrise/azel.html.

[5] J.E. Ahmad and Y. Takakura. Improving segmentation maps using polarization imaging. In *Image Processing, 2007. ICIP 2007. IEEE International Conference on*, volume 1, pages I –281 –I –284, 162007-oct.19 2007.

[6] M.E. Antone and S. Teller. Automatic recovery of relative camera rotations for urban scenes. pages II: 282–289, 2000.

[7] Y. Aron and Y. Gronau. Polarization in the lwir. In *Proceedings of SPIE*, volume 5783, pages 653–661, 2005.

[8] G.A. Atkinson and E.R. Hancock. Multi-view surface reconstruction using polarization. In *Proceedings of the Tenth IEEE International Conference on Computer Vision (ICCV05)*, 2005.

[9] S. Baker and S. K. Nayar. A theory of catadioptric image formation. In *International Conference on Computer Vision (ICCV03)*, pages 1351–1358, Oct 2003.

[10] G. Bao, Z. Zhou, S. Xiong, X. Lin, , and X.Ye. Towards micro air vehicle flight autonomy research on the method of horizon extraction. In *Instrumentation and Measurement Technology Conference, . IMTC '03. Proceedings of the 20th IEEE, 2003.*, 2003.

[11] S.T. Barnard. Interpreting perspective images. *Artificial Intelligence*, 21:435–462, 1984.

[12] G. Barrows, J. Chahl, and M. Srinivasan. Biomimetic visual sensing and flight control. In *Proceedings Seventeenth International Unmanned Air Vehicle Systems Conference*, 2002.

[13] A. Barta and G. Horváth. Why is it advantageous for animals to detect celestial polarization in the ultraviolet? skylight polarization under clouds and canopies is strongest in the uv. *J Theor Biol*, 226:429–437, 2004.

[14] A. Barta, G. Horváth, B. Bernáth, and V.B. Meyer-Rochow. Imaging polarimetry of the rainbow. *Applied Optics*, 42:399–405, 2003.

[15] J.C. Bazin, I.S. Kweon, C. Demonceaux, and P. Vasseur. Uav attitude estimation by combining horizon-based and homography-based approaches for catadioptric image. In *6th IFAC/EURON Intelligent Autonomous Vehicles (IAV07)*, Toulouse, France, 2007.

[16] J.C. Bazin, I.S. Kweon, C. Demonceaux, and P. Vasseur. Uav attitude estimation by vanishing points in catadioptric images. In *ICRA*, pages 2743–2749, 2008.

[17] C. Bellver. Influence of particulate pollution on positions of neutral points in the sky at seville (spain). *Atmospheric Environment*, 21:699–702, 1987.

[18] M. Ben-Ezra. Segmentation with invisible keying signal. In *Proceedings of IEEE Conference on Computer Vision and Pattern Recognition*, pages 32–37, 2000.

[19] S. Benedetto and P. Poggiolini. Theory of polarization shift keying modulation. *IEEE Transactions on Communications*, 40:708–721, 1992.

[20] B. Bernáth, J. Gál, and G. Horváth. Why is it worth flying at dusk for aquatic insects? polarotactic water detection is easiest at low solar elevations. *Journal of Experimental Biology*, 207:755–765, 2004.

[21] M. V. Berry, M. R. Dennis, and R. L. Jr. Lee. Polarization singularities in the clear sky. *New Journal of Physics*, 6:162, 2004.

[22] M. Born and E. Wolf. *Principles of Optics: Electromagnetic Theory of Propagation, Interference and Diffraction of Light (7th Edition)*. Cambridge University Press, 7th edition, October 1999.

[23] M. L. Brines and J.L. Gould. Skylight polarization patterns and animal orientation. *Journal of Experimental Biology*, 96:69–91, 1982.

[24] G. L. Brun, B. L. Jeune, J. Cariou, and J. Lotrian. Analysis of polarization signature of immersed targets. In *Proceedings of SPIE Polarization and Remote Sensing*, volume 1747, pages 128–139, 1992.

[25] N. Carey and W. Sturzl. An insect-inspired omnidirectional vision system including uv-sensitivity and polarisation. In *IEEE International Conference on Computer Vision Workshops, OMNIVIS*, 2011.

[26] J. Chahl and A. Mizutani. Biomimetic attitude and orientation sensors. *Sensors Journal, IEEE*, PP(99):1, 2010.

[27] S. Chandrasekar and D. Elbert. The illumination and polarization of the sunlit sky on rayleigh scattering. *Transactions of the American Philosophical Society*, 44:643 – 728, 1954.

[28] S. Chandrasekhar. *Radiative transfer*. Clarendon Press, Oxford, 1950.

[29] C.W. Chow, C. H. Kwok, Y. Liu, H.K. Tsang, and L. Chinlon. 3-bit/symbol optical modulation-demodulation simultaneously using drz, dpsk and polsk. In *Conference on Lasers and Electro-Optics (CLEO)*, 2006.

[30] J. Chu, H. Wang, W. Chen, and R. Li. Application of a novel polarization sensor to mobile robot navigation. In *Mechatronics and Automation, 2009. ICMA 2009. International Conference on*, pages 3763 –3768, 2009.

[31] J. Chu, K. Zhao, T. Wang, and Q. Zhang. Research on a novel polarization sensor for navigation. In *IEEE International Conference on Information Acquisition*, 2007.

[32] J. Chu, K. Zhao, Q. Zhang, and T. Wang. Design of a novel polarization sensor for navigation. In *IEEE International Conference on Mechatronics and Automation*, 2007.

[33] J. Chu, K. Zhao, Q. Zhang, and T. Wang. Construction and performance test of a novel polarization sensor for navigation. *Sensors and Actuators A: Physical*, 148:75–82, 2008.

[34] T.D. Cornall and G.K. Egan. Measuring horizon angle from video on a small unmanned air vehicle. In *2nd International Conference on Autonomous Robots and Agents, Palmerston North, New Zealand*, 2004.

[35] T.D. Cornall and G.K. Egan. Measuring horizon angle from video on a small unmanned air vehicle. Technical report, MONASH University, Department of Electrical and Computer Systems Engineering, 2005.

[36] T.D. Cornall, G.K. Egan, and A. Price. Aircraft attitude estimation from horizon video. *ELECTRONICS LETTERS*, 42(12), June 2006.

[37] K. L. Coulson. On the solar radiation field in a polluted atmosphere. *Journal of Quantitative Spectroscopy Radiation Transfer*, 2:739–755, 1971.

[38] K.L. Coulson. *Polarization and Intensity of Light in the Atmosphere*. A. DEEPAK Publishing, 1988.

[39] W.C. Cox, B.L. Hughes, and J.F. Muth. A polarization shift-keying system for underwater optical communications. In *OCEANS 2009, MTS/IEEE Biloxi - Marine Technology for Our Future: Global and Local Challenges*, 2009.

[40] W.C. Cox, J. Simpson, C.P. Domizioli, J. Muth, and B. Hughes. An underwater optical communication system implementing reed-solomon channel coding. In *Proceedings of OCEANS Conference*, 2008.

[41] T.W. Cronin and N. Shashar. The linearly polarized light field in clear, tropical marine waters: spatial and temporal variation of light intensity, degree of polarization, and e-vector angle. *J. Exp. Biol*, 204:2461 2467, 2001.

[42] T.W. Cronin, N. Shashar, R.L. Caldwell, J. Marshall, A.G. Cheroske, and T.H. Chiou. Polarization vision and its role in biological signaling. *Integr. Comp. Biol.*, 43(4):549–558, 2003.

[43] T.W. Cronin, N. Shashar, and L.B. Wolff. Portable imaging polarimeters. In *Pattern Recognition, 1994. Vol. 1 - Conference A: Computer Vision Image Processing., Proceedings of the 12th IAPR International Conference*, volume 1, pages 606 –609 vol.1, October 1994.

[44] T.W. Cronin, E.J. Warrant, and B. Greiner. Celestial polarization patterns during twilight. *Optical Society of America. Applied Optics*, 45, 2006.

[45] F. Crosby and S. Riley. Signature adaptive mine detection at a constant false alarm rate. In *Proceeding of SPIE Conference on Detection and Remediation Technologies for Mines and Minelike Targets*, 2001.

[46] F. Crosby and S. Stetson. Surface effect subtraction for airborne underwater target detection. In *OCEANS MTS/IEEE*, 2002.

[47] M.E. Cummings, S.A. Ahmed, H.M. Dierssen, A. Gilerson, W.F. Gilly, G.W. Kattawar, B.A. Seibel, and J.M. Sullivan. Biological response to the dynamic spectral-polarized underwater light field. Technical report, TEXAS UNIV AT AUSTIN, 2009.

[48] M. Dacke, M.J. Byrne, E. Baird, C.H. Scholtz, and E. Warrant. How dim is dim? precision of the celestial compass in moonlight and sunlight. *Phil. Trans. R. Soc. B*, 366:697–702, 2011.

[49] J.N. Damask. *Polarization optics in telecommunications*, volume 101. Springer, 2005.

[50] M. Dehmollaian and K. Sarabandi. Optimum polarizations for discrimination of a foliage-camouflaged target, using genetic algorithms. *IEEE Geoscience and Remote Sensing Letters*, 6(1):82 –86, 2009.

[51] C. Demonceaux, P. Vasseur, and C. Pegard. Omnidirectional vision on uav for attitude computation. In *ICRA*, pages 2842–2847, 2006.

[52] C. Demonceaux, P. Vasseur, and C. Pegard. Robust attitude estimation with catadioptric vision. In *IROS*, pages 3448–3453, 2006.

[53] C. Demonceaux, P. Vasseur, and C. Pegard. Uav attitude computation by omnidirectional vision in urban environment. In *ICRA*, pages 2017–2022, 2007.

[54] L.J. Denes, M. Gottlieb, B. Kaminsky, and P. Metes. Aotf polarization difference imaging. *SPIE*, 3584:106–115, 1998.

[55] P. Denis, J.H. Elder, and F.J. Estrada. Efficient edge-based methods for estimating manhattan frames in urban imagery. In *Proceedings of the 10th European Conference on Computer Vision: Part II*, pages 197–210, Berlin, Heidelberg, 2008. Springer-Verlag.

[56] J.M. Douglas, T.W. Cronin, T.H. Chiou, and N.J. Dominy. Light habitats and the role of polarized iridescence in the sen- sory ecology of neotropical nymphalid butterflies (lepidoptera: Nymphalidae). *Journal of Experimental Biology*, 210:788–799, 2007.

[57] D. Dusha, W. Boles, and R. Walker. Attitude estimation for a fixed-wing aircraft using horizon detection and optical flow. In *Proceedings of the 9th Biennial Conference of the Australian Pattern Recognition Society on Digital Image Computing Techniques and Applications*, DICTA '07, pages 485–492, Washington, DC, USA, 2007. IEEE Computer Society.

[58] W.G. Egan. Polarization in remote sensing. In *Proc. SPIE 1747*. Elsevier, 1992.

[59] W.G. Egan and M.J. Duggin. Optical enhancement of aircraft detection using polarization. In *Proceedings of SPIE*, volume 4133, pages 172–178, 2000.

[60] W.G. Egan and M.J. Duggin. Synthesis of optical polarization signatures of military aircraft. In *Proceedings of SPIE*, volume 4481, pages 188–194, 2002.

[61] S.M. Ettinger, M.C. Nechyba, P.G. Ifju, and M. Waszak. Vision-guided flight stability and control for micro air vehicles. In *IEEE/RSJ Int Conf on Robots and Systems*, pages 2134–2140, 2002.

[62] S.M. Ettinger, M.C. Nechyba, P.G. Ifju, and M. Waszak. Vision-guided flight stability and control for micro air vehicles. *Advanced Robotics*, 17(7):617–640, November 2003.

[63] D. Eynard, P. Vasseur, C. Demonceaux, and V. Fremont. Uav altitude estimation by mixed stereoscopic vision. In *Intelligent Robots and Systems (IROS), 2010 IEEE/RSJ International Conference on*, pages 646 –651, 2010.

[64] H. Farid and E.H. Adelson. Separating reflections and lighting using independent components analysis. In *Proceedings of IEEE Conference on Computer Vision and Pattern Recognition*, pages 262–267, 1999.

[65] G. Forssell and E. H. Karlsson. Measurements of polarization properties of camouflaged objects and of the denial of surfaces covered with cenospheres. In *Proceedings of SPIE*, volume 5075, pages 246–258, 2003.

[66] K.V. Frisch. Gelöste und ungelöste rätsel der bienensprache. *Naturwissenschaften*, pages 1: 12–23, 2: 38–43, 1948.

[67] K.V. Frisch. Die polarisation des himmeslichtes als orientierender faktor bei den tänzen der bienen. *Experientia*, 5:142–148, 1949.

[68] T. Furukawa and K. Sakamoto. Eye contact communication system between mobile robots using invisible code display. In Hyun Yang, Rainer Malaka, Junichi Hoshino, and Jung Han, editors, *Entertainment Computing ICEC 2010*, volume 6243 of *Lecture Notes in Computer Science*, page 468 471. Springer Berlin Heidelberg, 2010.

[69] G. Gebert, D. Snyder, J. Lopez, N. Siddiqi, and J. Evers. Optical flow angular rate determination. *Proc. of the International Conference on Image Processing*, 1:49–52, 2003.

[70] G. Gerhart and R. Matchko. Visualization techniques for four stokes parameter polarization. In *Proc. of the ground target modeling and validation conference*, pages 216–225, 2002.

[71] G.C. Giakos. Multifusion, multispectral, optical polarimetric imaging sensing principles. *IEEE Transactions on Instrumentation and MeasurementI*, 55:1628–1633, 2006.

[72] J.J GIBSON. The ecological approach to visual perception. *Houghton Mifflin, Boston*, 1950.

[73] J. Gál, G. Horváth, A. Barta, and R. Wehner. Polarization of the moonlit clear night sky measured by full-sky imaging polarimetry at full moon: comparison of the polarization of moonlit and sunlit skies. *Journal of Geophysical Research D*, 106:22647–22653, 2001a.

[74] J. Gál, G. Horváth, V. B. Meyer-Rochow, and R. Wehner. Polarization patterns of the summer sky and its neutral points measured by full-sky imaging polarimetry in finnish lapland north of the arctic circle. *Proceedings of the Royal Society of London A*, 457:1385–1399, 2001b.

[75] J. Gál, G. Horváth, and W.B. Meyer-Rochow. Measurement of the reflection-polarization pattern of the flat water surface under a clear sky at sunset. *Rem Sens Environ*, 76:103 – 111, 2001c.

[76] T.H. Goldsmith. The polarization sensitivity-dichroic absorption paradox in arthropod photoreceptors. *Photoreceptor optics, Springer Verlag, Berlin.*, A. W. Snyder and R. Menzel (eds.):98–125, 1975.

[77] D. Goldstein. Polarimetric characterization of federal standard paints. In *Proceedings of SPIE*, volume 4133, pages 112–123, 2000.

[78] D. Goldstein. *Polarized Light, Revised and Expanded (Optical Science and Engineering)*. CRC, 2 edition, June 2003.

[79] R.C. Gonzalez and R.E. Woods. *Digital Image Processing, 2E*. Tom Robbins, Prentice Hall, 2001.

[80] A. S. Green, P.R. Ohmann, N.E. Leininger, and J.A. Kavanaugh. Polarization imaging and insect vision. *The Physics Teacher*, 48(1):17–20, 2010.

[81] J. Grosinger. Investigation of polarization modulation in optical free space communications through the atmosphere. Master's thesis, Institut fur Nachrichtentechnik und Hochfrequenztechnik, eingereicht an der Technischen Universitat Wien, Fakultat fur Elektrotechnik und Informationstechnik, 2008.

[82] P. Gurfil and H. Rotstein. Partial aircraft state estimation from visual motion using the subspace constraints approach. *Journal of Guidance, Control, and Dynamics*, 24:1016–1028, 2001.

[83] W. Haidinger. Über das directe erkennen des polarisirten lichts und der lage der polarisationsebene. *Poggendorfs Annalen*, 63:29–39, 1844.

[84] R.T. Hanlon, M.R. Maxwell, N. Shashar, E.R. Loew, and K.L. Boyle. An ethogram of body patterning behavior in the biomedically and commercially valuable squid loligo pealei off cape cod. *Massachusetts. Biol Bull*, 197:49–62, 1999.

[85] R.T. Hanlon and J.B. Messenger. *Cephalopod Behaviour*. Cambridge, UK: Cambridge University Press, 1996.

[86] F. Hanson and S. Radic. High bandwidth underwater optical communication. *Applied Optics*, 47:277–283, 2008.

[87] S. Harsdorf, R. Reuter, and S. Tönebön. Contrast-enhanced optical imaging of submersible targets. *SPIE*, 3821:378–383, 1999.

[88] C. Hawryshyn. Polarization vision in fish. *American Scientist*, 80:164–175, 1992.

[89] C. Hedden. Vision-based uav aerodynamic attitude estimation in the presence of dynamic obstacles. University of Kansas, 12 2010.

[90] Åkesson S. Wehner R. Hegedüs, R. and G. Horváth. Could vikings have navigated under foggy and cloudy conditions by skylight polarization? on the atmospheric optical prerequisites of polarimetric viking navigation under foggy and cloudy skies. *Proceedings of the Royal Society of London A*, 463:1081–1095, 2007d.

[91] R. Hegedüs, A. Barta, B. Bernáth, V.B. Meyer-Rochow, and G. Horváth. Imaging polarimetry of forest canopies: how the azimuth direction of the sun, occluded by vegetation, can be assessed from the polarization pattern of the sunlit foliage. *Applied Optics*, 46:6019–6032, 2007e.

[92] R. Hegedüs, S. Åkesson, and G. Horváth. Polarization patterns of thick clouds: overcast skies have distribution of the angle of polarization similar to that of clear skies. *J. Opt. Soc. Am.*, 24:2347–2356, 2007.

[93] R. Hegedüs, S. Åkesson, and G. Horváth. Anomalous celestial polarization caused by forest fire smoke: why do some insects become visually disoriented under smoky skies. *Applied Optics*, 46:2717–2726, 2007a.

[94] R. Hegedüs, S. Åkesson, and G. Horváth. Polarization patterns of thick clouds: Overcast skies have distribution of the angle of polarization similar to that of clear skies. *Journal of the Optical Society of America A*, 24:2347–2356, 2007b.

[95] R. Hegedüs, S. Åkesson, and G. Horváth. Polarization of "water-skies" above arctic open waters: how polynyas in the ice-cover can be visually detected from a distance. *Journal of the Optical Society of America A*, 24:132–138, 2007c.

[96] J. Heidemann, W. Ye, J. Wills, A. Syed, and Y. Li. Research challenges and applications for underwater sensor networking. In *In Proceedings of the IEEE Wireless Communications and Networking Conference*, pages 228–235, 2006.

[97] G.C. Holzworth and C.R. Rao. Studies of skylight polarization. *Journal of the Optical Society of America*, 55:403–408, 1965.

[98] G. Horváth. *POLARIZATION PATTERNS IN NATURE Imaging Polarimetry with Atmospheric Optical and Biological Applications*. PhD thesis, Hungarian Academy of Sciences, 2003.

[99] G. Horváth, A. Barta, J. Gál, B. Suhai, and O. Haiman. Ground-based full-sky imaging polarimetry of rapidly changing skies and its use for polarimetric cloud detection. *Applied Optics*, 41:543–559, 2002c.

[100] G. Horváth, B. Bernáth, B. Suhai, A. Barta, and R. Wehner. First observation of the fourth neutral polarization point in the atmosphere. *Journal of the Optical Society of America A*, 19:2085–2099, 2002a.

[101] G. Horváth, J. Gál, T. Labhart, and R. Wehner. Does reflection polarization by plants influence colour perception in insects? polarimetric measurements applied to a polarization-sensitive model retina of papilio butterflies. *Journal of Experimental Biology*, 205:3281–3298, (2002b).

[102] G. Horváth, J. Gál, and R. Wehner. Why are water-seeking insects not attracted by mirages? the polarization properties of mirages. *Naturwissenschaften*, 84:300–303, 1997.

[103] G. Horváth and D. Varjú. Polarization pattern of freshwater habitats recorded by video polarimetry in red, green and blue spectral ranges and its relevance for water detection by aquatic insects. *Journal of Experimental Biology*, 200:1155–1163, 1997.

[104] G. Horváth and D. Varjú. *Polarized Light in Animal Vision: Polarization Patterns in Nature*. Springer-Verlag, Heidelberg - Berlin - New York, 2004.

[105] S.C. Hsieh, L.K. Wang, F.B. Hsaio, K.Y. Huang, and F.J. Tsai. Airborne attitude/ground target location determinations using unscented kalman filter. In *Aerospace Conference, 2004. Proceedings. 2004 IEEE*, volume 3, pages 6 vol. (xvi+4192), 2004.

[106] D.F. Huber, L. Denes, M. Hebert, M. Gottlieb, B. Kaminsky, and P. Metes. A spectro-polarimetric imager for intelligent transportation systems. In *SPIE International Symposium on Intelligent Systems and Advanced Manufacturing, Intelligent Transportation Systems*, volume 3207, 1997.

[107] M. Hwangbo and T. Kanade. Visual-inertial attitude estimation using urban scene regularities. In *To appear in IEEE International Conference on Robotics and Automation*, 2011.

[108] M. Iqbal, O. Morel, and F. Meriaudeau. A survey on outdoor water hazard detection. In *The 5th International Conference on Information & Communication Technology and Systems*, 2010.

[109] A. Ivanoff and T.H. Waterman. Factors, mainly depth and wavelength, affecting the degree of underwater light polarization. *J. Mar. Res*, 16:283–307, 1958.

[110] R.V. Iyer, Z. He, and P.R. Chandler. On the computation of the ego-motion and distance to obstacles for a micro air vehicle. *Proc. of the IEEE American Control Conference*, 2006.

[111] N. Karpel and Y.Y. Schechner. Portable polarimetric underwater imaging system with a linear response. In *Proc. SPIE Polarization: Measurement, Analysis and Remote Sensing VI*, 2004.

[112] J. Kehoe, R. Causey, A. Arvai, and R. Lind. Partial aircraft state estimation from optical flow using non-model-based optimization. *Proc. of the IEEE American Control Conference*, 2006.

[113] J.J. Kehoe, A.S. Watkins, R.S. Causey, and R. Lind. State estimation using optical flow from parallax-weighted feature tracking. *Proceedings of the AIAA Guidance, Navigation, and Control Conference*, 2006.

[114] G.P. Können. *Polarized Light in Nature*. Cambridge University Press, Cambridge, UK, 1985.

[115] D. Lambrinos, M. Maris, H. Kobayashil, T. Labhart, R. Pfeifer, and R. Wehner. An autonomous agent navigation with a polarized light compass. *Adaptive Behaviour*, 6:131–161, 1997.

[116] D. Lambrinos, M. Maris, H. Kobayashil, T. Labhart, R. Pfeifer, and R. Wehner. Navigating with a polarized light compass. In *Self-Learning Robots II: Bio-robotics (Digest No. 1998/248), IEE*, pages 7/1 –7/4, February 1998.

[117] D. Lambrinos, R. Möller, T. Labhart, R. Pfeifer, and R. Wehner. A mobile robot employing insect strategies for navigation. *Robotics and Autonomous Systems*, 30:39–64, 2000.

[118] J. K. Lee and S. Mudaliar. Optimum polarizations in the bistatic scattering from layered random media. *IEEE Transactions on Geoscience and Remote Sensing*, 32:169–176, 1994.

[119] R.L. Lee. Digital imaging of clear-sky polarization. *Applied Optics*, 37:1465–1476, 1998.

[120] A. Lerner, S. Sabbah, C. Erlick, and N. Shashar. Navigation by light polarization in clear and turbid waters. *Philosophical Transactions of The Royal Society Biological Sciences*, 366:671–679, 2010.

[121] Y. Li and S. Wang. Underwater polarization imaging technology. In *Conference on Lasers Electro Optics The Pacific Rim*, pages 1 –2, 2009.

[122] Y. Li and S. Wang. Underwater object detection technology based on polarization image fusion. In *5th International Symposium on Advanced Optical Manufacturing and Testing Technologies: Optoelectronic Materials and Devices for Detector, Imager, Display, and Energy Conversion Technology, Proc. of SPIE*, 2010.

[123] S.S. Lin, K.M. Yemelyanov, E.N.Jr. Pugh, and N. Engheta. Polarization enhanced visual surveillance techniques. In *Proceedings of the IEEE International Conference on Networking. Sensing & Control*, 2004.

[124] J.N. Lythgoe and C.C. Hemmings. Polarized light and underwater vision. *Nature*, 213:893 894, 1967.

[125] D. Malacara. Physical optics and light measurements. In *Academic Press*, page 157, 1989.

[126] L. Matthies, P. Bellutta, and M. Mchenry. Detecting water hazards for autonomous off-road navigation. In *Proceedings of SPIE Conference 5083: Unmanned Ground Vehicle Technology V*, pages 263–352, 2003.

[127] J. Meeus. *Astronomical Algorithms*. Willmann-Bell, Inc., 1991.

[128] F. Meriaudeau, M. Ferraton, C. Stolz, L. Bigué, and O. Morel. Polarization imaging for industrial inspection. In *SPIE Electronic Imaging - Machine Vision Applications in Industrial Inspection XIII*, volume 6813, 2008.

[129] D. Miyazaki, M. Ammar, R. Kawakami, and K. Ikeuchi. Estimating sunlight polarization using a fish-eye lens. *IPSJ Transactions on Computer Vision and Applications*, 1:288 – 300, 2009.

[130] R. Möller, D. Lambrinos, R. Pfiefer, T. Labhart, and R. Wehner. Modeling ant navigation with an autonomous agent. In *Proceedings of the fifth international conference on simulation of adaptive behavior on From animals to animats*, 1998.

[131] I.F. Mondragón, P. Campoy, C. Martínez, and M. Olivares. Omnidirectional vision applied to unmanned aerial vehicles uavs attitude and heading estimation. *Robotics and Autonomous Systems*, March 2010.

[132] I.F. Mondragón, M. Olivares, P. Campoy, C. Martínez, and L. Mejias. Unmanned aerial vehicles uavs attitude, height, motion estimation and control using visual systems. *Autonomous Robots*, 29, 2010.

[133] R.J.D. Moore, S. Thurrowgood, D. Bland, D. Soccol, and M.V. Srinivasan. A stereo vision system for uav guidance. In *IEEE/RSJ International Conference on Intelligent Robots and Systems*, 2009.

[134] R.J.D. Moore, S. Thurrowgood, D. Bland, D. Soccol, and M.V. Srinivasan. Uav altitude and attitude stabilisation using a coaxial stere ovision system. In *IEEE International Conference on Robotics and Automation*, 2010.

[135] R.J.D. Moore, S. Thurrowgood, D. Soccol, D. Bland, and M.V. Srinivasan. A bio-inspired stereo vision system for guidance of autonomous aircraft. *Advances in Theory and Applications of Stereo Vision*, 2010.

[136] O. Morel. *Environnement actif pour la reconstruction tridimensionnelle de surfaces métalliques spéculaires par imagerie polarimétrique*. PhD thesis, Université de Bourgogne, 2005.

[137] O. Morel. http://www.geogebratube.org/student/m7829, 2012.

[138] O. Morel, M. Ferraton, C. Stolz, and P. Gorria. Active lighting applied to shape from polarization. In *IEEE ICIP06*, pages 2181–2184, 2006.

[139] O. Morel and D. Fofi. Calibration of catadioptric sensors by polarization imaging. In *Robotics and Automation, 2007 IEEE International Conference on*, pages 3939–3944, 2007.

[140] O. Morel, R. Seulin, and D. Fofi. Catadioptric camera calibration by polarization imaging. In *IAPR 3rd Iberian Conference on Pattern Recognition and Image Analysis (IbPRIA'2007)*, 2007.

[141] O. Morel, R. Seulin, and D. Fofi. Measurement of the three-dimensional mirror parameters by polarization imaging applied to catadioptric camera calibration. In *IEEE/SPIE 8th International Conference on Quality Control by Artificial Vision (QCAV'2007)*, 2007.

[142] O. Morel, R. Seulin, and D. Fofi. Measurement of three-dimensional mirror parameters by polarization imaging applied to catadioptric camera calibration. *Journal of Electronic Imaging*, 17(3), 2008.

[143] O. Morel, C. Stolz, and P. Gorria. Application of polarimetric imaging to 3d inspection of highly reflective metallic surface. In *SPIE Optics East - Two- and Three-Dimensionale Vision Systems for Inspection, Control, and Metrology II*, volume 5606, pages 82–89, 2004.

[144] O. Morel, C. Stolz, and P. Gorria. Polarization applied to 3d reconstruction of highly reflective metallic objects. In *OSAV*, 2004.

[145] O. Morel, C. Stolz, and P. Gorria. Polarization imaging for 3d inspection of highly reflective metallic objects. *Optics and Spectroscopy*, 101(1):15–21, 2006.

[146] O. Morel, C. Stolz, F. Meriaudeau, and P. Gorria. Three-dimensional inspection of highly-reflective metallic objects by polarization imaging, 2005.

[147] O. Morel, C. Stolz, F. Meriaudeau, and P. Gorria. Three-dimensional inspection of highly-reflective metallic objects by polarization imaging. *Electronic Imaging Newsletter*, 15(2):4, 2005.

[148] O. Morel, C. Stolz, F. Meriaudeau, and P. Gorria. Active lighting applied to 3d reconstruction of specular metallic surfaces by polarization imaging. *Applied Optics*, 45(17):4062–4068, 2006.

[149] S.P. Morgan, M.P. Khong, and M.G. Somekh. Effects of polarization state and scatterer concentration on optical imaging through scattering media. *Applied Optics*, 36:1560–1565, 1997.

[150] L.M. Mäthger and R.T. Hanlon. Anatomical basis for camouflaged polarized light communication in squid. *Biology letters*, 2(4):494–496, 2006.

[151] S. K. Nayar, X. S. Fang, and T. Boult. Separation of reflection components using color and polarization. *International Journal of Computer Vision*, 21:163–186, 1997.

[152] H. Neuberger. Arago's neutral point: a neglected tool in meteorological research. *Bulletin of the American Meteorological Society*, 31:119–125, 1950.

[153] W. Niblack and E. Wolf. Polarization modulation and demodulation of light. *Applied Optics*, 3:277–277, 1964.

[154] D.E. Nilsson and E.J. Warrant. Visual discrimination: Seeing the third quality of light. *Curr. Biol, 9R535-R537.*, 9:535–537, 1999.

[155] J. A. North and M. J. Duggin. Stokes vector imaging of the polarized sky-dome. *Applied Optics*, 36:723–730, 1997.

[156] F.I. Novales and C. W. Hawryshyn. Is the use of underwater polarized light by fishes restricted to crepuscular time periods? *Vision Res*, 37:975–989, 1997.

[157] A. Pandian. Robot navigation using stereo vision and polarization imaging. Master's thesis, Institut Universitaire de Technologie IUT Le Creusot, University of Burgundy, VIBOT master, 2008.

[158] J.B. Phillips and J.A. Waldvogel. Celestial polarized light patterns as a calibration reference for sun compass of homing pigeons. *Journal of Theoretical Biology*, 131:55–67, 1988.

[159] I. Pomozi, J. Gál, G. Horváth, and R. Wehner. Fine structure of the celestial polarization pattern and its temporal change during the total solar eclipse of 11 august 1999. *Rem Sens Environ*, 76:181 – 201, 2001a.

[160] I. Pomozi, G. Horváth, and R. Wehner. How the clear-sky angle of polarization pattern continues underneath clouds: full-sky measurements and implications for animal orientation. *The Journal of Experimental Biology*, 204:2933–2942, 2001.

[161] I. Pomozi, G. Horváth, and R. Wehner. How the clear-sky angle of polarization pattern continues underneath clouds: full-sky measurements and implications for animal orientation. *J Exp Biol*, 204(17):2933–2942, 2001b.

[162] W.K. Pratt. *Laser Communication Systems*. New York: Wiley, 1969.

[163] S. Pun, C. Chan, and L. Chen. A novel optical frequency shift keying transmitter based on polarization modulation. In *Optical Fiber Communication Conference. Technical Digest. OFC/NFOEC*, volume 3, 2005.

[164] T. Ramskou. Solstenen. *Skalk*, 2:16–17, 1967.

[165] T. Ramskou. *Solstenen - Primitiv Navigation I Norden for Kompasset*. Rhodos, Kobenhavn, 1969.

[166] A. Rankin and L. Matthies. Daytime mud detection for unmanned ground vehicle autonomous navigation. In *Proceedings of the 26th Army Science Conference*, 2008.

[167] S. Rossel. Polarization sensitivity in compound eyes. *Facets of vision, Springer Verlag, Berlin*, In D. G. Stavenga and R. C. Hardie (eds.):298–316, 1989.

[168] C. Rother. A new approach for vanishing point detection in architectural environments. In *In Proc. 11th British Machine Vision Conference*, pages 382–391, 2000.

[169] M.P. Rowe, E.N.Jr. Pugh, J.S. Tyo, and N. Engheta. Polarization-difference imaging: a biologically inspired technique for observation through scattering media. *Optics Letters*, 20:608–610, 1995.

[170] A. Rozhok. Orientation and navigation cues. In *Orientation and Navigation in Vertebrates*, pages 1–76. Springer Berlin Heidelberg, 2008.

[171] M. Saito, Y. Sato, K. Ikeuchi, and H. Kashiwagi. Measurement of surface orientations of transparent objects using polarization in highlight. *Journal of the Optical Society of America*, 16(9):2286 – 2293, 1999.

[172] M. Saito, Y. Sato, K. Ikeuchi, and H. Kashiwagi. Measurement of surface orientations of transparent objects using polarization in highlight. In *Proceedings of IEEE Conference on Computer Vision and Pattern Recognition*, 1999.

[173] A. Sarafraz, S. Negahdaripour, and Y.Y. Schechner. Enhancing images in scattering media utilizing stereovision and polarization. In *Proceedings of IEEE Workshop on Applications of Computer Vision*, 2009.

[174] M. Sarkar, D.S.S. Bello, C.V. Hoof, and A. Theuwissen. Biologically inspired autonomous agent navigation using an integrated polarization analyzing cmos image sensor. *Procedia Engineering*, 5:673 – 676, 2010. Eurosensor XXIV Conference, Eurosensor XXIV Conference.

[175] M. Sarkar, D.S.S. Bello, C.V. Hoof, and A. Theuwissen. Integrated polarization-analyzing cmos image sensor. In *Circuits and Systems (ISCAS), Proceedings of 2010 IEEE International Symposium on*, pages 621 –624, 302010-june2 2010.

[176] M. Sarkar, D.S.S. Bello, C.V. Hoof, and A. Theuwissen. Integrated polarization analyzing cmos image sensor for autonomus navigation using polarized light. In *IEEE Conf. of Intelligent Systems*, pages 224–229, 2010.

[177] M. Sarkar, D.S.S. Bello, C.V. Hoof, and A. Theuwissen. Integrated polarization-analyzing cmos image sensor for detecting incoming light ray direction. In *IEEE Sensors Applications Symposium (SAS)*, pages 194 –199, 2010.

[178] A. Sarwal, J. Nett, and D. Simon. Detection of small water-bodies. Technical report, PercepTek Robotics 12395 N. Mead Way Littleton, CO 80125, 2004.

[179] Y. Y. Schechner, J. Shamir, and N. Kiryati. Polarization-based decorrelation of transparent layers: The inclination angle of an invisible surface. In *Proceedings of IEEE International Conference on Computer Vision*, pages 814–819, 1999.

[180] Y. Y. Schechner, J. Shamir, and N. Kiryati. Polarization and statistical analysis of scenes containing a semi-reflector. *Journal of the Optical Society of America A*, 17:276–284, 2000.

[181] Y.Y. Schechner and N. Karpel. Clear underwater vision. In *IEEE Conference on Computer Vision and Pattern Recognition*, page 536 543, 2004.

[182] Y.Y. Schechner and N. Karpel. Recovery of underwater visibility and structure by polarization analysis. *IEEE Journal of Oceanic Engineering*, 30:631–636, 2005.

[183] Y.Y. Schechner, S.G. Narasimhan, and S.K. Nayar. Instant dehazing of images using polarization. In *Proceedings of IEEE Conference on Computer Vision and Pattern Recognition*, pages 325–332, 2001.

[184] Y.Y. Schechner, S.G. Narasimhan, and S.K. Nayar. Polarization-based vision through haze. *Applied Optics*, 42:511–525, 2003.

[185] Y.Y. Schechner, S.G. Narasimhan, and S.K. Nayar. Polarization-based vision through haze. In *Proceeding of ACM SIGGRAPH ASIA*, volume 42, 2008.

[186] A. Schmolke and H.A. Mallot. Polarisation compass for robot navigation. In *D. Polani, J. Kim, & T. Martinez (eds.) Fifth German Workshop on Artificial Life*, 2002.

[187] D.L. Schuler, J.S. Lee, and K.W. Hoppel. Polarimetric sar image signatures of the ocean and gulf stream features. *IEEE Transactions on Geoscience and Remote Sensing*, 31:1210–1221, 1993.

[188] R. Schwind. Zonation of the optical environment and zonation in the rhabdom structure within the eye of the backswimmer, notonecta glauca. *Cell and Tissue Research*, 232:53–63, 1983.

[189] R. Schwind. The plunge reaction of the backswimmer notonecta glauca. *Journal of Comparative Physiology*, A, 155:319–321, 1984.

[190] R. Schwind. Polarization vision in water insects and insects living on a moist substrate. *Journal of Comparative Physiology*, A, 169:531–540, 1991.

[191] Z. Sekera. Light scattering in the atmosphere and the polarization of skylight. *Journal of the Optical Society of America*, 47:484–490, 1957.

[192] A. E. R. Shabayek, C. Demonceaux, O. Morel, and D. Fofi. Vision based uav attitude estimation: Progress and insights. *Journal of Intelligent & Robotic Systems*, 65:295–308, 2012.

[193] A. E. R. Shabayek, O. Morel, and D. Fofi. Visual behaviour based bio-inspired polarization techniques in computer vision and robotics. In *International Workshop on Bio-Inspired Robots, Nants, France*, April, 2011.

[194] A.E.R. Shabayek. *Non-Central Catadioptric Sensors Auto-Calibration*. LAP Lambert Academic Publishing, 2010.

[195] A.E.R. Shabayek, D. Fofi, and O. Morel. A novel non-central catadioptric auto-calibration approach. In *9th Workshop on Omnidirectional Vision (OMNIVIS) in conjunction with International Conference on Computer Vision (ICCV)*, 2009.

[196] A.E.R. Shabayek, O. Morel, and D. Fofi. Auto-calibration and 3d reconstruction with non-central catadioptric sensors using polarization imaging. In *10th Workshop on Omnidirectional Vision (OMNIVIS) in conjunction with Robotics Systems and Science RSS*, 2010.

[197] A.E.R. Shabayek, O. Morel, and D. Fofi. *Developing and Applying Biologically-Inspired Vision Systems: Interdisciplinary Concepts*, chapter Visual Behavior Based Bio-Inspired Polarization Techniques in Computer Vision and Robotics. IGI Global, 2013.

[198] N. Shashar, L. Adessi, and T.W. Cronin. Polarization vision as a mechanism for detection of transparent objects. *Ultraviolet radiation and coral reefs, HIMB Tech*, D. Gulko and P. L. Jokiel (eds.):207 211, 1995. Rept. 41, pp.207 211. UHIHI-Sea Grant-CR-95-03.

[199] N. Shashar, T.W. Cronin, L.B. Wolff, and M.A. Condon. The polarization of light in a tropical rain forest. *Biotropica*, 30:275–285, 1998.

[200] N. Shashar, R. Hagan, J.G. Boal, and R.T. Hanlon. Cuttlefish use polarization sensitivity in predation on silvery fish. *Vision Res*, 40:71–75, 2000.

[201] N. Shashar and R.T. Hanlon. Squids (loligo pealii and euprymna scolopes) can exhibit polarized light patterns produced by their skin. *The Biological Bulletin*, 193:207–208, 1997.

[202] N. Shashar, R.T. Hanlon, and A.D. Petz. Polarization vision helps detect transparent prey. *Nature*, 393:222–223, 1998.

[203] N. Shashar, C. Milbury, and R.T. Hanlon. Polarization vision in cephalopods: Neuroanatomical and behavioral features that illustrate aspects of form and function. *Marine and Freshwater Behaviour and Physiology*, 35:57 68, 2002.

[204] N. Shashar, S. Sabbah, and T.W. Cronin. Transmission of linearly polarized light in seawater: implications for polarization signaling. *Journal of Experimental Biology*, 207:3619–3628, 2004.

[205] J. A. Shufelt. Performance evaluation and analysis of vanishing point detection techniques. *Pattern Analysis and Machine Intelligence, IEEE Transactions on*, 21(3):282–288, 1999.

[206] A. M. Shutov. Videopolarimeters. *Soviet Journal of Optical Technology*, 60:295–301, 1993.

[207] S. Soatto, R. Frezza, and P Perona. Motion estimation via dynamic vision. *IEEE Transactions on Automatic Control*, 41:393–413, 1996.

[208] S. Soatto and P. Perona. Recursive 3-d visual motion estimation using subspace constraints. *International Journal of Computer Vision*, 22:235–259, 1997.

[209] J. Stowers, A. Bainbridge-Smith, M. Hayes, and S. Mills. Optical flow for attitude estimation of a quadrotor helicopter. *European Micro Air Vehicle Conference*, 2009.

[210] N. Subramaniam and E. Hancock. Surface material segmentation using polarisation. *Lecture Notes in Computer Science*, 6256:115–124, 2010.

[211] B. Suhai and G. Horváth. How well does the rayleigh model describe the e-vector distribution of skylight in clear and cloudy conditions? a full-sky polarimetric study. *Journal of the Optical Society of America A*, 21:1669–1676, 2004.

[212] A. Sweeney, C. Jiggins, and S. Johnsen. Insect communication: Polarized light as a butterfly mating signal. *Nature*, 423:31–32, May 2003.

[213] C. H. Tang and M. D. Rubin. Optimum polarization for rain cancellation. In *Proceedings of IEEE Antennas and Propagation Society International Symposium*, volume 10, 1972.

[214] M. Tarhan and E. Altug. Ekf based attitude estimation and stabilization of a quadrotor uav using vanishing points in catadioptric images. *Journal of Intelligent & Robotic Systems*, pages 1–21–21, September 2010.

[215] B. Taylor, C. Bil, and S. Watkins. Horizon sensing attitude stabilisation: A vmc autopilot. In *18th International UAV Systems Conference*, 2003.

[216] J.S.Jr. Taylor, P.S. Davis, and L.B. Wolff. Underwater partial polarization signatures from the shallow water real-time imaging polarimeter (shrimp). In *OCEANS MTS/IEEE*, 2002.

[217] J.S.Jr. Taylor, P.S. Davis, and L.B. Wolff. Underwater partial polarization signatures from the shallow water real-time imaging polarimeter (shrimp). In *Spie proceedings, Detection and Remediation Technologies for Mines and Minelike Targets VIII*, 2003.

[218] J.S.Jr. Taylor and L.B. Wolff. Partial polarization signature results from the field testing of the shallow water real-time imaging polarimeter (shrimp). In *OCEANS MTS/IEEE Conference and Exhibition*, 2001.

[219] P. Terrier, V. Devlaminck, and J.M. Charbois. Segmentation of rough surfaces using a polarization imaging system. *Optical Society of America*, 25(2):423–430, Feb 2008.

[220] S. Thurrowgood, D. Soccol, R.J.D. Moore, D. Bland, and M.V. Srinivasan. A vision based system for attitude estimation of uavs. In *IEEE/RSJ International Conference on Intelligent Robots and Systems*, 2009.

[221] V. A. Timofeeva. Plane of vibrations of polarized light in turbid media. *Izvestiya Atmos. Ocean. Physics*, 5:603–607, 1969.

[222] S. Todorovic and M.C. Nechyba. Sky/ground modeling for autonomous mav flight. In *In IEEE International Conference on Robotics and Automation (ICRA*, pages 1422–1427, 2003.

[223] S. Todorovic and M.C. Nechyba. A vision system for intelligent mission profiles of micro air vehicles. *IEEE Transactions on Vehicular Technology*, 53:1713–1725, 2004.

[224] T. Treibitz and Y.Y. Schechner. Instant 3descatter. In *Proc. IEEE Computer vision and pattern recognision*, 2006.

[225] T. Treibitz and Y.Y. Schechner. Active polarization descattering. *IEEE Transactionson pattern analysis and machine intelligence*, 31:385–399, 2009.

[226] J.S. Tyo. Optimum linear combination strategy for an n-channel polarization-sensitive imaging or vision system. *Journal of Optical Society*, 15:359–366, 1998.

[227] H. Uehara, I. Seto, T. Ohtsuki, I. Sasase, and S. Mori. Phase noise insensitive multilevel polsk based on qam mapping in coherent optical systems. In *Singapore ICCS/ISITA. Communications on the Move*, 1992.

[228] K. Usher, P. Ridley, and P. Corke. A camera as a polarized light compass: Preliminary experiments. In *Australian Conference on Robotics and Automation*, 2001.

[229] K. J. Voss and Y. Liu. Polarized radiance distribution measurements of skylight. i. system description and characterization. *Applied Optics*, 36:6083–6094, 1997.

[230] A. Wallace, B. Liang, E. Trucco, and J. Clark. Improving depth image acquisition using polarized light. *International Journal of Computer Vision*, 32(2):87–109, 1999.

[231] L.K. Wang, S.-C. Hsieh, E.C.-W. Hsueh, Fei-Bin Hsaio, and Kou-Yuan Huang. Complete pose determination for low altitude unmanned aerial vehicle using stereo vision. In *Intelligent Robots and Systems, 2005. (IROS 2005). 2005 IEEE/RSJ International Conference on*, pages 108 – 113, 2005.

[232] T.H. Waterman. Polarization sensitivity. *H. Autrum (ed.), Handbook of sensory physiology, Springer Verlag, Berlin.*, VII/6B:281–463, 1981.

[233] T.H. Waterman. Polarization of marine light fields and animal orientation. *SPIE*, 925:431–437, 1988.

[234] T. Webb, R. Prazenica, A. Kurdila, and R. Lind. Vision-based state estimation for autonomous micro air vehicles. *Proc. of the AIAA Guidance, Navigation, and Control Conference*, page 5249, 2004.

[235] T. Webb, R. Prazenica, A. Kurdila, and R. Lind. Vision-based state estimation for uninhabited aerial vehicles. *Proc. of the AIAA Guidance, Navigation, and Control Conference*, page 5869, 2005.

[236] R. Wehner. Matched filters neural models of the external world. *Journal of Comparative Physiology A*, 161:511–531, 1987.

[237] R. Wehner. The polarization-vision project: championing organismic biology. In Elsner N. (eds) Schildberger, K., editor, *Neural Basis of Behavioural Adaptations*, volume 39, pages 103–143. Gustav Fischer Verlag, Stuttgart, Jena, New York, Fortschritts der Zoologie, 1994.

[238] R. Wehner. Polarization vision a uniform sensory capacity? *Journal of Experimental Biology*, 204:2589–2596, 2001.

[239] A. Weidemann, G. R. Fournier, L. Forand, and P. Mathieu. In harbor underwater threat detection/ identification using active imaging. In *Proceedings of SPIE, Photonics for Port and Harbor Security*, volume 5780, pages 59–70, 2005.

[240] L.B. Wolff. Using polarization to separate reflection components. In *Proceedings of IEEE Conference on Computer Vision and Pattern Recognition*, pages 363–369, 1989.

[241] L.B. Wolff. Polarization-based material classification from specular reflection. *IEEE Transaction on Pattern Analysis and Machine Intelligence*, 12(11):1059 – 1071, 1990.

[242] L.B. Wolff. Polarization camera technology. *Proc DARPA Image Understanding Works, Washington DC, USA*, pages 1031–1036, 1993.

[243] L.B. Wolff. Applications of polarization camera technology. *IEEE Expert*, 10(5):30 –38, October 1995.

[244] L.B. Wolff. Polarization vision: a new sensory approach to image understanding. *Image and Vision Computing*, 15:81–93, 1997.

[245] L.B. Wolff and A. G. Andreou. Polarization camera sensors. *Image and Vision Computing*, 13:497–510, 1995.

[246] L.B. Wolff, T.A. Mancini, P. Pouliquen, and A.G. Andreou. Liquid crystal polarization camera. *Robotics and Automation, IEEE Transactions on*, 13(2):195 –203, April 1997.

[247] L. Wu, J. Gao, Z. Fan, and Z. Xie. How to get navigation information within patches of sky as insects do? a primitive orientation by skylight polarization maps. In *2nd International Conference on Signal Processing Systems (ICSPS)*, 2010.

[248] B. Xie, Z. Xiang, H. Pan, and J. Liu. Polarization-based water hazards detection for autonomous off-road navigation. In *IEEE/RSJ International Conference on Intelligent Robots and Systems*, 2007.

[249] M. Yamada, K. Ueda, I. Horiba, and N. Sugie. Discrimination of the road condition toward understanding of vehicle driving environments. *IEEE Transaction on Intelligent Transportation Systems*, 2(1):26 – 31, 2001.

[250] K. M. Yemelyanov, M. A. Lo, E.N.Jr. Pugh, and N. Engheta. Display of polarization information by coherently moving dots. *Optics Express*, 11:1577–1584, 2003.

[251] K.M. Yemelyanov, S.S. Lin, W.Q. Luis, E.N.Jr. Pugh, and N. Engheta. Bio-inspired display of polarization information using selected visual cues. In *Proceedings of SPIE - The International Society for Optical Engineering 5158*, 2003.

[252] Z.Y. Zhang, H.F. Cheng, Z.H. Chen, and W.W. Zheng. Analysis of polarimetric characteristics of camouflage targets. In *Proceedings of SPIE 4th International Symposium on Advanced Optical Manufacturing and Testing Technologies: Optical Test and Measurement Technology and Equipment*, volume 7283, 2009.

[253] Z.Y. Zhang, H.F. Cheng, Z.H. Chen, and W.W. Zheng. Analysis of polarimetric scattering for backgrounds and camouflage materials. In *Proceedings of SPIE International Symposium on Photoelectronic Detection and Imaging: Advances in Infrared Imaging and Applications*, volume 7383, 2009.

[254] K. Zhao, J. Chu, T. Wang, and Q. Zhang. A novel angl ealgorithm of polarization sensor for navigation. *IEEE TRANSACTIONS ON INSTRUMENTATION AND MEASUREMENT*, 58:2791–2796, 2009.

[255] Y. Zhao, Q. Pan, and H. Zhang. Object detection by fusion spectral and polarimetric imagery. In *Proceedings of SPIE Vol. 6031*, 2006.

[256] Y. Zhao, L. Zhang, D. Zhang, and Q. Pan. Object separation by polarimetric and spectral imagery fusion. *Computer Vision and Image Understanding*, 113:855–866, August 2009.

[257] Y.Q. Zhao, P. Gong, and Q. Pan. Object detection by spectropolarimeteric imagery fusion. *IEEE Transactions on Geoscience and Remote Sensing*, 46:3337–3345, 2008.

Appendix A

Visual Behavior Based Bio-Inspired Polarization Techniques

Bio-inspiration is an established concept which is developing to meet the needs of many challenges particularly in machine vision applications. Polarization vision is one of the most important biological features in the animal kingdom. A broad range of applications has been inspired from it. Light's vector orientation (polarization) can be surprisingly weakly detected by some humans with their naked eyes ([83]), but humans need the help of polarizing optics to visualize most invisible polarization effects ([80]).

Many fish, cephalopods, crustaceans, insects, and other animals are capable of perceiving polarized light ([104]). Most animal photoreceptors are able to differentially react to partially linearly polarized light ([76], [154], [232], [238]). Fish ([88]) and birds ([158]) photoreceptors respond to polarized light patterns and hence are able to analyze linear polarization ([42]).

Firstly, we will briefly cover the polarization based visual behavior in the animal kingdom A.1, especially behaviors that can be mapped directly to the machine vision world such as orientation and navigation A.1.1, water and transparent object detection A.1.2, camouflage breaking A.1.3, and communication A.1.4. Secondly, a comprehensive cover of polarization-inspired machine vision applications will be given (A.2, A.3, A.4, A.5, A.6, A.8).

The main part of the chapter will go into details regarding bio-inspired polarization techniques in robotics applications A.2. We start with a short coverage of how to visualize polarization information A.3. Then a detailed complete survey of robot orientation and navigation techniques based on polarization will be given A.4 due to its importance for both communities of computer vision and robotics and its active ongoing research. A comprehensive survey of underwater polarization vision is also given A.5 due to the challenging problem of enhancing vision underwater and how it is greatly improved using polarization. Moderate survey of communication A.6 (few methods are clearly bio-inspired) and camouflage breaking A.7 techniques based on polarization are then covered. Finally, examples of general computer vision techniques based on polarization are mentioned A.8.

Figure A.1: Polarization in the animal kingdom. From left to right and top to bottom: Bee, desert ant (Cataglyphis), nocturnal bird (owl), and salmon fish

Our objective is to give a top view of polarization applications in computer vision and robotics, especially the bio-inspired polarization dependent techniques in order to have a comprehensive coverage of such important and active area of research.

A.1 Polarization based visual behavior in the animal kingdom

A.1.1 Orientation and Navigation

See section (5.1).

A.1.2 Water and Transparent Object Detection

Water surfaces can be discriminated from virtual surfaces (like mirages) by flying insects using their polarization vision ability ([102, 42]). Reflected polarized light is used by aquatic insects such as dragon-flies, mayflies, and backswimmers to detect calm water surfaces ([104]). Lythgoe & Hemmings ([124]), were the first to propose enhancing the transparent targets visibility in water using polarization. It was found that there are some objects which strongly reflect polarized light underwater ([41, 42]). It is proved that squids and their relatives see obscure objects using polarized light ([198, 203]).

A.1.3 Camouflage Breaking

Camouflage is a tool to defeat visual detection by predators. Lythgoe & Hemmings ([124]) proposed that polarization could be used to detect well-camouflaged targets in water. Polarization vision helps to detect transparent preys ([202]). Cephalopods (squid, cuttlefish, and octopus) can produce a variety of body patterns for camouflage using their optically malleable skin that contains neutrally controlled pigmented chromatophores as well as structural light reflectors and some of them are able to see camouflaged objects ([85, 201, 199, 200]). Mäthger & Hanlon ([150]), give evidence that the polarized aspect of iridescent color in squid skin produces highly dynamically changeable camouflaged patterns.

A.1.4 Communication

Polarization patterns are used for signaling by some animals. Some of these signals are controlled by the reflection of linearly polarized light. Forests butterflies use their wings as identifying markers by utilizing their polarization-dependent reflectivity ([212, 56]). Males seem to recognize females based on that ([212, 42, 56]).

Although the spectral irradiance varies strongly underwater with depth, signal constancy is stable and predictable thanks to polarization ([109]). Linked to specific communications, polarized light is strongly reflected from many stomatopod species body parts that are specialized for that kind of reflection ([42]). Polarized-light signals and color signals are used in much the same way by mantis shrimps ([42]). Cephalopods can produce body patterns for signaling using their skin that contains controlled pigmented chromatophores and structural light reflectors ([85]).

A.2 Polarization-Inspired machine vision applications

It is clear that the polarized patterns seen by some animals have an important impact on image formation as they are significant image features within the animals' visual fields. These significant polarized features can be transferred to the computer world leading toward numerous biologically inspired applications in camera technology, image formation, computer vision and robotics. A lot of researchers have already made use of polarization features in nature and inspired artificial vision techniques e.g ([115, 77, 218, 68]). Some of the current applications which imitate the animal natural behavior are found in robot orientation and navigation, camouflage breaking, communication, and underwater vision. Scene segmentation and object detection, recognition, and tracking are also active research areas e.g ([18, 5, 219, 210, 192]).

There are many applications that utilize polarization but are not biologically inspired (e.g. camera calibration, fiber optics communication, etc). Therefore these methods are out of the scope of this chapter, however, section (A.8) is dedicated to list different examples of polarization based applications in computer vision. This chapter mainly covers methods that imitate animal's behavior.

A.3 Visualizing Polarization Information

Polarization-Difference Imaging (PDI) inspired by polarization vision of certain animal species was introduced by ([169]). They demonstrated that PDI techniques may facilitate targets detection in scattering media even if targets show very weak polarization or are distant far from the optical setup ([236, 123, 169]).

In order to represent polarization without affecting other visual information such as color and brightness, special sensory substitution forms are required. Yemelyanov et al. ([251, 250]) investigated several bio-inspired representational methodologies for mapping polarization information into visual cues readily perceived by the human visual system. The visual cues and strategies they explored were a) the use of coherently moving dots superimposed on image to represent various range of polarization signals, b) overlaying textures with spatial and/or temporal signatures to isolate image regions with differing polarization, c) modulating luminance and/or scenes color contrast in terms of certain aspects of polarization values, and d) fusing polarization images into intensity-only images. They tried to determine which mappings are most suitable for specific applications such as object detection, navigation, sensing, scene classifications, and surface deformation. Lin et al. ([123]), proposed to use these visual cues to enhance visual surveillance techniques using polarization.

A.4 Robot Orientation and Navigation

See section (5.1).

A.5 Underwater Polarization Vision

Underwater imaging is widely used in scientific research and technology. Computer vision methods are used for a variety of applications, such as swimming pool life guards, mine detection, inspection of underwater power and telecommunication cables, pipelines, nuclear reactors, research in marine biology, archaeology and mapping.

The underwater polarized light distribution is mainly affected by a) the position of the sun or the moon in the sky, b) the water optical properties, c) the viewing depth, and d) surfaces reflections ([233, 156, 41, 204]). There are two distinct polarization patterns underwater, one inside Snell's window (underwater natural lighting comes from a limited cone above the scene which is caused by the illuminating rays refraction through the water surface, and is called the optical manhole or Snell's window) and one outside it. Generally, the polarization pattern inside Snell's window in a few meters depths is assumed to be determined by the same factors as those influencing the sky polarization ([233]). Small differences between the polarization patterns within Snell's window and outside it were found by ([41]). With increasing depth, the polarization pattern simplifies rapidly, tending to become horizontal everywhere ([221, 204]).

Lerner et al. ([120]) found that, only in clear waters, the polarization is correlated with the sun's elevation and the maximum value of the e-vector orientation angle equals the angle of refraction in the horizontal viewing direction. They concluded that navigation by means of underwater polarization is possible

under restricted conditions like being in clear waters, mainly near the horizontal viewing direction, and in locations where the sea floor has limited effects on the light's polarization. In underwater vision, the scattering of light largely degrades contrast between the observer and any object observed ([124, 238]). As a result of the existing horizontal polarization, a vertical analyzer would reduce the scattered light amount perceived and, hence, increase contrast.

In order to improve airborne underwater target detection, a proper polarization filter should be selected. This reduces line of sight problems and false alarms. Detection processing of a polarization filter that gives mostly surface related detections can be used to filter the final detection list as proposed in ([46]). They found that reducing the effect of the surface reflections is possible using a linear horizontal and a linear vertical polarizer. One of them contains surface reflection and one does not. If the system is active, the choice is the image from the polarizer that aligns with the light source. Otherwise (if passive), the linear horizontal polarizer image contains the most surface effects. They chose an algorithm called FX target detection ([45]) along with the linear polarizers to improve the detection of underwater targets.

The SHallow water Real-time IMagIng Polarimeter (SHRIMP), developed at the Office of Naval Research in 2000, can measure underwater partial polarization imagery ([218]). This sensor is a passive, three-channel device that concurrently measures the three Stokes vector components needed to find out the partial linear polarization of the scene. The testing of this sensor was completed in 2002 and the data was analyzed in ([216, 217]). They presented performance results which showed high probability for detecting the target with a low probability of a false alarm. The tests were done in very shallow water and surf zone regions. Their results support that a) the passive polarization signature is a range dependent quantity that decreases with increased range which do not impact performance greatly, and it is reflective (it is a function of target shape, surface characteristics, and light source level), b) the polarization magnitude signature is higher for the more turbid water.

Shashar et al. ([204]) studied how polarization signals vary when seen from different distances in water. To check how polarization changes as a function of distance in water, a polarization target was created. The target was set at different locations and types of water (clear and turbid). The target was videotaped over a range of distances with a custom-built underwater imaging polarimeter where the polarizer was rotated automatically at ($0°$, $45°$, and $90°$). Images were analyzed based on ([245]). Based on these measurements, ([204]) expect that polarization sensitivity will be most useful in a few meters distance for visual tasks in water. It will be much less useful for detecting objects, signals, or structures from far away. Celestial polarization patterns for navigation and orientation are expected to be limited to shallow waters, while solar navigation is possible through a deeper range.

In order to improve underwater visibility, some methods applied image enhancement either by showing p ([169, 218]) or showing the polarization contrast by subtracting two orthogonal polarization images ([54, 87]). The previous solutions assumed that polarization is associated with the object radiation, rather than the causes which degrade this signal. This assumption is not valid with increasing distance ([149]). In natural illumination, underwater polarization is associated with the visibility disturbance ([114]). The approach in ([181, 182, 225]) uses the captured polarization components using an underwater polarimetric

camera ([111, 225]) to delete that disturbance and inverts the physical model to recover an image similar to the clear visibility appearance. In their methods, they use two images maintaining the same viewing position while varying the polarization filter orientation. Polarization analysis was integrated with stereovision ([173]) by extending the single-camera method in ([224]) to a pair of cameras displaced by a finite base line where each camera makes use of a different polarization setting. The stereo disparity and polarization analysis are used to construct enhanced de-scattered views.

A method proposed for backscatter rejection ([121]) where the difference between object and background depolarization characteristics is used to improve image contrast. If the object and the background differ considerably in their depolarization properties, the signal-to-noise ratio (SNR) of the image may increase. Polarization image fusion for I, p, and α in a false RGB image was proposed to enhance the underwater image contrast ([122]).

A.6 Communication

From a communication's perspective, polarization modulation of an optical signal is an old concept that was proposed in ([153]). A basic theoretical treatment of a polarization modulation system can be found in ([162, 19]). The use of light polarization for sending data is common in fiber optic systems ([29]), and has previously been proposed for free space communications ([227]), but is rarely implemented due to concerns about depolarization in free space communications ([163]). Intensity modulation schemes are usually implemented and the polarization of the signal is usually ignored. A comparison of intensity and polarization modulation can be found in ([81]) which proves that polarization modulation outperforms intensity modulation.

Due to the seawater high conductivity which limits the electromagnetic waves propagation, radio frequency communications in seawater are impractical. Current methods, such as acoustic communication, are limited in bandwidth, data rate, and have a high latency ([96]). The use of cables is impractical for autonomous vehicles. Optical wireless communications that utilize the blue/green transparency window of seawater offer high bandwidth short range communications ([86]).

One useful feature of optical communications is the ability to exploit the light beam polarization to differentiate the received signal from backscatter, other transmitters, or surface light. (Cox, Hughes, & Muth, 2009 [39]) demonstrate a simple and low-cost system to explore the light polarization for underwater communication. The system uses diode lasers and is portable. It consists of a transmitter (which uses two diode lasers mounted to the faces of a polarizing beam splitter (PBS) to combine the orthogonal polarizations) and a receiver (which is constructed using another PBS with two detectors mounted to the faces that detect the imposed modulated data on the orthogonal polarizations). Their work is based on ([40]).

A communication method using an invisible polarization code which is drawn on the eyes of the robot was proposed by ([68]). A special graphics display for showing expression of robot's eyes was developed. The mobile robots are able to send and receive data, using the invisible polarization code, in order to establish an environment for cooperative robots. The code is a variation

of QR (Quick Response) Code which is a kind of 2D symbology developed by Denso Wave in 1994. QR Code contains information in both the vertical and horizontal directions. This QR Code was used to establish the communication between the mobile robots. To embed the invisible polarization code within the displayed data, they used a polarized symbol image to overlap additional data on the display. Their display consists of a conventional LCD panel, an additional liquid crystal (LC) layer and some optics. The LC layers can rotate the direction of the polarization axis according to the applied voltage. The LC layer in the LCD panel is responsible for showing visual data. The additional LC layer changes the direction of polarization from LCD outputs to generate invisible symbol patterns which are horizontal or vertical linear polarized light waves. This difference of orientation creates a binary symbol image. The invisible code can be perceived using a polarizer.

A.7 Camouflage Breaking

Polarization has a strong role to play in camouflage breaking specially in remote sensing. Camouflage technology has exposed the conventional remote sensing drawback because the natural background makes the targets detection very complicated. Scattering light polarimetric characteristics of camouflaged targets are very different from that of natural backgrounds. Polarimetric imaging can remove the backgrounds influence and improve the inspection efficiency. Compared with reflectance images, polarization images have advantages in camouflage targets detection. Polarimetric imaging has proven to be the most effective approach as it strongly reveals camouflaged targets embedded in complex backgrounds ([58, 24, 239, 253]).

In different remote sensing applications, polarimetric techniques were studied to find the optimum polarization for rain cancellation [213]), to enhance the image visibility of ocean waves ([187]), and to find optimum polarizations in the bistatic scattering from layered random media ([118]). An optimum polarization set that is able to enhance the signal-to-clutter ratio of a foliage-camouflaged stationary target was sought by ([50]). They employed a genetic algorithm to find optimum polarization configurations which minimize the effect of forests on the backscattered radar cross section response of a camouflaged hard target.

A field study of polarimetric characteristics was done by many researchers. It indicated that polarimetric imaging in hot infrared can eliminate the influence of background and enhance the efficiency of detection. Military coatings on aluminous plate was tested by ([77]) and ([59, 60]) studied the aircrafts and camouflaged vehicles polarimetric characteristics. Polarimetric experiments were carried out on vehicles ([65]) and ([7]) did it on tents.

In order to set up a portable polarimetric camera, ([43]) placed two twisted nematic liquid crystals and a fixed polarizing filter in front of a CCD camera. They presented two configurations: an autonomous sensor that uses a small camcorder for recording images; and an on-line sensor that uses a digital camera connected to a personal computer. For the same purpose ([252]) used a multispectral CCD polarization camera, a trisection prism to divide the scattering light from targets into three parts, and a polarizer. The simplest polarimetric camera may consist of a rotating linear polarizer and a CCD camera.

A polarimetric camera was used to break color camouflage ([43]). An orange

caterpillar camouflaged on an orange leaf show a case where polarization can be used where the orientation of polarization difference is significantly larger than the differences that appear in the brightness of the natural full colored image. Moreover, the angle of polarization variation in the light reflected from the caterpillar is much larger than that reflected from the leaf.

The properties of camouflage targets polarization scattering according to the change of incidence angle and observational angle were studied by ([252]). They concluded that the spectra of camouflage targets can simulate that of backgrounds. Polarization remote sensing proved that the camouflage targets with the same spectra most likely have very different polarimetric characteristics with background. Camouflage targets can be identified clearly in degree of polarization imaging and angle of polarization imaging. The camouflage effect is lost when it comes from traditional remote sensing to polarization remote sensing.

The spectral scattering light polarization signature is affected by the incidence angle, azimuth and the characteristics of materials. In ([253]) the coating degree of polarization was studied, and the results indicated that the coating degree of polarization represented a reverse trend with the surface reflectance and azimuth angle. A model based on Fresnel reflection equation was set up to describe the coatings polarization scattering behavior which can be predicted by the model up to visible light and infrared wavelengths.

A.8 Miscellaneous

Polarization filtered images analysis proved to be useful for computer vision. Hence, in this section we will cover different applications in computer vision based on polarization, which are not necessarily bio-inspired, to give the flavor of polarization in this important research area. See table (A.1) for some examples.

A.9 Summary

This section will summarize the different areas of bio-inspired polarization based computer vision and robotics applications, highlighting the important points in each area.

Visualizing polarization information A.3: A short survey was given on available methods to visualize polarization information in order to map it into visual cues such as polarization-difference imaging, coherently moving dots superimposed on image, overlaying textures with spatial and/or temporal signatures, modulating luminance and/or scenes color contrast in terms of certain aspects of polarization measured values, and fusing polarization images into intensity-only images.

Robot orientation and navigation A.4: We surveyed the different bio-inspired polarization techniques for robot orientation and navigation. Photodiodes, CCD/CMOS, and special sensors were used. The methods using photodiodes are cheap however they are simulating insects' strategy taking advantage of the skylight polarization through single numerical values rather than patterns. The techniques based on CCD/CMOS sensors are more expensive but

Applications	**Papers**
Analyze speculiarities	Wolff, 1989 [240]; Nayar, Fang, & Boult, 1997 [151]; Saito, Sato, Ikeuchi, & Kashiwagi, (1999a; 1999b) [171, 172]
Separate transparent and semi-reflected scenes	Farid, & Adelson, 1999 [64]; Schechner, Shamir, & Kiryati, (1999; 2000) [179, 180]
Classify materials	Wolff, 1997 [244]; Sarkar et al. 2010b [177]
Catadioptric camera calibration and 3D reconstruction	Morel, Stolz, & Gorria, 2004a [144]; Morel, Meriaudeau, Stolz, & Gorria, 2005 [146]; Atkinson, & Hancock, 2005 [8]; Morel, Ferraton, Stolz, & Gorria, 2006 [138]; Morel, Stolz, Meriaudeau, & Gorria, 2006 [148]; Morel, & Fofi, 2007 [139]; Morel, Seulin, & Fofi, (2007a; 2007b; 2008) [141, 140, 142]; Shabayek, Morel, & Fofi, (2009; 2010) [195, 196]; Shabayek, 2010 [194]
Industrial inspection	Morel, Stolz, & Gorria, 2004b [143]; Morel, Stolz, Meriaudeau, & Gorria, 2005 [147]; Morel, Stolz, & Gorria, 2006 [145]; Meriaudeau, Ferraton, Stolz, Bigué, & Morel, 2008 [128]
Segmenting scenes	Ben-Ezra, 2000 [18]; Ahmad, & Takakura, 2007 [5]; Terrier et al., 2008 [219]; Subramaniam, & Hancock, 2010 [210]; Shabayek et al., 2012 [192]
Dehazing	Schechner, Narasimhan, & Nayar, (2001; 2003; 2008) [183, 184, 185]
Polarimetric cameras which enable acquisition of polarization information in real time to be applied in any of the polarized based machine vision applications	Shutov, 1993 [206]; Cronin et al., 1994 [43]; Wolff, Mancini, Pouliquen, & Andreou, 1997 [246]; Ben-Ezra, 2000 [18]; Zhang et al., 2009a [252]

Table A.1: Examples of the usage of polarization in several computer vision and robotics applications

they can analyze the sky polarization patterns giving polarization maps (degree of polarization p, angle of polarization α, polarization contrast) in order to obtain various orientation and navigation clues. Using a fisheye lens with a CCD sensor is a good solution to obtain an omni-directional polarization image up to 180°. CMOS based techniques are promising for miniature robots as size is important for practical situations however the viewing angle is limited. Stereo vision based techniques provide different points of view but require more equipment and they are not practical especially if the cameras do not share the same baseline. Polarimetric cameras are a good solution as they acquire the polarization information in one shot which is better than conventional sensors which need at least three acquisitions. The spectro-polarimetric imager is good in the sense that it is possible to obtain both polarimetric and spectral information to be fused to obtain various clues for orientation and navigation.

Underwater polarization vision A.5: The effect of water surface reflections can be reduced using a linear horizontal and a linear vertical polarizer. The passive polarization signature decreases with increased range, and it is a function of target shape, surface characteristics, and light source level. Polarization sensitivity will be most useful in a few meters distance for visual tasks in water. In short distances, it is valid to assume that polarization is associated with the object radiation, and hence it is possible to use degree of polarization, angle of polarization, and difference polarization imaging to enhance the image. However it is not valid with long distance, therefore, the visibility disturbance should be deleted and the physical model of the disturbance cause should be inverted to obtain a clear image.

Communication A.6: Polarization modulation outperforms intensity modulation. Optical communications are able to exploit the light beam polarization to differentiate the received signal from any other signal in air and underwater. It is possible to show invisible polarization code on a display (e.g robot's eyes) to be embedded within visual information. Polarization information can be used effectively for cooperative robots.

Camouflage breaking A.7: Polarization has a strong role to play in camouflage breaking specially in remote sensing. Polarimetric imaging has proven to be the most effective approach as it strongly reveals camouflaged targets embedded in complex backgrounds. The camouflage targets with the same spectra most likely have very different polarimetric characteristics with background. The camouflage effect can be lost when it comes from traditional sensing to polarization sensing.

Miscellaneous A.8: Polarization filtered images analysis proved to be useful for computer vision and robotics applications. It has been used in a broad range of applications like specularities analysis, separating transparent and semi-reflected scenes, material classification, camera calibration, 3D reconstruction, industrial inspection, scene segmentation, de-hazing, and developing new camera technologies (e.g polarimetric cameras).

Appendix B

Polarization patterns simulation examples

B.1 Omni-Pola-Catadioptric sensors

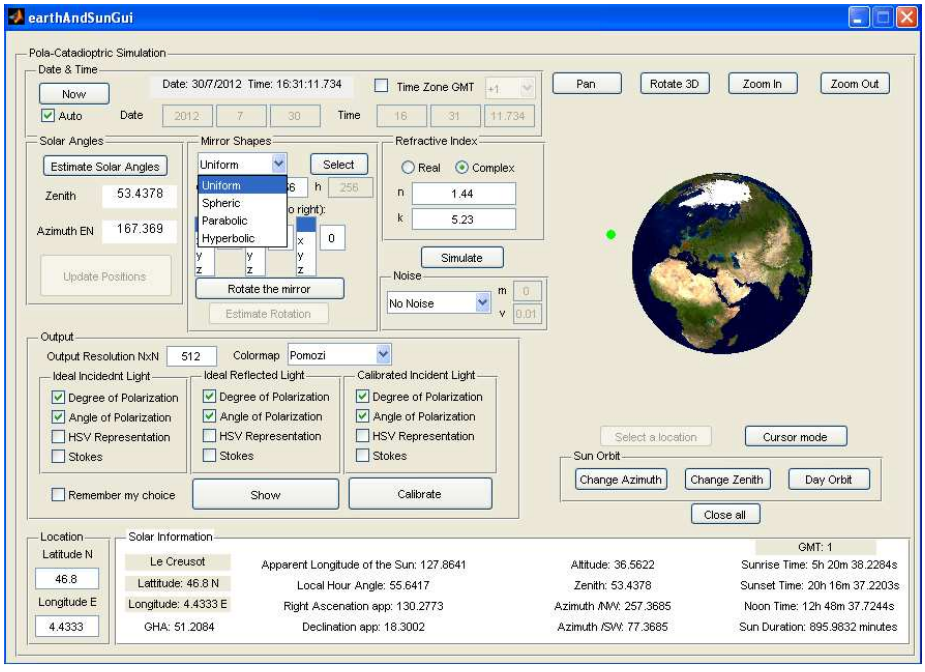

Figure B.1: Program snapshot to simulate polarization patterns on different types of mirrors

In the following sections each mirror is represented by f , its derivative is fd , $r = sqrt(x^2 + y^2)$ where x and y are the mirror points coordinates with the center at the tip of the mirror, the radius is R , and the height is h . The mirror

local polar coordinate system has $\theta - axis$ and $\psi - axis$ where $\theta = -atan(fd)$ is the zenith angle and $\psi = atan2(y, x)$ is the azimuth angle.

B.1.1 Uniform

1. $tmax = \pi/4$
2. $k = tmax/R$
3. $k1 = 1/k$
4. $f = k1 * log(abs(cos(k * r)))$
5. $fd = -tan(k * r)$

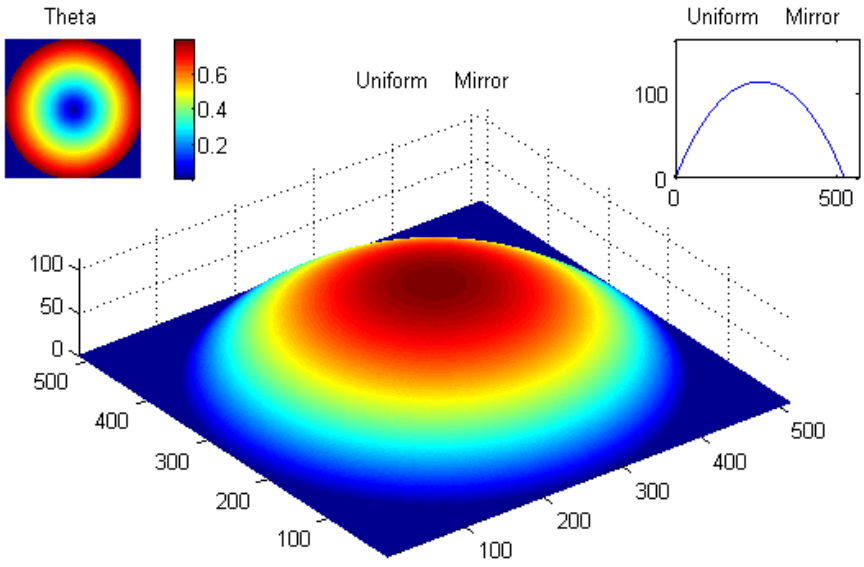

Figure B.2: Uniform mirror

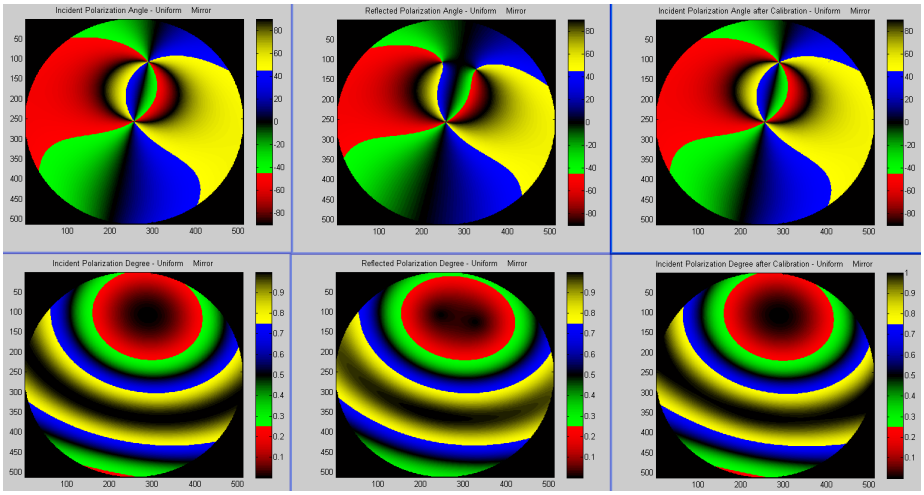

Figure B.3: Polarization patterns (incident/reflected/calibrated) as they appear on a uniform mirror

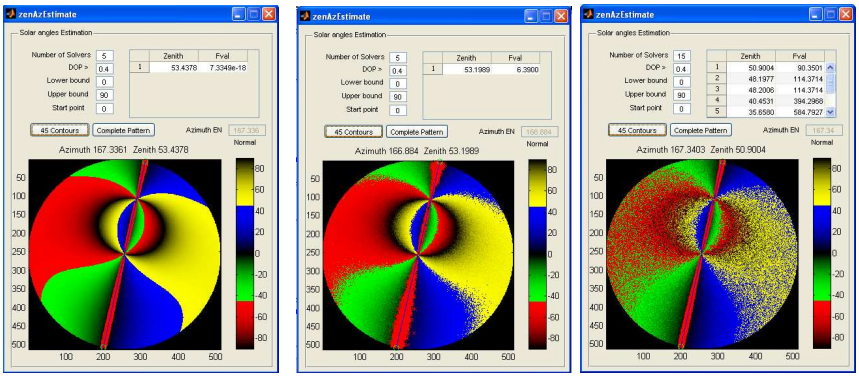

(a) Without noise

(b) Adding Gaussian noise with $mean = 0$ and $variance = 6$

(c) Adding Speckle noise with $mean = 0$ and $variance = 0.04$

Figure B.4: Solar angles estimation from calibrated polarization patterns after being reflected on a uniform mirror

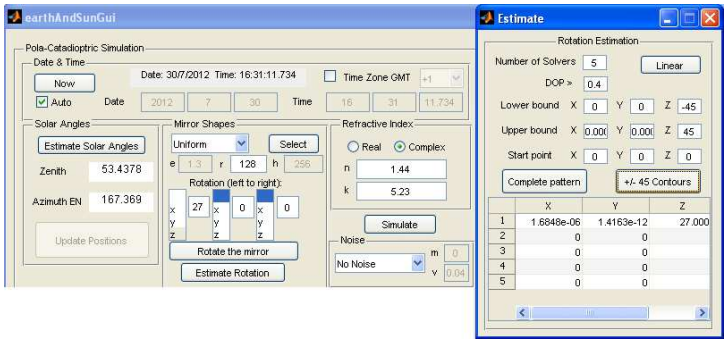

(a) Without noise

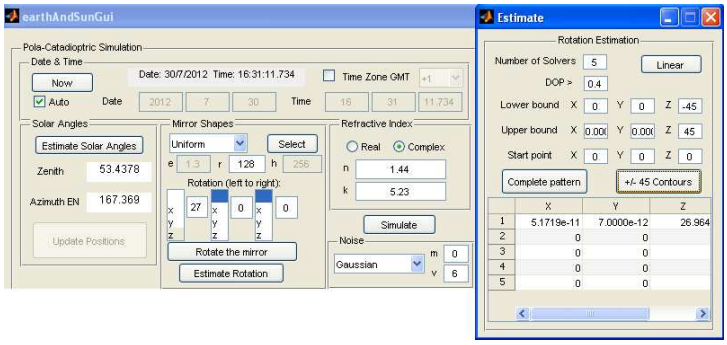

(b) Adding Gaussian noise with $mean = 0$ and $variance = 6$

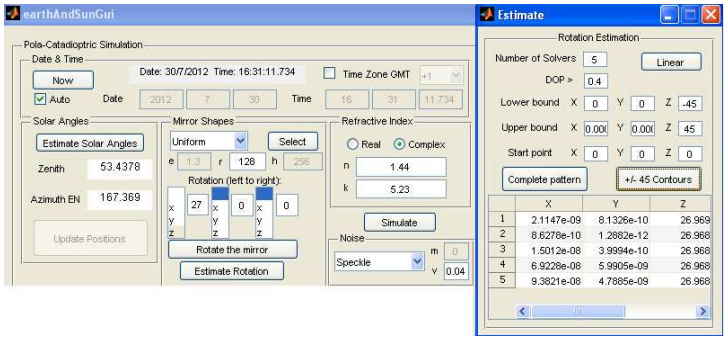

(c) Adding Speckle noise with $mean = 0$ and $variance = 0.04$

Figure B.5: One rotation angle estimation from calibrated polarization patterns after being reflected on a uniform mirror

B.1.2 Spherical

1. $f = sqrt(R^2 - r^2)$
2. $fd = -r/sqrt(R^2 - r^2)$

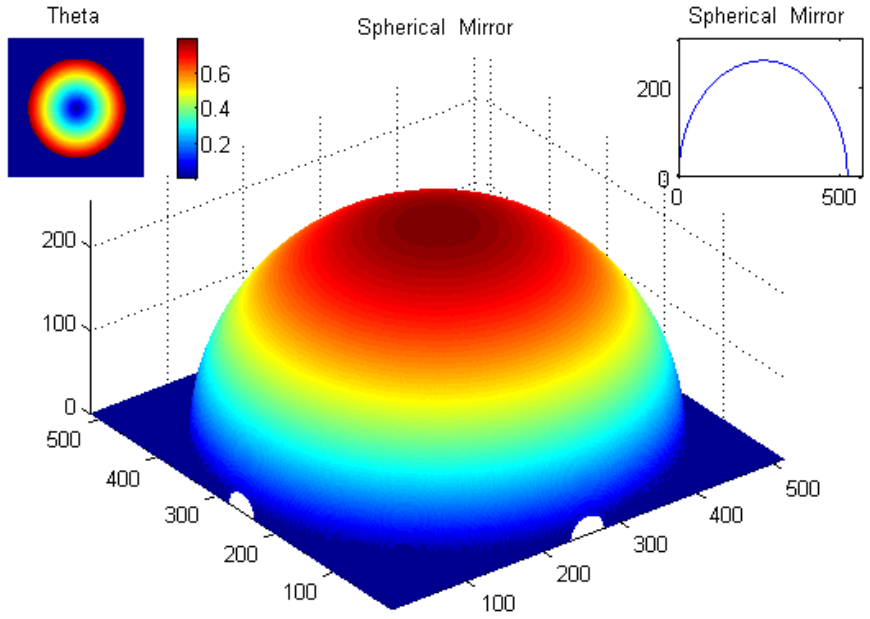

Figure B.6: Spherical mirror

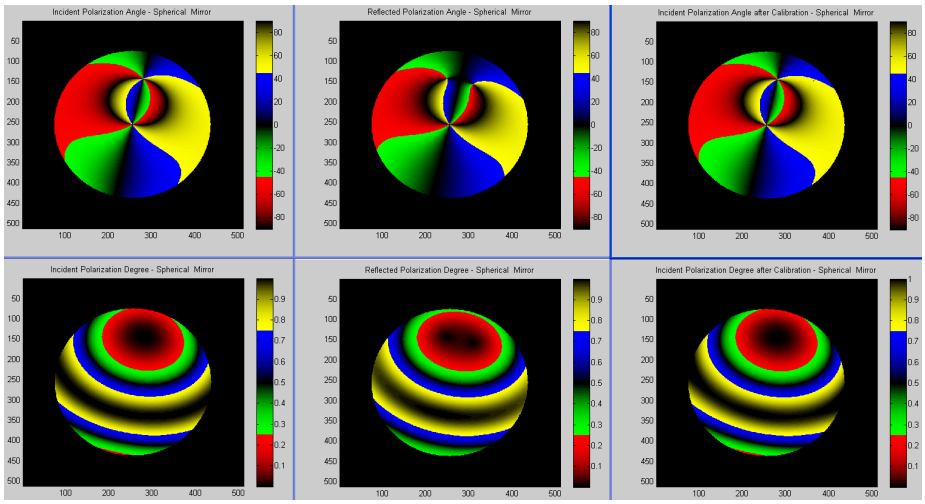

Figure B.7: Polarization patterns (incident/reflected/calibrated) as they appear on a spherical mirror

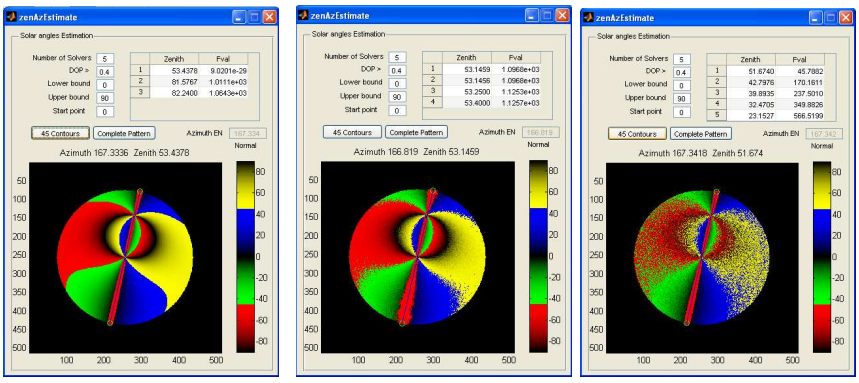

(a) Without noise

(b) Adding Gaussian noise with $mean = 0$ and $variance = 6$

(c) Adding Speckle noise with $mean = 0$ and $variance = 0.04$

Figure B.8: Solar angles estimation from calibrated polarization patterns after being reflected on a spherical mirror

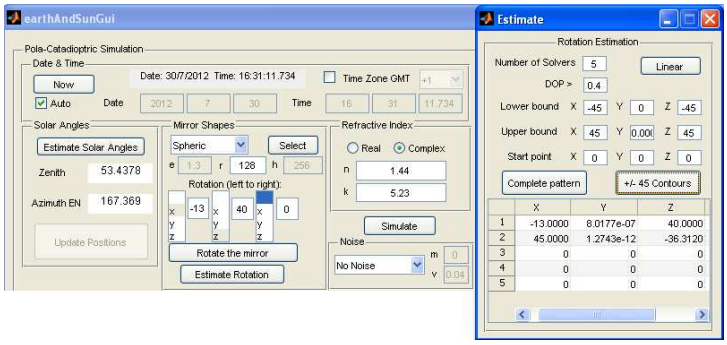

(a) Without noise

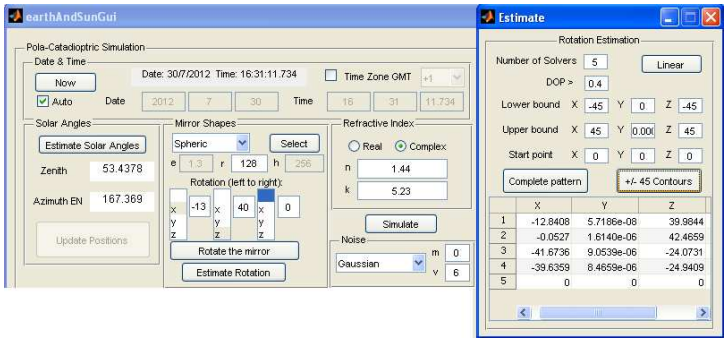

(b) Adding Gaussian noise with $mean = 0$ and $variance = 6$

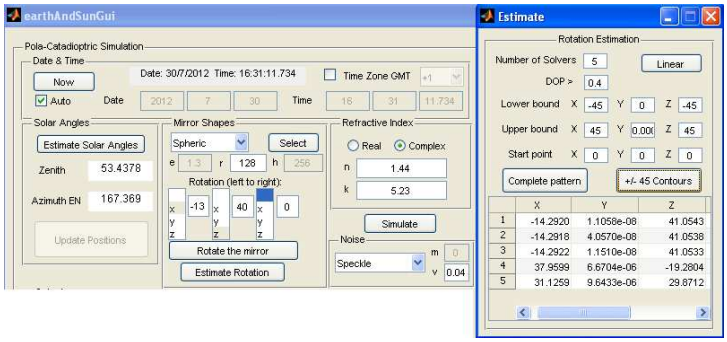

(c) Adding Speckle noise with $mean = 0$ and $variance = 0.04$

Figure B.9: Two rotation angles estimation from calibrated polarization patterns after being reflected on a spherical mirror

B.1.3 Parabolic

1. $f = h * (1 - (r/R)^2)$
2. $fd = -2 * h * r/R^2$

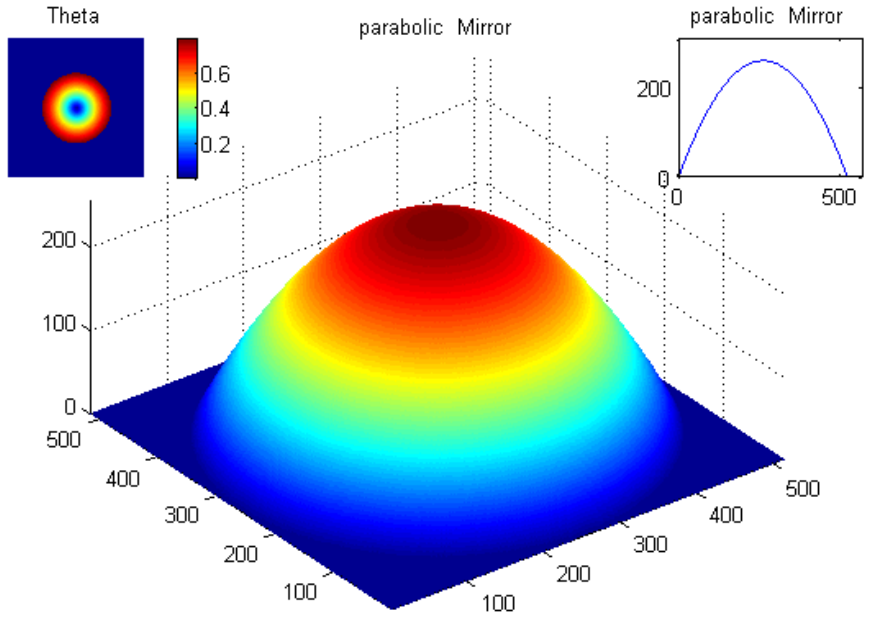

Figure B.10: Parabolic mirror where $radius = height$

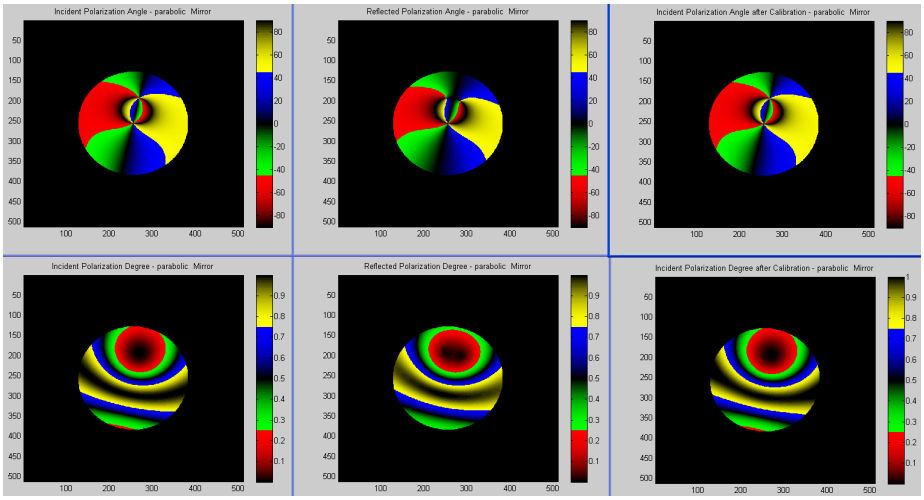

Figure B.11: Polarization patterns (incident/reflected/calibrated) as they appear on a parabolic mirror

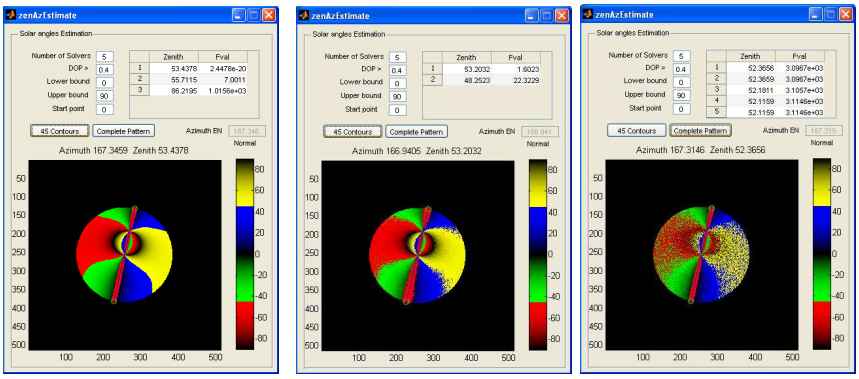

(a) Without noise

(b) Adding Gaussian noise with $mean = 0$ and $variance = 6$

(c) Adding Speckle noise with $mean = 0$ and $variance = 0.04$

Figure B.12: Solar angles estimation from calibrated polarization patterns after being reflected on a parabolic mirror

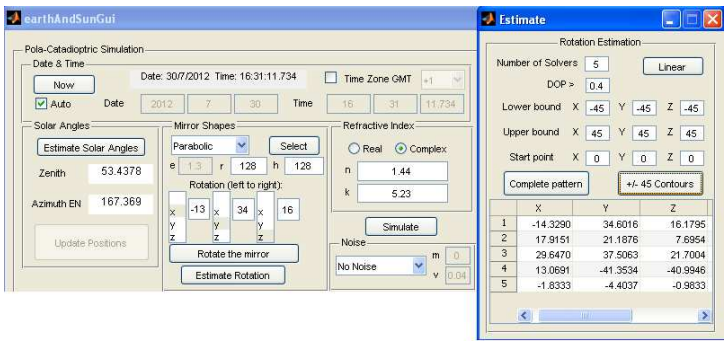

(a) Without noise

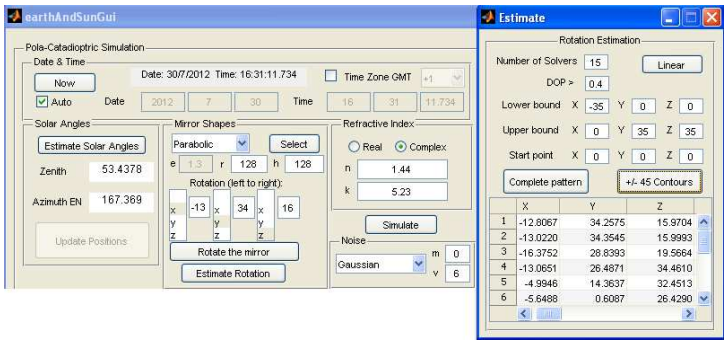

(b) Adding Gaussian noise with $mean = 0$ and $variance = 6$

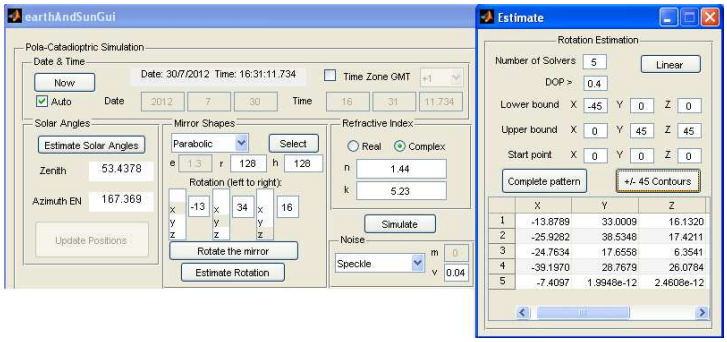

(c) Adding Speckle noise with $mean = 0$ and $variance = 0.04$

Figure B.13: Three rotation angles estimation from calibrated polarization patterns after being reflected on a parabolic mirror

B.1.4 Hyperbolic

1. $a = (1/(2 * h)) * ((R^2/(e^2 - 1)) - h^2)$
2. $b = a * sqrt(e^2 - 1)$
3. $c = a + h$
4. $f = c - a * sqrt(1 + (r^2/b^2))$
5. $fd = -a * r/(b^2 * sqrt(1 + (r^2/b^2)))$

where eccentricity $e > 1$, $R^2 > h^2(e^2 - 1)$

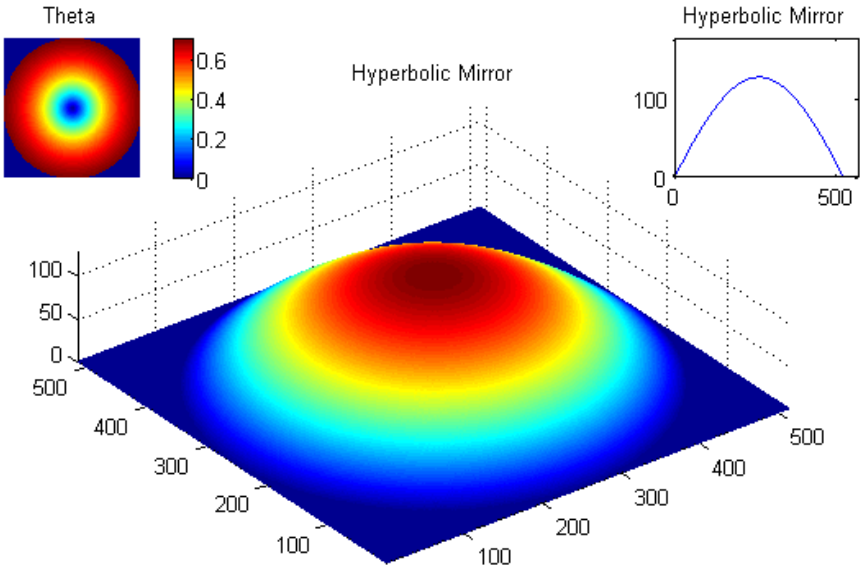

Figure B.14: Hyperbolic mirror where $radius = 2{*}height$ and $eccentricity = 1.3$

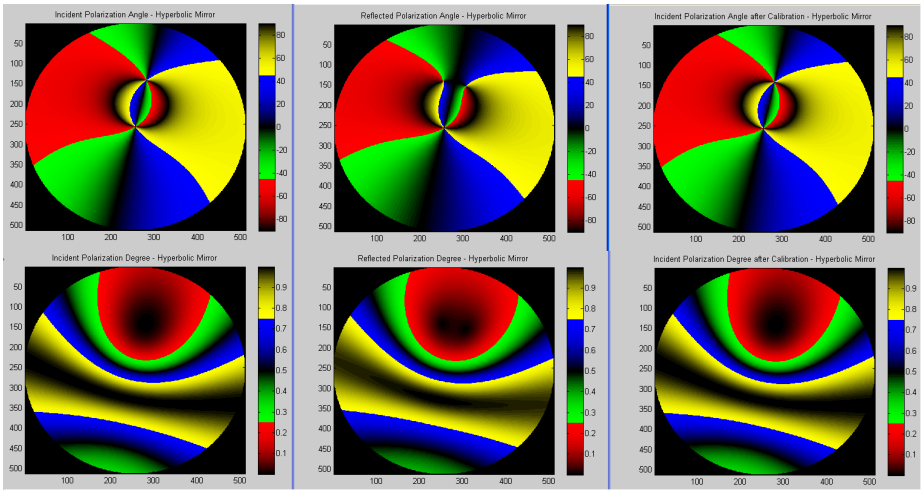

Figure B.15: Polarization patterns (incident/reflected/calibrated) as they appear on a hyperbolic mirror

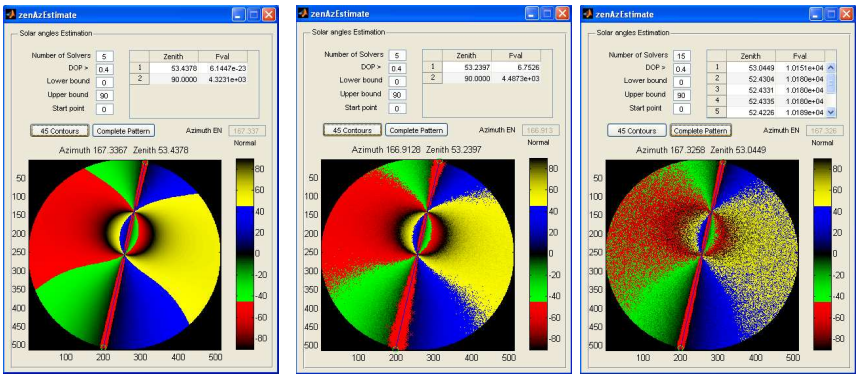

(a) Without noise

(b) Adding Gaussian noise with $mean = 0$ and $variance = 6$

(c) Adding Speckle noise with $mean = 0$ and $variance = 0.04$

Figure B.16: Solar angles estimation from calibrated polarization patterns after being reflected on a hyperbolic mirror

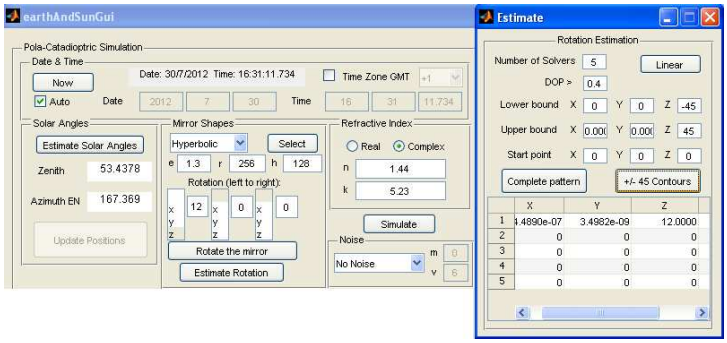

(a) One angle estimation without noise

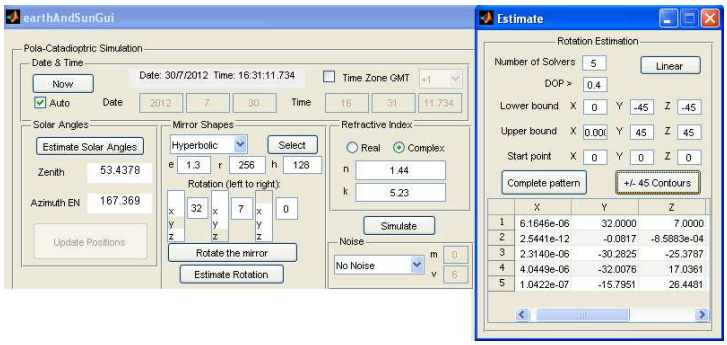

(b) Two angles estimation without noise

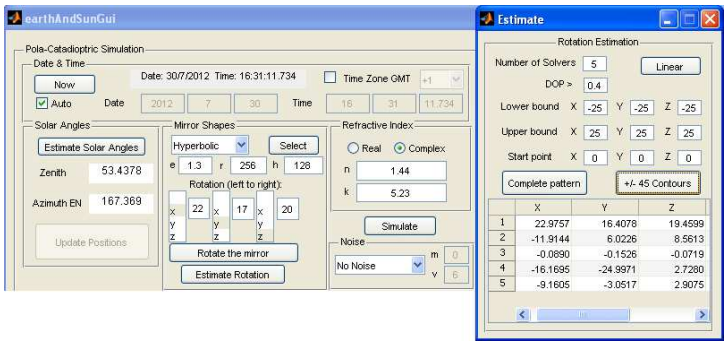

(c) Three angles estimation without noise

Figure B.17: Rotation angles estimation from calibrated polarization patterns after being reflected on a hyperbolic mirror

B.2 Noisy skylight polarization patterns

The noisy incident angle α and degree p of polarization patterns after adding high Speckle noise with variance 0.85 and mean 0 are shown in figure (B.18) and the noisy incident angle α and degree p of polarization patterns after adding high Gaussian noise with variance 15 and mean 3 are shown in figure (B.19),

where the simulation parameters in table (5.1a) are used.

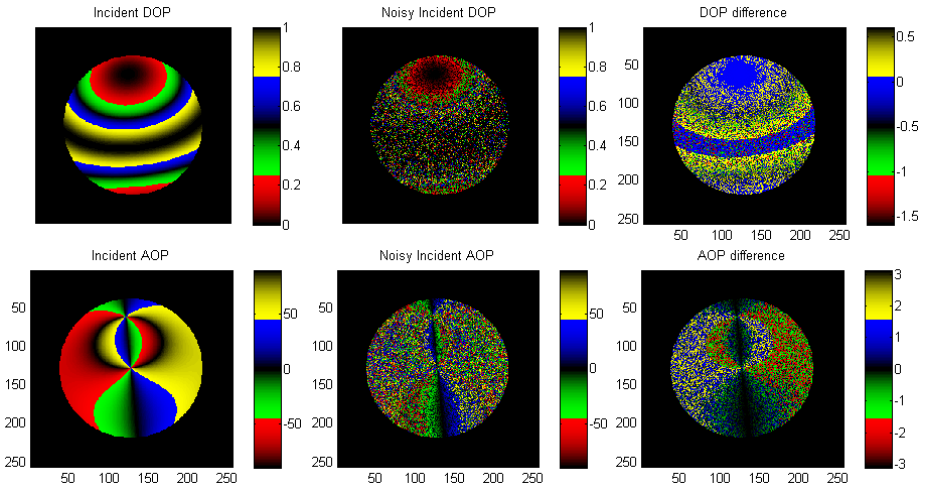

Figure B.18: Noisy incident angle α and degree p of polarization patterns. Speckle noise with variance 0.85 and mean 0.

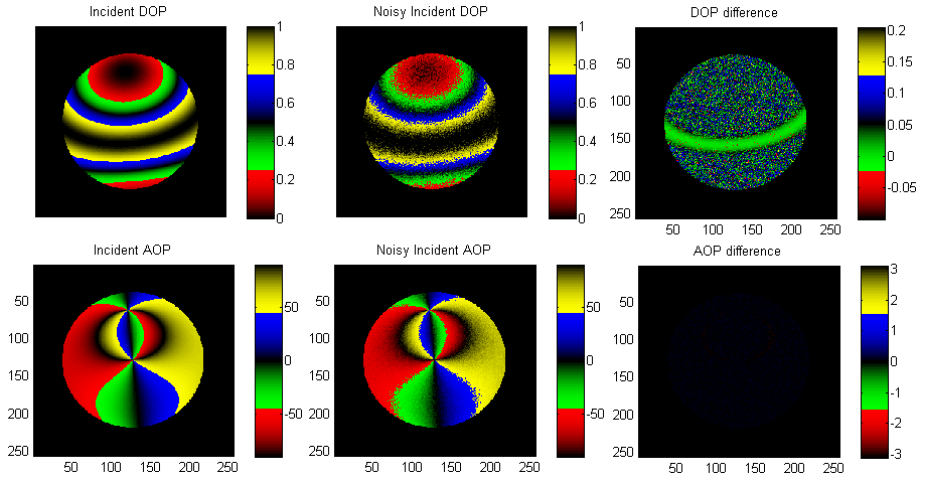

Figure B.19: Noisy incident angle α and degree p of polarization patterns. Gaussian noise with variance 15 and mean 3.

B.3 Solar angles estimation

Figure (B.20) shows some examples of solar angles estimation within the day, and table (5.1) gives the simulation parameters and the computation results.

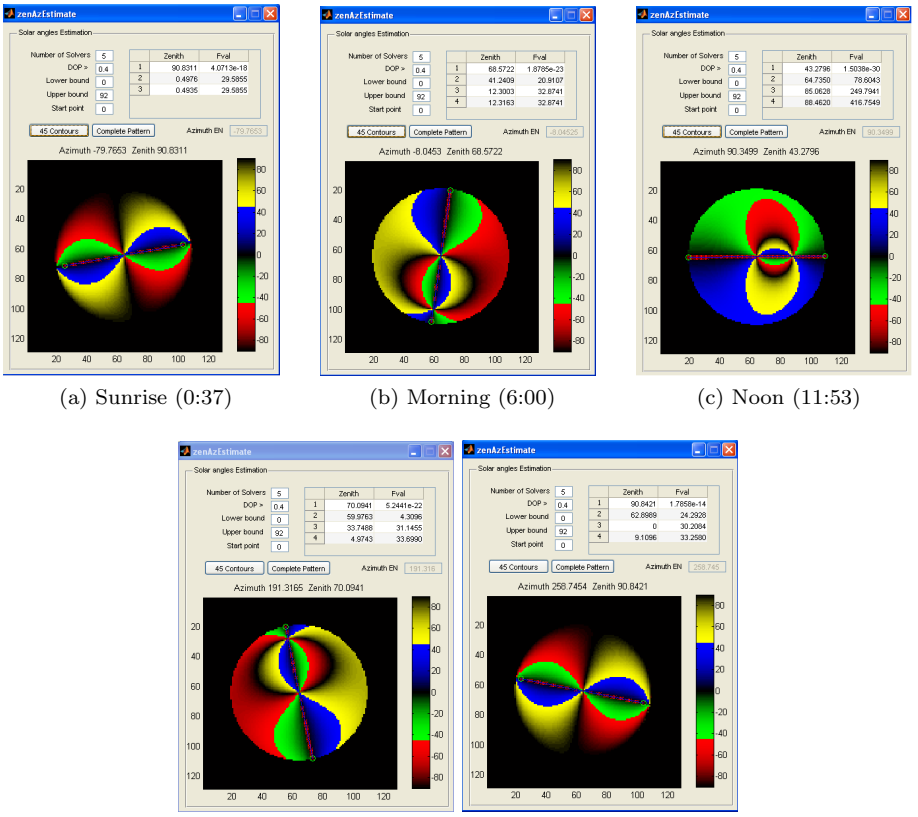

(a) Sunrise (0:37) (b) Morning (6:00) (c) Noon (11:53)

(d) Afternoon (18:00) (e) Sunset (23:04)

Figure B.20: Solar azimuthal and zenital angles estimation.

Examples of noisy α patterns and the estimated solar angles in different times of the day are shown in figures (B.21, B.22, B.23).

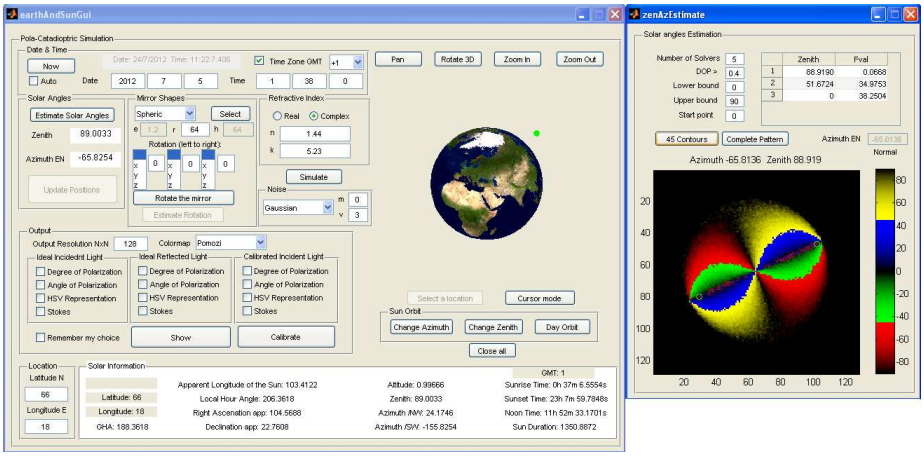

Figure B.21: Solar angles estimation from a noisy α pattern at 01:38. Simulation parameters are shown on the left handside and estimation results on the right handside.

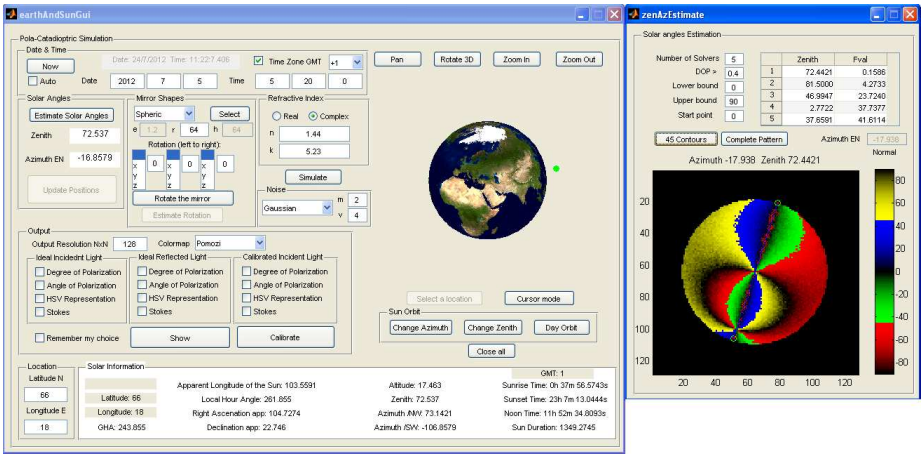

Figure B.22: Solar angles estimation from a noisy α pattern at 05:20. Simulation parameters are shown on the left handside and estimation results on the right handside.

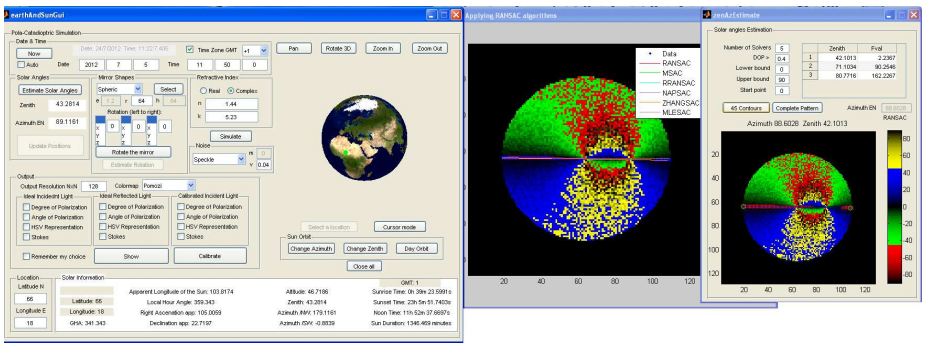

Figure B.23: Solar angles estimation from a noisy α pattern at 11:50. Simulation parameters are shown on the left handside and estimation results on the right handside.

B.4 AV attitude estimation

Examples of estimating two angles of rotation assuming the knowledge of the rotation axis based on algorithm (5.13) are shown in figures (B.24, B.25).

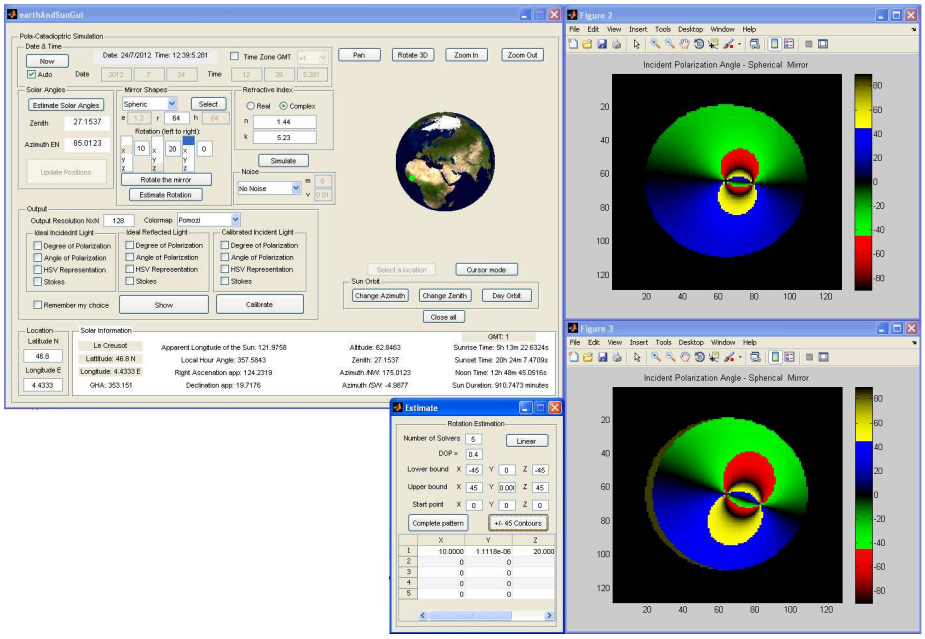

Figure B.24: Estimating two angles of rotation assuming the knowledge of the rotation axis. The robot is rotated around x by 10°then around z by 20°. The simulation parameters and the original α pattern (before rotation) are shown on the top. The estimation results and the rotated α pattern are shown on the bottom. Note that the rotation order is not assumed to be known. The earth is represented in dark green.

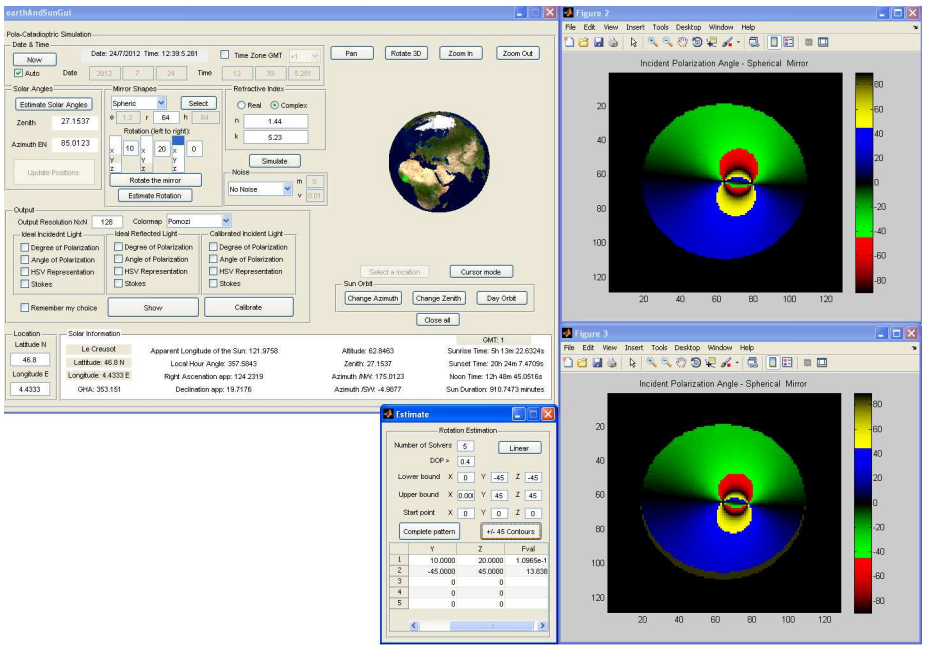

Figure B.25: Estimating two angles of rotation assuming the knowledge of the rotation axis. The robot is rotated around y by 10°then around z by 20°. The simulation parameters and the original α pattern (before rotation) are shown on the top. The estimation results and the rotated α pattern are shown on the bottom. Only the first solution is accepted as the second did not converge to a value close to zero. Note that the rotation order is not assumed to be known. The earth is represented in dark green.

Estimating three angles of rotation where no knowledge is assumed about the rotation order however better lower and upper bounds are assumed to be provided, figure (5.8a) shows an example which is based on algorithm (5.13).

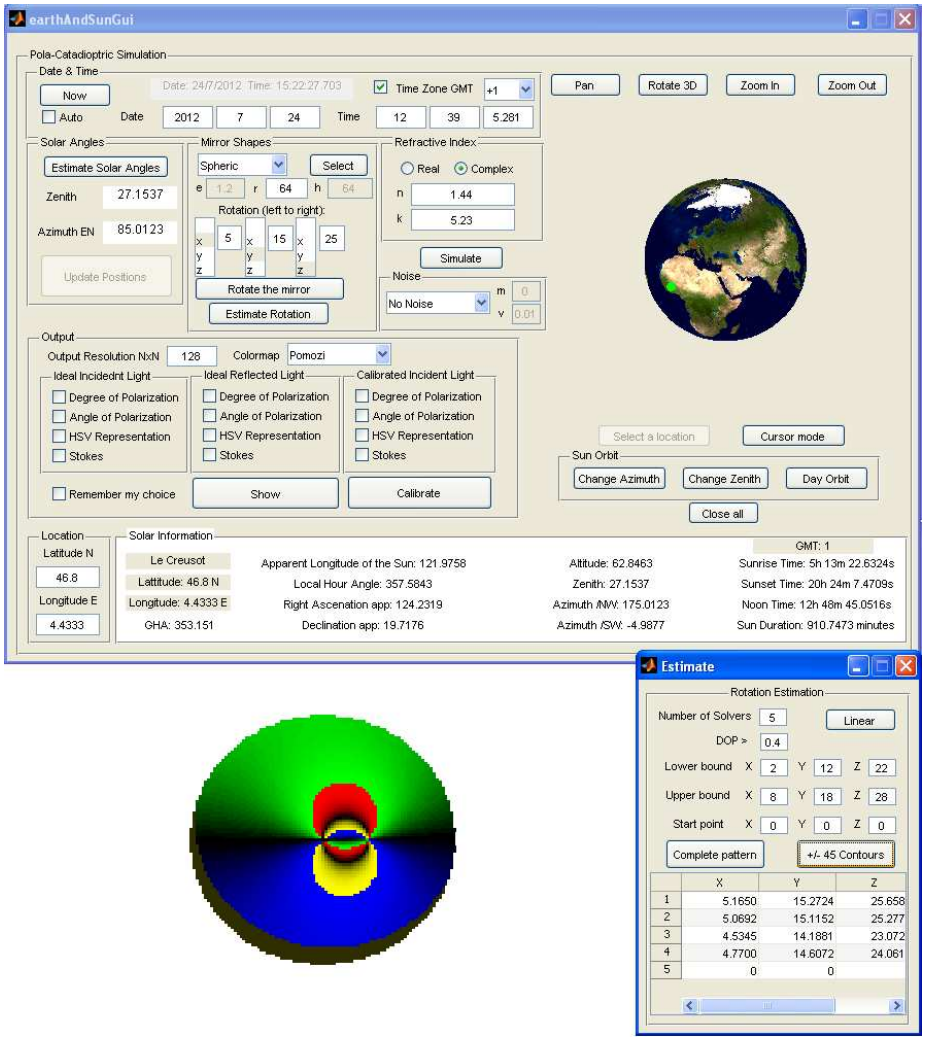

Figure B.26: Estimating three angles of rotation where no knowledge is assumed about the rotation order however better lower (2°,12°,22°) and upper (8°,18°,28°) bounds are assumed to be provided. The robot is rotated by (5°, 15°, 25°) around x, y, and z respectively . The earth is represented in dark green.

Figure (B.27) shows an example of estimating an equivalent rotation (3 angles) to a rotation about one unknown axis and figure (B.28) shows an example of estimating an equivalent rotation (3 angles) to two rotations about two unknown axises.

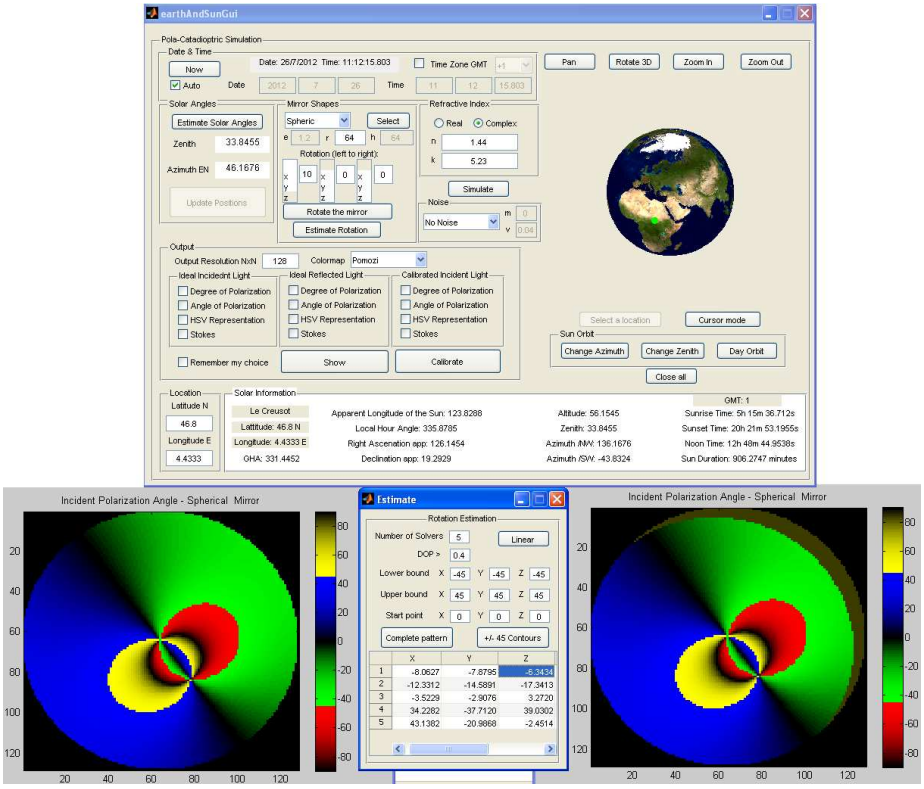

Figure B.27: Estimating one angle of rotation assuming no knowledge of the rotation axis. The robot is rotated around z-axis by 10°. The simulation parameters are shown on the top. The the rotated α pattern, estimation results, and the rotated pattern based on the first estimation are shown on the bottom from left to right respectively. The earth is represented in dark green.

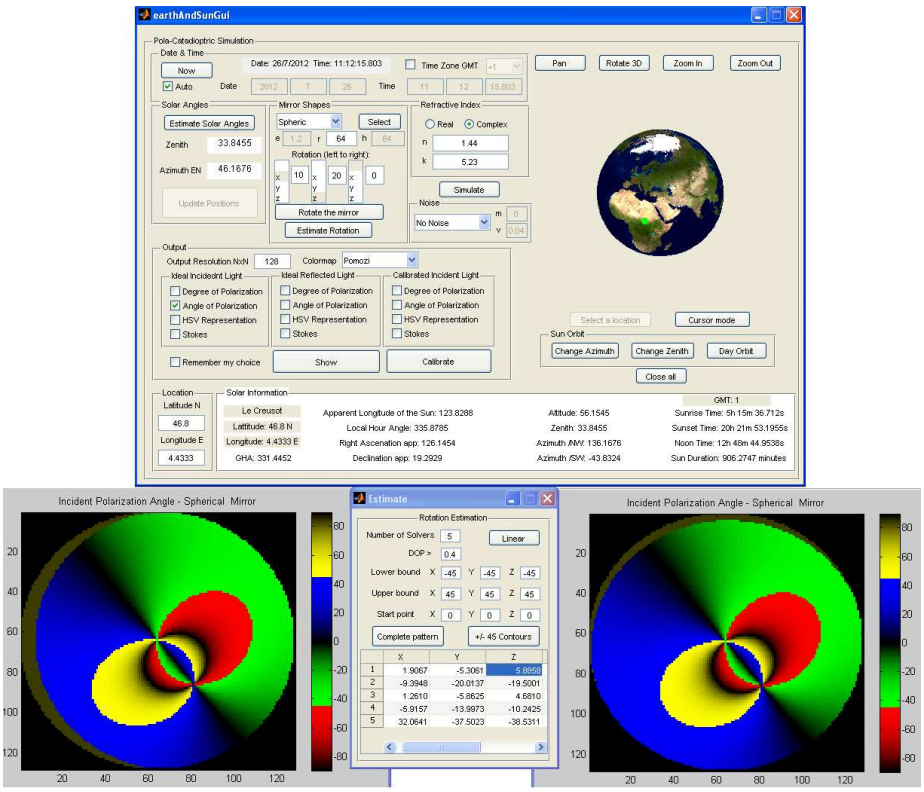

Figure B.28: Estimating two angles of rotation assuming no knowledge of the rotation axises. The robot is rotated around x by 10°then around z by 20°. The simulation parameters are shown on the top. The the rotated α pattern, estimation results, and the rotated pattern based on the first estimation are shown on the bottom from left to right respectively. The earth is represented in dark green.

Figures (B.29, B.30, B.31) show the results of adding noise on γ estimation (one angle of rotation) based on algorithm (5.11). Simulation parameters are shown in table (5.6).

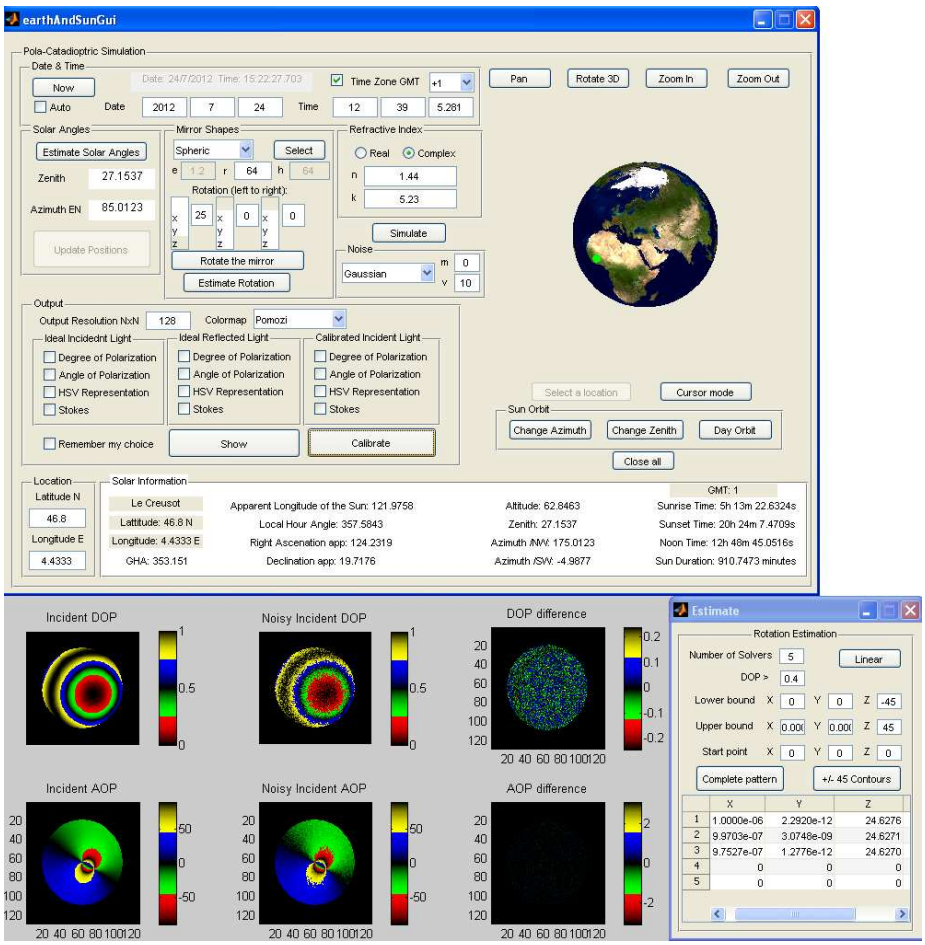

Figure B.29: γ estimation using algorithm (5.11) after adding Gaussian noise with zero mean and *variance* = 10. The upper part shows the program with the simulation parameters and the lower part shows the rotated noisy α pattern and the estimation results on the axis of rotation (z-axis).

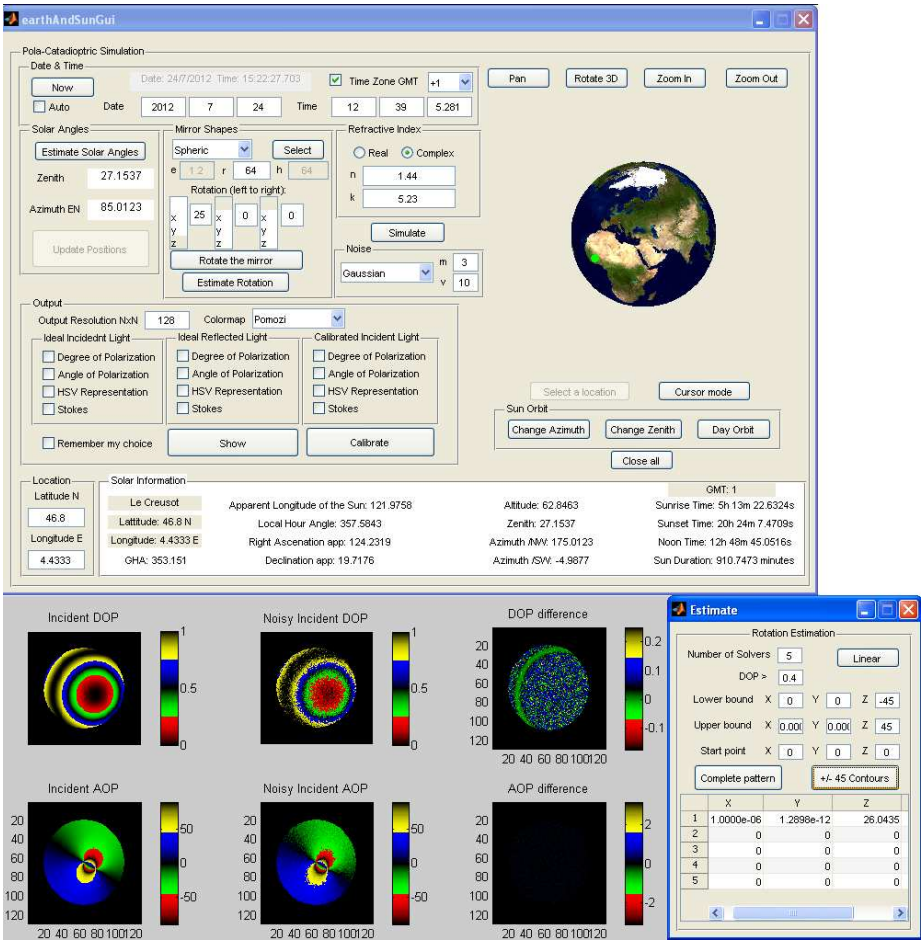

Figure B.30: γ estimation using algorithm (5.11) after adding Gaussian noise with $mean = 3$ and $variance = 10$. The upper part shows the program with the simulation parameters and the lower part shows the rotated noisy α pattern and the estimation results on the axis of rotation (z-axis).

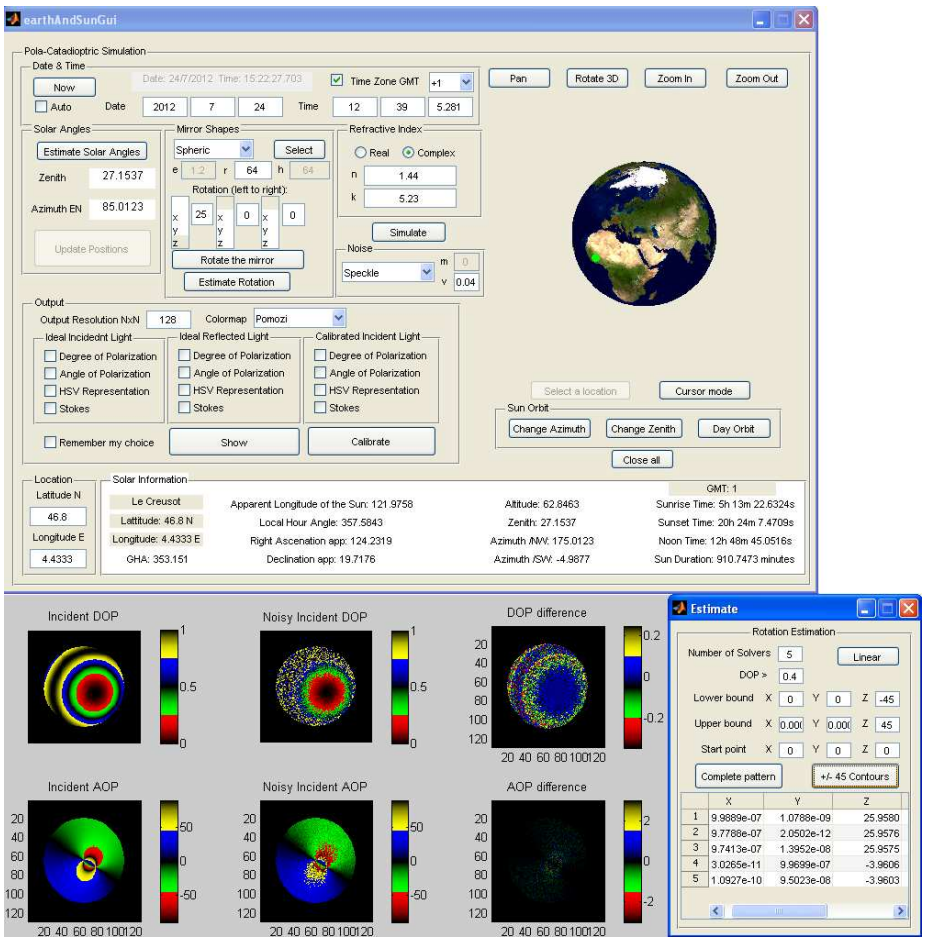

Figure B.31: γ estimation using algorithm (5.11) after adding speckle noise with zero mean and *variance* = 0.04. The upper part shows the program with the simulation parameters and the lower part shows the rotated noisy α pattern and the estimation results on the axis of rotation (z-axis).

Figures (B.32, B.33, B.34) show the results of adding noise on general rotation estimation based on algorithm (5.13).

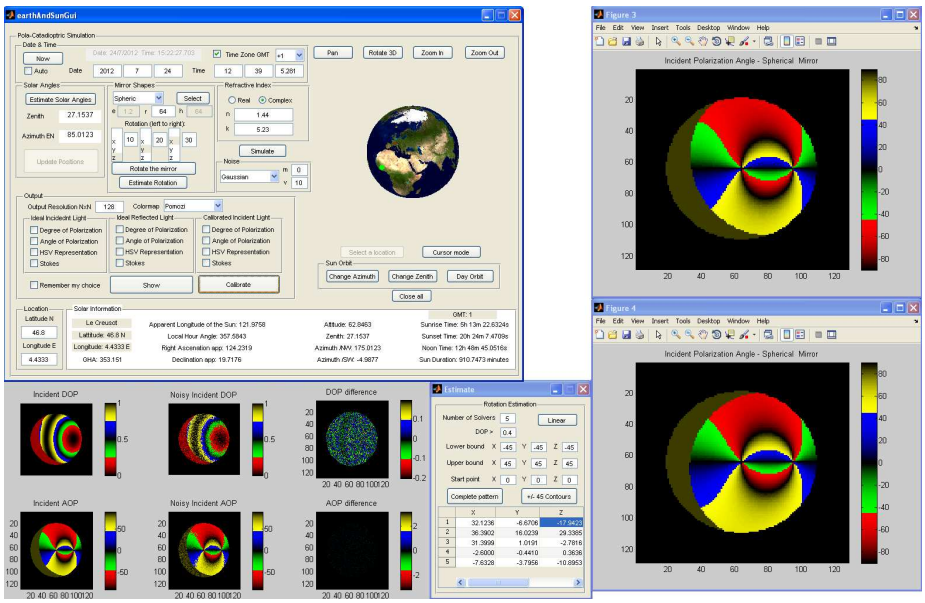

Figure B.32: General rotation estimation using algorithm (5.13) after adding Gaussian noise with zero mean and *variance* = 10. The upper part shows the program with the simulation parameters and applying the original rotation. The lower part shows the rotated noisy α pattern, the estimation results, and the first rotation estimation (roll ϕ, pitch β, and yaw γ) after being applied to the original incident α pattern.

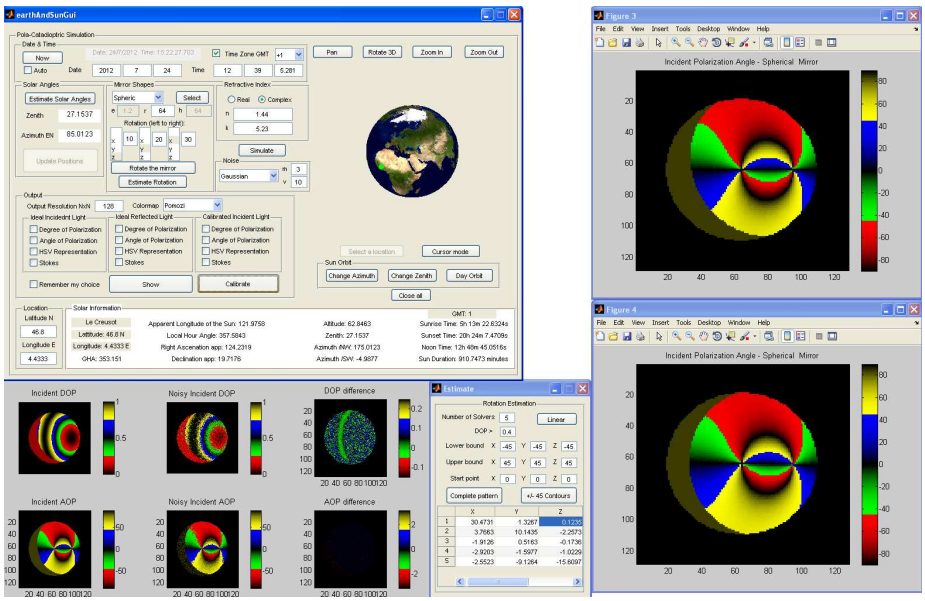

Figure B.33: General rotation estimation using algorithm (5.13) after adding Gaussian noise with $mean = 3$ and $variance = 10$. The upper part shows the program with the simulation parameters and applying the original rotation. The lower part shows the rotated noisy α pattern, the estimation results, and the first rotation estimation (roll ϕ, pitch β, and yaw γ) after being applied to the original incident α pattern.

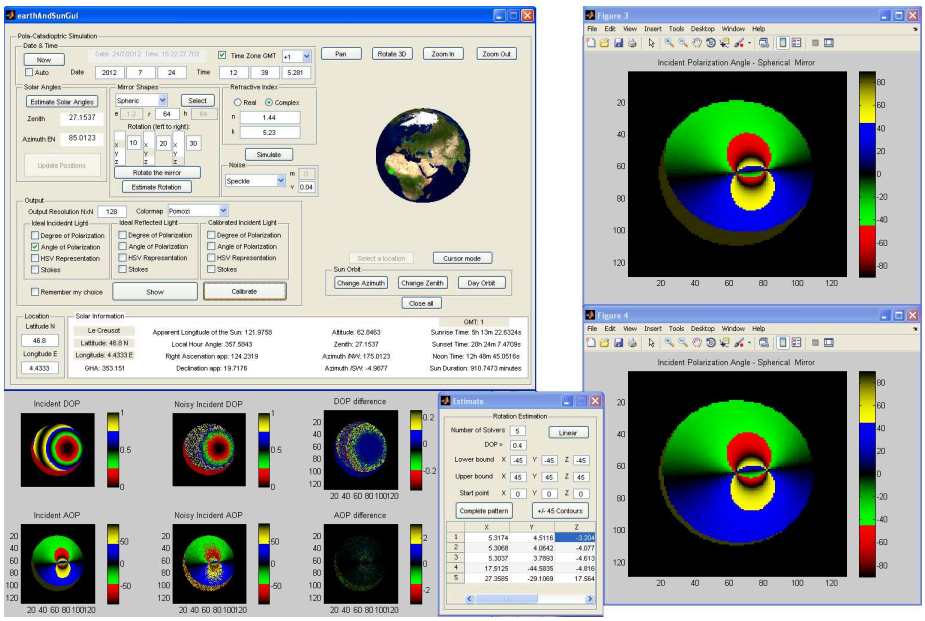

Figure B.34: General rotation estimation using algorithm (5.13) after adding speckle noise with zero mean and $variance = 0.04$. The upper part shows the program with the simulation parameters and applying the original rotation. The lower part shows the rotated noisy α pattern, the estimation results, and the first rotation estimation (roll ϕ, pitch β, and yaw γ) after being applied to the original incident α pattern.

SPIM

■ École doctorale SPIM - Université de Bourgogne/UFR ST BP 47870 F - 21078 Dijon cedex
■ tél. +33 (0)3 80 39 59 10 ■ ed-spim@univ-fcomte.fr ■ www.ed-spim.univ-fcomte.fr

UNIVERSITÉ DE BOURGOGNE